The Pennsylvania State University

The Graduate School

QUANTUM TRANSPORT IN TOPOLOGICAL MATERIALS AND PROXIMITY EFFECT IN FERROMAGNETIC NANOWIRES

A Dissertation in

Physics

by

Jue Jiang

Submitted in Partial Fulfillment
of the Requirements
for the Degree of

Doctor of Philosophy

August 2019

The dissertation of Jue Jiang was reviewed and approved* by the following:

Moses H. W. Chan

Professor Emeritus of Physics

Evan Pugh Professor

Dissertation Adviser, Chair of Committee

Cui-zu Chang

Assistant Professor of Physics

Chaoxing Liu

Associate Professor of Physics

Roman Engel-Herbert

Associate Professor of Materials Science and Engineering and Physics

Richard W. Robinett

Professor of Physics

Associate Head for Undergraduate and Graduate Students

*Signatures are on file in the Graduate School.

Abstract

The magnetic topological insulator (TI) and the superconductor look different from each other, however, they share a similar electrical transport property of a profound significance: zero resistance. Their potential in the future low-power-consumption applications is beyond measure, therefore, the research attention on TI has been dramatically expanding since its debut in 2009, and the study of superconductivity keeps inspiring people of generations in the past 100 years.

The realization of the non-dissipative channel in magnetic TI requires the broken time-reversal-symmetry by ferromagnetic dopants. The engineering of ferromagnetism, in turn, induces new topological phenomena. In this dissertation, we show that by fabricating a magnetic TI/pure TI/magnetic TI sandwich structure, rigorous quantum anomalous Hall (QAH) effect could be realized along with 'axion insulator' state or topological Hall effect, depending on the sample structure. In Cr-doped/non-doped/V-doped TI heterostructures, QAH effect emerges when the magnetizations of the Cr-doped and V-doped magnetic layers are parallel, while an 'axion insulator' state with zero Hall resistance and insulating longitudinal resistance appears when magnetization alignment is anti-parallel; In an Cr-doped/non-doped/Cr-doped TI structure, by tuning the chemical potential, QAH effect crossovers to topological Hall effect, where the electron spins form topologically non-trivial spin textures.

Superconductivity, on the other hand, would be destroyed in a ferromagnet due to the decoupling of a Cooper pair by the exchange coupling. Therefore, a spin-singlet Cooper pair is not able to survive in a ferromagnet more than a few nanometers. In this dissertation,

however, we show that in a ferromagnetic Ni nanowire (500 nm wide and 40 nm thick), by simply adding a thin Cu buffer layer with natural oxidation between superconducting/ferromagnetic interface, an unusual long-range superconducting proximity effect (up to 136 nm) emerges. Strong evidence points to the Cu oxides for providing a noncollinear magnetic profile that is crucial to the induction of spin-triplet. The spin-triplet pairing can have two electrons with the same spin direction, and thus immune to the exchange coupling of the ferromagnetic nanowire.

The experiments of magnetic TI heterostructures and spin-triplet superconductivity presented in this dissertation would inspire more relating studies and pave the way for next-generation energy-efficient spintronic and electronic applications.

Contents

List of Figures viii

List of Tables xviii

Acknowledgment xix

Part I: Quantum transport in magnetic topological insulator heterostructure 1

Chapter 1 Introduction of Topological Insulator 1

1.1 Historical Overview of Topological Insulator 1

1.2 Crystal Structure 3

1.3 Electrical Properties 5

1.3.1 Electrical Band Structure 5

1.3.2 Angle-resolved Photoemission Spectroscopy (ARPES) 6

1.3.3 Transport Characterization 8

1.4 Quantum Anomalous Hall Effect 10

Chapter 2 Experimental Procedure 14

2.1 Sample Growth 14

2.1.1 Substrate Preparation 14

2.1.2 Molecular Beam Epitaxy (MBE) Growth 15

2.1.3 Reflection High-energy Electron Diffraction (RHEED) 17

2.2 Sample Characterization Methods 18

2.2.1 Physical Property Measurement System (PPMS) 19

2.2.2 Sample Configuration 20

2.2.3 Hall Resistance 21

2.2.4 Arrott Plot 23

2.2.5 Conductance Conversion 25

2.3 Ultra-low Temperature Transport Measurement 26

2.3.1 Operation Principle of Dilution Refrigerator 27

2.3.2 Sample Space and Superconducting Magnet 29
2.3.3 AC Resistivity Bridge 31
Chapter 3 Realization of the Axion Insulator State 33
3.1 Topological Magnetoelectric Effect 33
3.1.1 Basic Concepts 33
3.1.2 Requirements for Topological Magnetoelectric Effect 35
3.1.3 Previous Experiments 37
3.2 Realization of the Axion Insulator State in TI Heterostructures 39
3.2.1 Sample Configuration and Structural Characterization 39
3.2.2 Transport Characterization at 2K 42
3.2.3 Gate Dependence of Transport Properties 44
3.2.4 Exchange Coupling in Heterostructures 49
3.2.5 Magnetic Force Microscopy (MFM) Measurements 50
3.3 Conclusions and Discussion 52
Chapter 4 Crossover of Quantum Anomalous Hall to Topological Hall Effects 53
4.1 Chiral Spin Textures and Topological Hall Effect 53
4.1.1 Spin Textures 53
4.1.2 Origin of Chiral Spin Textures 57
4.1.3 Experimental Observations 57
4.1.4 Topological Hall Effect 60
4.2 Unifying Topological Hall and Quantum Anomalous Hall Effect 63
4.2.1 Sample Configuration 63
4.2.2 Sample Structure Characterization 65
4.2.3 Transport Results 65
4.2.4 Conductance Results 73
4.2.5 Angular Dependence of Topological Hall Effect 74
4.2.6 Thickness Dependence of Topological Hall Effect 75

4.3 Explanation and Discussion 78
4.3.1 Chiral Domain Walls 78
4.3.2 Theoretical Calculations 79
4.3.3 Discussion and Conclusion 82
Part II: Long-range superconducting proximity effect in Ni nanowire 86
Chapter 5 Superconducting Proximity Effect in Ferromagnet 86
5.1 Overview of Superconductivity 86
5.1.1 Microscopic Understanding – Bardeen Cooper Schrieffer Theory 87
5.1.2 Macroscopic Approach – Ginzburg-Landau Theory 90
5.2 Spin-triplet Superconductivity 92
5.3 Previous Studies on Superconducting Proximity Effect 95
Chapter 6 Sample Fabrication 99
6.1 Physical Vapor Deposition 99
6.2 E-beam lithography 102
6.3 Sample Configuration 104
Chapter 7 Long-range Superconducting Proximity Effect in Ni nanowire 106
7.1 Proximity Effect with Cu Buffer Layer 106
7.1.1 Proximity Effect without any Buffer Layer 106
7.1.2 Proximity Effect with CuNi Buffer Layer 107
7.1.3 Long-range Proximity Effect with Cu Buffer Layer 108
7.1.4 Proximity Effect with Au Buffer Layer 113
7.2 Possible Explanation of Long-range Proximity Effect in Ni 115
7.2.1 Possible Noncollinear Magnetic Profile Induced by CuO 115
7.2.2 Experimental Evidence of Magnetic CuO 117
7.2.3 Proximity Effect with Minimum Influence of CuO 120
7.3 Conclusion 124
References 125

List of Figures

Figure 1.1 Crystal structure of Bi_2Se_3 family 3D TI. (a) Crystal structure of Bi_2Te_3, Bi_2Se_3, Sb_2Te_3 with three primitive lattice vectors labeled as t1, t2, t3. Dashed box includes one QL. (b) Top view. (c) Side view. (d) Crystal structure of $(Bi_{1-x}Sb_x)_2Te_3$. Doped Sb atoms randomly replace Bi and lower the chemical potential while maintaining the same crystal structure.....3

Figure 1.2 Electrical band structure of 3D TI and magnetically doped 3D TI. (a) Band structure of Bi_2Se_3 family of 3D TI. The red and blue bands represent the bulk conduction and valence band, respectively, and the yellow Dirac cone is the surface state. Black arrows represent the spin of the electrons. (b) Schematic of electrons propagating on the surface of a 3D TI in real space when the Fermi surface is in the charge neutral point. (c) Band structure of the magnetically doped $(Bi_{1-x}Sb_x)_2Te_3$ film. A line connecting surface bandgap is the chiral edge state. (d) Schematic of chiral edge state in real space in a magnetically doped $(Bi_{1-x}Sb_x)_2Te_3$ film.....5

Figure 1.3 ARPES measurement on the electronic band structure of 3D TI. (a) Schematic of ARPES set-up. This figure is reproduced from https://en.wikipedia.org/wiki/Angle-resolved_photoemission_spectroscopy. (b) ARPES intensity maps of $Bi_{0.9}Sb_{0.1}$ with the photon energy of 29 eV. This figure is reproduced from Hsieh *et al.,* Nature, 2008. **452** (7190): p. 970-U5. (c) ARPES intensity map of the gapless surface state bands of cleaved Bi_2Te_3. The yellow arrow is the spin direction based on calculation. (d) Constant energy ARPES intensity map using photon energy of 35 eV. Figure (c) and (d) are reproduced from Hsieh *et al*., Physical Review Letters, 2009. **103** (14). 7

Figure 1.4 Electrical transport of a 5 QL $(Bi_{1-x}Sb_x)_2Te_3$ grown on STO substrate at 2 K. (a) $\mu_0 H$-dependent Hall traces at various V_g. (b) V_g-dependent Hall and longitudinal resistance at $\mu_0 H$ = 1 T. (c) Estimated Fermi level respective to Dirac-cone surface state at different V_g. 8

Figure 1.5 Experimental observation of QAH effect by ultra-low temperature electrical transport measurement. (a) Field-dependent Hall resistance ρ_{yx} under varying V_g in Cr-doped $(Bi_{1-x}Sb_x)_2Te_3$. The Fermi surface reaches charge neutral point V_g^0 at V_g = -1.5 V, and the ρ_{yx} becomes $e2h$. This figure is reproduced from Chang, C.Z., et al., Science, 2013. **340**(6129). (b) Field-dependent ρ_{xx} and ρ_{yx} at $V_g = V_g^0$ in V-doped $(Bi_{1-x}Sb_x)_2Te_3$. The coercive field increased to 1T. This figure is reproduced from Chang, C.Z., *et al*., Nature Materials, 2015. **14**(5).....12

Figure 2.1 The schematic of the MBE system. MBE growth is carried out in an ultra-high vacuum chamber at the pressure < 2×10^{-10} mbar. The substrate is mounted on a rotary stage with and heated by a radiant heater. Knudsen effusion cells are used for evaporating Bi, Sb, Te, Cr sources, and e-

gun is used for depositing V. RHEED system is used for *in situ* monitoring of the crystal quality during the growth……16

Figure 2.2 RHEED pattern taken from sample growth. (a) A typical RHEED pattern of $(Bi_{1-x}Sb_x)_2Te_3$ layer with the atomically flat crystalline surface. (b) A typical RHEED pattern of STO substrate prior to the growth. Kikuchi lines indicate a good reconstructed surface. 18

Figure 2.3 Physical property measurement system (PPMS). (a) Storage dewar and M6000 controller. (b) Block diagram of electrical connection. (c) Schematic of the storage dewar. (d) Schematic of the PPMS probe. It is submerged in the liquid ^{4}He bath. (e) Schematic of the cooling system and sample space. Figure (a), (d), and (e) are reproduced from Quantum Design website https://www.qdusa.com/. 20

Figure 2.4 Sample configuration in the transport measurement. (a) Photo of a typical sample with Hall bar geometry. (b) Schematic of the sample configuration. It shows the current flow direction, ρ_{yx} & ρ_{xx} leads, and gating voltage V_g. 21

Figure 2.5 Arrott plot of a Cr-doped TI (3QL)/non-doped (5QL)/Cr-doped TI (3 QL) heterostructure. The T_c of this sample is around 19 K. 24

Figure 2.6 Two common artifacts when conducting conductance conversion from resistance. (a) $\mu_0 H$-dependent ρ_{yx} and ρ_{xx} of V-doped TI showing QAH effect. (b) the 'zero plateau' of σ_{yx} around H_c. (c) $\mu_0 H$-dependent ρ_{yx} and ρ_{xx} of Cr-doped TI showing QAH effect. (d) the 'peak' overshoots quantized conductance $e2h$. 26

Figure 2.7 Operating principle of a dilution refrigerator. (a) The schematic diagram of a DR insert, the dilution circuit and other key components are labeled. (b) Picture of the DR insert used in our experiment with the shields removed. (c) Phase diagram of ^{3}He/^{4}He mixture[41]. (d) Picture of the experimental set-up of transport measurement, it is attached to the mixing chamber. (e) Picture of the sample puck and the sample. 28

Figure 2.8 AVS-47 AC resistivity bridge. (a) The front panel of AVS-47. The reference resistance R_r and the reference excitation voltage V_{ref} is adjustable. (b) The digital interface for AVS-47. (c) Block diagram that shows the working principle of AVS-47. Figure (a), (b), and (c) are reproduced from AVS-47 manual from http://www.picowatt.fi. 31

Figure 3.1 Schematics of the QAH insulator and the axion insulator shows TME effect. (a) The realization of the QAH effect in TI with the magnetizations of both top and bottom surfaces aligned to the same direction. (b) Axion insulator state with the magnetization and quantized Hall conductance of two surfaces in opposite directions. With the application of an electric field E_x, it

forms a circulating current that gives rise to a magnetic field B_x. This is a unique magnetoelectric effect for topological insulators and termed as the TME effect. 34

Figure 3.2 Proposed axion insulator structure and its $\mu_0 H$ dependence of σ_{yx}. (a) Schematic of a magnetic / nonmagnetic/magnetic TI sandwich heterostructures for realizing axion insulator state. (b) $\mu_0 H$ dependence of σ_{yx}, the blue and red arrows represent the magnetization alignment of magnetic TI layers. The axion insulator state occurs at $\mu_0 H_{c1} > \mu_0 H > \mu_0 H_{c2}$. It displays zero Hall conductance and anti-parallel magnetization alignment. This figure is reproduced from Wang, J., et al., Physical Review B, **92,** 081107 (2015). 35

Figure 3.3 'Zero-plateau' feature in uniformly doped TI. (a) $\mu_0 H$ dependence of σ_{yx} in Cr-doped $(Bi_{1-x}Sb_x)_2Te_3$ at different temperatures. σ_{yx} is quantized when the sample is magnetized and a 'zero-plateau' feature appears during the magnetization reversal. (b) $\mu_0 H$ dependence of ρ_{xx} at different temperatures. Huge peaks with resistance up to a few megaohms appear around H_c. (c) Schematic of samples' magnetization with randomly-formed multi-domains. Orange arrows and red color region represent upward magnetization while green arrows and blue color region represent the opposite direction. (d) Flow diagram of (σ_{xx}, σ_{yx}) of V-doped $(Bi_{1-x}Sb_x)_2Te_3$ films with thickness d = 6 nm (green), 8 nm (orange), 9nm (gray). The two dashed black semi-circles represent the scaling behavior of integer quantum Hall effect, while the red dashed semi-circle represents the QAH state. Figure (a - c) are reproduced from Kou, X., et al., Nat Commun, **6**, 8474 (2015); Figure (d) is reproduced from Grauer, S., et al., Phys Rev Lett, **118**, 246801 (2017). 38

Figure 3.4 Structural characterization of 3QL V-doped $(Bi_{1-x}Sb_x)_2Te_3$ / 4-6QL $(Bi_{1-x}Sb_x)_2Te_3$ / 3QL Cr-doped $(Bi_{1-x}Sb_x)_2Te_3$ sandwich heterostructure. (a) The schematic of the sample configuration and its cross-sectional STM image. The V-doped TI layer is labeled by blue color, while the Cr-doped layer is labeled by red color. (b) QAH effect of uniformly V-doped TI (blue curve), and Cr-doped TI (red curve) at 30 mK. H_c of V[14] is 1 T and that of Cr[9] is 0.15 T. (c - d) RHEED pattern of heat-treated STO substrate before growth and the 3-6-3 heterostructure after the growth. (e) The cross-sectional TEM image of 3-4-3 heterostructure and the EDS mapping of Cr and V element.....40

Figure 3.5 Electrical transport characterization of the best sample in each thickness configuration at 2 K. (a - d) V_g dependent ρ_{yx} and ρ_{xx} at 2 K of 2-4-2, 3-4-3, 3-5-3, and 3-6-3 heterostructures. The feature included inside the dashed box indicates the emergence of QAH effect. Figure (e - h) $\mu_0 H$-ρ_{yx} relation that displays a 'plateau' feature due to two H_c of V-/Cr- doped TI layers. 42

Figure 3.6 $\mu_0 H$ dependence of ρ_{xx}, σ_{xx}, ρ_{yx}, and σ_{yx} of the 3-4-3 heterostructure at 30 mK under different V_g. (a) -200 V, (b) -100 V, (c) -50 V, (d) 0 V, (e) 16 V, (f) +50 V, (g) +100 V, and (h) +200 V.....45
Figure 3.7 $\mu_0 H$ dependence of ρ_{xx}, σ_{xx}, ρ_{yx}, and σ_{yx} of the 3-5-3 heterostructure at 30 mK under different V_g. (a) -200 V, (b) -100 V, (c) -50 V, (d) 0 V, (e) 18 V, (f) +50 V, (g) +100 V, and (h) +200 V.....46
Figure 3.8 $\mu_0 H$ dependence of ρ_{xx}, σ_{xx}, ρ_{yx}, and σ_{yx} of the 3-6-3 heterostructure at 30 mK under different V_g. (a) -200 V, (b) -100 V, (c) -50 V, (d) -16 V, (e) 0 V, (f) +50 V, (g) +100 V, and (h) +200 V.....47
Figure 3.9 Minor loop of $\mu_0 H$ dependence of σ_{yx} at $V_g = V_g^0$ under T = 30 mK. (a) 3-4-3 heterostructure, (b) 3-5-3 heterostructure, (c) 3-6-3 heterostructure.....49
Figure 3.10 $\mu_0 H$ dependence of ρ_{yx} and corresponding MFM images of the 3-5-3 heterostructure. (a) $\mu_0 H$ dependence of ρ_{yx} at 5.3 K under V_g = 0 V. (b) $\mu_0 H$ dependence of magnetic domain contrasts (δf) from 0 T to 1 T. (c - j) The MFM images of selected $\mu_0 H$ respectively representing the magnetization alignment transiting from parallel upward, then antiparallel, and finally parallel downward. Corresponding Hall resistance is labeled by black circles in (a).....51

Figure 4.1 Spin textures. (a) Vortex with in-plane spins. (b) Vortex with out-of-plane core with $Q = \pm 12$. (c) Meron with surrounding spins radially pointing outward. (d) Meron with spins pointing inward. (c) Spin bubble with $Q = \pm 0$. (f) Spin bubble with $Q = \pm 1$. (g) Neel-type skyrmion projected from a hedgehog sphere. (h) Bloch-type skyrmion projected from a combed hedgehog sphere. These figures are reproduced from Liu, J. et al., 'Skyrmions: topological structures, properties, and applications.', CRC Press, 2016. 54

Figure 4.2 The spin configuration of domain walls. (a) Bloch-type domain wall. (b) Neel-type domain wall. (c) Domain wall with zero topological charge. (d) Chiral domain wall with a non-zero winding number. These figures are reproduced from Liu, J. et al., 'Skyrmions: topological structures, properties, and applications.', CRC Press, 2016.....55
Figure 4.3 Phase diagram for the formation of chiral spin textures. (a) Magnetic phase diagram of MnSi in *B*-*T* parameter space. Three phases were observed: conical, helical, and an 'A-phase' with skyrmion lattice. (b) The small angle neutron scattering data from a helical spin structure at 28.5 K under zero external fields. (c) The small angle neutron scattering result of skyrmion lattice under a finite field of 200 mT. (d - f) LSTM image of helical + skyrmion phase, skyrmion phase, and ferromagnetic + skyrmion phase of $Fe_{0.5}Co_{0.5}Si$ under finite fields. (g) – (h) The Lorentz TEM

observation is combined with a magnetic transport-of-intensity equation calculation to show the magnetic components of the helical and skyrmion phase. The spin direction is shown by the white arrows. (i) The magnetic phase diagram of $Fe_{0.5}Co_{0.5}Si$. The stars are corresponding to the *B* - *T* conditions in Figure (d - f). Figure (a - c) are reproduced from Muhlbauer, S., et al., Science, 2009. **323** (5916). Figure (d - i) are reproduced from Yu, X.Z., et al., Nature, 2010. **465** (7300). 58

Figure 4.4 TH effect in magnetic TI structures. (a) Schematic of a 2 nm $Cr_x(Bi_{1-y}Sb_y)_{2-x}Te_3$ / 5 nm $(Bi_{1-y}Sb_y)_{2-x}Te_3$ magnetic TI heterostructure. (b) Schematic of a 4 QL Mn-doped Bi_2Te_3. (c) Top gate-dependent Hall conductance of the Cr-doped TI / non-doped TI heterostructure at 2 K. The 'hump' feature emerges at negative top gating voltage. (d) Bottom gate-dependent Hall resistance of the Mn-doped TI at 1.5 K. The TH effect persists at both positive and negative gating voltages. Figure (a) and (c) are reproduced from Yasuda, K., et al., Nature Physics, 2016, **12**, 555-559. Figure (b) and (d) are reproduced from Liu, C., et al., Physical Review Letters, 2017, **119** (176809). 61

Figure 4.5 Schematic of the 3-5-3 sample and its RHEED pattern during the MBE growth. (a) Schematic of the 3QL $(Bi_{1-x}Sb_x)_{1.85}Cr_{0.15}Te_3$/5QL $(Bi_{1-x}Sb_x)_2Te_3$/3QL $(Bi_{1-x}Sb_x)_{1.85}Cr_{0.15}Te_3$ sample. (b) RHEED pattern of the heat-treated substrate. (c)-(e) RHEED patterns of the TI layer during each stage of the MBE growth. 64

Figure 4.6 HAADF-STEM image and EDS mapping of the 3-5-3 sample. (a) The HADDF-STEM image of the sample cross section. Te capping layer, the 11 QL heterostructure, STO substrate can be distinguished. (b) EDS map of the Cr ions of this 3-5-3 sample. 65

Figure 4.7 The $\mu_0 H$-dependent transport data at V_g = 0 V of 3-5-3 sample under various temperatures. (a) $\mu_0 H$ dependence of ρ_{xx} at varying temperatures under V_g = 0 V. (b) $\mu_0 H$ dependence of ρ_{yx}. At T = 30 mK, the quantized ρ_{yx} and the vanished ρ_{xx} suggest this sandwich sample in the QAH state when V_g = 0 V. ρ_{yx} deviates from quantized value as temperature increases. 66

Figure 4.8 Crossover of QAH to TH effects at T = 30 mK. (a - f) $\mu_0 H$ dependence of ρ_{yx} under varying V_g. The sample harbors a perfect QAH state when $V_g = V_g^0 = +20$ V. ρ_{yx} deviates from the quantized value and a "hump" feature appears in ρ_{yx} (green shadowed) when V_g is tuned away from V_g^0. Inset of (a - f): the offset resistance of ρ_{yx} when the external $\mu_0 H$ is swept upward and downward, which is used as TH component ρ_{yx}^{TH}.....67

Figure 4.9 $\mu_0 H$ dependence of ρ_{yx} of the 3-5-3 sample under different V_g and temperatures. (a) 60 mK, (b) 100 mK, (c) 200 mK, (d) 400 mK, (e) 600 mK, and (f) 1 K. 68

Figure 4.10 $\mu_0 H$ dependence of ρ_{xx} of the 3-5-3 sample under different V_g and temperatures. (a) 60 mK, (b) 100 mK, (c) 200 mK, (d) 400 mK, (e) 600 mK, and (f) 1 K. 69

Figure 4.11 TH component ρ^{TH}_{yx} at different V_g and T. (a) $\mu_0 H$ dependence of the ρ^{TH}_{yx} at varying V_g under T=30 mK. (b) $\mu_0 H$ dependence of the ρ^{TH}_{yx} when $V_g = V_g^{TH, max}$ at different T. Maximum ρ^{TH}_{yx} =1.65 K at T = 30 mK and disappears at T = 5 K. (c) The maximum ρ^{TH}_{yx} as a function of (V_g - V_g^0) at different T. ρ^{TH}_{yx} shows a peak denoted by the arrows when $V_g < V_g^0$. 70

Figure 4.12 $\mu_0 H$ dependence of ρ_{yx} of the 3-5-3 sample under V_g = -180 V at T = 30 mK......72

Figure 4.13 $\mu_0 H$ dependence of the Hall conductance σ_{xy} of the 3-5-3 sample under different V_g and T= 30 mK. (a) -200 V, (b) -120 V, (c) -80 V, (d) 90 V, (e) 200 V. Inset: the offset conductance σ_{xy}^{TH} when the external $\mu_0 H$ is swept upward (blue) and downward (red). 73

Figure 4.14 Tilt-angle dependence of TH effect for the 3-5-3 sample under V_g= -180V at T=2K. (a) Schematic showing the tilt-angle θ. The external $\mu_0 H$ is tilted at an angle θ from the normal of the film. (b-i) The ρ_{yx} of the 3-5-3 sample at the various angles of the $\mu_0 H$ inclination. (b) θ = 0º, (c) θ = 5º, (d) θ =1 0º, (e) θ = 20º, (f) θ = 30º, (g) θ = 40º, (h) θ = 50º, (i) θ = 60º. Inset of (b - i): the TH resistance ρ_{yx}^{TH} with the normal Hall and anomalous Hall contributions (ρ_{yx}^{NH} and ρ_{yx}^{AH}) subtracted. This is accomplished by subtracting the red curve from the blue curve. In the inset, the blue (red) curve represents the trace in sweeping $\mu_0 H$ upward (downward).....74

Figure 4.15 $\mu_0 H$ dependence of ρ_{yx} at $V_g = V_g^0$ and V_g = -200 V of the samples 5 QL $(Bi_{1-x}Sb_x)_2Te_3$ film sandwiched magnetic TI layers with different thicknesses at T = 500 mK. (a) 1-5-1, (b) 2-5-2, (c) 3-5-3, (d) 4-5-4, and (e) 5-5-5. Inset: the offset resistance, ρ^{TH}_{yx} at V_g = -200 V between upward (blue) and downward (red) $\mu_0 H$ sweep. 76

Figure 4.16 $\mu_0 H$ dependence of ρ_{yx} at $V_g = V_g^0$ and V_g = -200 V of samples top and bottom 3 QL Cr doped $(Bi_{1-x}Sb_x)_2Te_3$ layers sandwiched by undoped TI films with different thicknesses at T = 500 mK. (a) 3-1-3, (b) 3-2-3, (c) 3-3-3, (d) 3-4-3, (e) 3-5-3, (f) 3-6-3, and (g) 3-7-3. Inset: the offset resistance, ρ^{TH}_{yx}, at V_g = - 200 V between upward (blue) and downward (red) $\mu_0 H$ sweep. .77

Figure 4.17 Chiral magnetic domain walls and theoretical interpretations of the crossover between the QAH and TH effects. (a) The formation of the chiral magnetic domain walls during magnetization reversals. (b) The spin distribution of the magnetic TI in a zoomed-in area in Fig. (a). (c) The energy dispersions of the SS and QW bands in the magnetic TI sandwich heterostructures. (d-e) χxz as a function of energy for the QW and SS states, respectively, under different asymmetric potentials U. (f) The QW contribution to χxz, SS contribution to χxz, and total χxz in the magnetic TI sandwich heterostructures when U = 0.02. $qx = 0.005$ Å $- 1$ and $qy = 0$ in Fig. (d - f). 80

Figure 4.18 The formation of 'hump' feature in $SrIrO_3/SrRuO_3/SrTiO_3$ sandwich structures by two AH channels with opposite signs. (a) The schematic of two AH channels with opposite signs. (b) The simplified crystal structure of $SrIrO_3/SrRuO_3/SrTiO_3$ shows the exact locations for

two AH channels (c) Different 'hump' features observed in the sample. (d-f) Experimental observations interpreted by the addition of Rxy, IAH and Rxy, IIAH. This figure is reproduced from Groenendijk, D. J., et al., arXiv:1810.05619, (2018). 83

Figure 4.19 The control sample with enhanced Hc (a) Schematic of the control sample: 5 QL V-($Bi_{1-x}Sb_x)_2Te_3$ on 3-5-3 sample heterostructure. (b-d) $\mu_0 H$ dependence of the ρ_{yx} under V_g = -50 V (b), 0 V (c), 200 V (d). Because of the exchange coupling between the 5 QL V-($Bi_{1-x}Sb_x)_2Te_3$ and the top 3 QL Cr-($Bi_{1-x}Sb_x)_2Te_3$, the coercive field ($\mu_0 H_{c1}$) of the top Cr-doped TI layer increases to 0.25 T at 2 K, while the coercive field ($\mu_0 H_{c2}$) of the bottom Cr-TI stays at 0.08 T.....84

Figure 5.1 Different pairing types of superconducting Cooper pair and the creation mechanism of 'equal-spin' triplet. (a) The schematics of spin-singlet and triplet. Spin-singlet has opposite spin directions and $S = 0$, while for the spin-triplet, $S = 1$. (b) Electrons would acquire a spin direction dependent phase shift when entering a spin-polarized barrier. Blue curves indicate the wave function of spin-up electrons, while red curves represent that of spin-down electrons, so they will have a relative phase shift ϑ that gives rise to a singlet-triplet mixing state. (c) A buffer ferromagnetic layer with different magnetization direction than the strong bulk ferromagnet would create 'equal-spin' triplets that could survive in a ferromagnet. Figure (b - c) are reproduced from Eschrig, M., *Phys. Today*, *64* (1), p.43. 93

Figure 5.2 Observation of the spin-triplet pairing in mesoscopic superconducting/ ferromagnetic (SF) junctions. (a) Long-ranged supercurrent is observed in the ferromagnetic half metal CrO_2 by using NbTiN electrodes. (b) I - V relation indicates a clear zero resistance supercurrent which is presumably caused by spin-triplet. (c) Schematics of the SF junction using Nb as the superconductor and Co as the ferromagnet. Ho with conical magnetization is used as the magnetic inhomogeneity to induce spin-triplet pairing. (e) I_cR_N – Co thickness relation of Nb/Ho/Co/Ho/Nb junction. Inset shows I_cR_N – Co thickness in the junctions without Ho buffer layer. (d) Schematic of SF junction using Co/Ru/Co as strong ferromagnet and Pd/Ni as a weak ferromagnetic layer F'/F". Cu buffer layers are also used to magnetically isolate those magnetic layers. (f) I_cR_N – Co thickness relation of the junction shown in Fig. (d). Red dots represent the data points acquired from the junction with F'/F" layers, while the black dots represent the exponential drop of spin-singlet where F'/F" layers are absent. Figure (a - b) are reproduced from Keizer, R. S., et al., *Nature*, **439**, 825-827 (2006). Figure (c - d) are reproduced from Eschrig, M., *Physics Today*, **64** (2011). Figure (e) is reproduced from Robinson, et al., *Science*, **329**, 59-61 (2010). Figure (f) is reproduced from Khaire, T. S., et al., *Phys Rev Lett*, **104**, 137002 (2010).....96

Figure 5.3 Sample configurations of the experiments observed long-range superconducting proximity effect in Co nanowire with FIB-assisted superconducting W electrodes / inducer. (a) SEM image of Co NW contacted by W electrodes and its resistance is measured by four-probe measurement. (b) SEM image of Co NW contacted by Pt electrodes; a W inducer is deposited in the middle of the NW to give rise to superconducting proximity effect. (c) Schematic of the sample configuration in figure (b). Figure (a) is reproduced from Wang, et al., *Nature Physics*, **6**, 389-394 (2010). Figure (b - c) are reproduced from Kompaniiets, et al., Applied Physics Letters, 104 (2014). 98

Figure 6.1 Physical vapor deposition (PVD) methods for sample growth. (a) Schematic of a thermal evaporation chamber. The evaporation source (shown in red) is melted in a W filament and the vapor will reach and condense on the face-down substrate. The process can be controlled by source shutter and monitored by the thickness monitor. A cryo-panel can be cooled by LN_2 and improve the background vacuum. (b) Schematic of a magnetron sputtering machine. The target is installed on top of a magnetron source and a high voltage will accelerate the ionized Ar atoms and bombard on the target surface. The ejected target material is trapped by the magnetic field and deposited on the substrate. (c) Image of a W filament in a shape of 'board' with Al_2O_3 coating. (d) Image of a magnetron gun used in the sputtering machine. Figure (c) is reproduced from https://www.lesker.com. Figure (d) is reproduced from https://moorfield.co.uk/.....100

Figure 6.2 Schematics of the e-beam lithography process. (a) Spin-coating of the e-beam resist on top of SiO_2/Si substrate. (b) The solubility of the resist would be reduced (in a costume pattern, shown in blue) once scanned by electron beams. (c) Regions of exposed resist will be dissolved after being immersed into the developer. (d) During the deposition, the vaporized materials will either condense on the e-beam resist or the bare substrate in the resist-removed region. (e) The pattern is left on the substrate once it is soaked into the lift-off solvent. 103

Figure 6.3 The sample configurations of nanowire structure. (a) The pattern fabricated in the lithography process. The long leads and pads are used for making electrical contacts between NWs and transport measurement system. (b) A typical image for the NW and electrodes from an optical microscope. (c) Schematics of the NW configuration in side view. The supercurrent can flow through the ferromagnetic Ni NW either in a 'bottom-up' or 'top-down' manner. (d) The superconducting proximity range can be characterized by the ratio of superconducting resistance drop to normal resistance.....105

Figure 7.1 *R-T* and R-$\mu_0 H$ property of a Ni NW measured by the superconducting Nb electrodes without any buffer layer. Dots in the graphs are individual data points and the lines are the guide to the eye. (a) The resistance of *Sample 1* starts to drop at 1.5 K, and drops 0.8 % down to 0.5 K, suggesting the proximity range of superconducting singlet is 2 nm in the ferromagnet. The inset is the schematic of *Sample 1* in side view. (b) $\mu_0 H$ dependence of resistance shows decreasing B_c and resistance drop as temperature increases. The inset shows contact resistance from the 2-terminal measurement, indicating the $T_c \sim 8$ K of Nb electrodes……107

Figure 7.2 *R-T* relation of a Ni NW measured by the superconducting Nb electrodes with a Cu (1 nm)/CuNi (1 nm)/Cu (1 nm) buffer layer. The superconducting drop of *Sample 2* indicates a proximity range of 8 nm. The inset on the upper left is R-H relation and the one at the right corner is the schematic of *Sample 2* in side view. 108

Figure 7.3 *R-T* and R-$\mu_0 H$ property of a Ni nanowire measured by the superconducting Nb electrodes with a Cu buffer layer. (a) The resistance of *Sample 3* starts to drop at 3 K, and drops 25 % down to 0.2 K, suggesting a superconducting proximity range of 65 nm in Ni NW. The inset is the schematic of *Sample 3* in side view. (b) R-$\mu_0 H$ relation shows decreasing B_c and resistance drop as temperature increases, the dots in the graph are individual data points and the lines are the guide to the eye. The inset shows contact resistance from the 2-terminal measurement, indicating the Tc ~ 8 K of Nb electrodes. A resistive upturn shows up under 3 K. 109

Figure 7.4 *R-T* and *R-$\mu_0 H$* property of two Ni nanowires deposited on Cu/Nb electrodes. (a) *R-T* curve of *Sample 4* suggests a superconducting proximity range of 35 nm with Tc ~ 8 K at zero field. The resistance drop gradually vanishes with the application of *H*. The inset is the schematic of *Sample 4* in side view. (b) R-$\mu_0 H$ curve of *Sample 4* shows $B_c \sim 4$ T at 2 K. B_c and the amount of resistance drop decrease as temperature increases. The inset shows contact resistance from the 2-terminal measurement. (c) *R-T* graph of *Sample 5* suggests a proximity range of 136nm with $T_c \sim 8$ K at $H = 0$ and decreases with the application of *H*. The inset is the schematic of *Sample 5* in side view. (d) R-$\mu_0 H$ curve of *Sample 5* shows $B_c \sim 6$ T at 0.5 K, and $B_c \sim 4$ T at 2 K. B_c and the amount of resistance drop decrease as temperature increases. The inset shows contact resistance from the 2-terminal measurement. 111

Figure 7.5 Normalized resistance v.s. current relation under different temperatures of (a) *Sample 3,* (b) *Sample 4,* and (c) *Sample 5*. The superconducting proximity effect is gradually diminishing as the excitation or temperature increases, indicated by the decreasing resistance drop of ferromagnetic Ni NW. (d) Normalized resistance-*T* relation of the three samples. 112

Figure 7.6 *R-T* and *R-$\mu_0 H$* property of a Ni NW measured by the superconducting Nb electrodes with Au interlayer. (a) *R-T* graph of *Sample 6*. The inset is the schematic of *Sample 6*

in side view. (b) *R*-$\mu_0 H$ of *Sample 6*. The inset shows contact resistance from the 2-terminal measurement. (c) *R-T* graph of *Sample 7*. The inset is the schematic of *sample 7* in side view, where the Au layer has covered the whole Ni wire. (d) *R*-$\mu_0 H$ of *Sample 7*. The inset shows contact resistance from the 2-terminal measurement. 113

Figure 7.7 *M-H* relation of controlled samples. (a) M-H curve of a 4 μm × 4 μm Si substrate with 500 nm SiO2 on the surface. (b) M-H relation of a 40 nm Nb sputtered on the substrate. The inset shows the *M-H* curve of the sample under 2 K. No ferromagnetic impurity is found by the SQUID measurement. 117

Figure 7.8 *M-H* relation of 3nm naturally oxidized Cu evaporated on 4 μm × 4 μm SiO_2/Si Substrate with / without 40 nm Nb layer. (a) Raw Data acquired from the sample. (b) *M-H* relation of 3 nm naturally oxidized Cu layer with background subtraction. (c) A number of such Cu films from different batches were tested, similar M-H relations were found. Thin Film 1 is the film shown in Fig. (a) and (b). (d) *M-H* relation of 3 nm naturally oxidized Cu layer on top of 40 nm Nb. Inset shows the diamagnetism of superconductivity. 118

Figure 7.9 *M-H* relation in thicker Cu layer or thin Cu layer with minimum exposure to atmosphere. (a) *M-H* relation of 10 nm naturally oxidized 10nm Cu evaporated on a 4 μm × 4 μm Si substrate with 500 nm SiO_2. Cu and Nb are deposited without breaking the vacuum. (b) *M-H* relation of 3 nm Cu layer covered by a 40 nm Nb layer grown on the Si substrate. Ferromagnetism vanished in these two cases, indicating the anti-ferromagnetism of CuO.....119

Figure 7.10 *R-T* and *R*-$\mu_0 H$ relation of *Sample 8*, where Cu/Nb are deposited consecutively in the same chamber. (a) *R-T* relation under the different magnitude of the external field. The inset is the schematic of *Sample 8* in the side view. (b) *R*-$\mu_0 H$ property under different temperatures. The inset shows contact resistance from the 2-terminal measurement. 121

Figure 7.11 *R-T* and *R*-$\mu_0 H$ relation of Ni NW with 10 nm Cu interlayer. (a) *R-T* relation under the different magnitude of the external field of *Sample 9,* where Cu/Nb are deposited without breaking the vacuum. The inset is the schematic of *Sample 9* in the side view. (b) *R*-$\mu_0 H$ property under different temperatures of *Sample 9*. The inset shows contact resistance from the 2-terminal measurement. (c) *R-T* relation under different magnitude of the external field of *Sample 10*, where Nb/Cu are sputtered prior to Ni NW. CuO is presented at the Cu/Ni interface. The inset is the schematic of *Sample 10* in the side view. (b) *R*-$\mu_0 H$ property under different temperatures of *Sample 10*. The inset shows contact resistance from the 2-terminal measurement. 122

List of Tables

Table 2.1 The typical growth condition of doped/non-doped TI layers. Bi, Sb, Te, and Cr are evaporated from Kundsen effusion cell, and the table shows their typical temperatures during the growth process. The power of e-gun used for depositing V is also shown above. The temperature can be slightly adjusted (up to ±20 °C) to increase/decrease the sources' flux to tune the chemical potential of the sample into charge neutral point. 16

Table 7.1 Summary of NW structure and properties presented in this dissertation. *Sample 1* has no buffer layer and it shows superconducting proximity range consistent with conventional theory. *Sample 2, Sample 6, and Sample 7* are showing a similar level of proximity range, indicating a slight enhancement due to the buffer layer. *Sample 3* to *Sample 5* display surprising long-range proximity effect when a naturally oxidized thin Cu layer is acting as the buffer layer. *Sample 8* to *Sample 10* will be presented in the next section to show that proximity range dramatically decreases if we reduce the amount of CuO or the magnitude of its magnetism.....115

Acknowledgment

My six years of Ph.D. is full of surprising but interesting adventures. It has granted me the courage and power to face the challenges yet to come, and at the end of this long journey, I would like to thank all the people who helped me along the way.

I want to thank my advisor Dr. Moses Chan and Dr. Cui-zu Chang. I have benefited from their dedications and insights at every step of my research. Not only had they taught me how to deal with technical difficulties, but also showed me the right attitude towards life and science. My special thank goes to my collaborator, Di Xiao. Most of my experiments would be impossible without his hard work. I would like to thank Dr. Chaoxing Liu, Dr. Nitin Samarth, Dr. Jainendra Jain and Dr. Roman Engel-Herbert for their instructions.

My labmates have helped me with equipment training, data analysis, and troubleshooting. I want to thank Dr. Weiwei Zhao for his patience and availability whenever I encountered a problem. He is a role model to me on treating families and colleagues. I also felt immense gratitude to Dr. Jae-ho Shin, who guided me through a lot of sleepless nights doing experiments. I also want to thank Pavlo Bulanchuk, Dr. Fei Wang, Dr. Morteza Kayyalha, Yifan Zhao, Run Xiao, Lin Zhang, Ruoxi Wang, Dr. Ludi Miao, Dr. Renzhong Du, Dr. Shiming Lei, Dr. Yu Pan for their help.

My deepest gratitude goes to my family for their unfailing love and support throughout my life. Finally, I want to thank my girlfriend, Xueyuan Jiang, for her company and support, and my life would never be complete without her.

I gratefully acknowledge the funding provided by NSF grant DMR-1539916 (Penn State 2DCC-MIP), DMR-1420620 (Penn State MRSEC), DMR-1539916, ONR grant N-000141512370, and DOE grant DE-SC0019064.

Part I: Quantum transport in magnetic topological insulator heterostructure

Chapter 1

Introduction of Topological Insulator

1.1 Historical Overview of Topological Insulator

Topological insulator (TI), a new state of matter that has insulating interior but conducting boundary, has drawn great research attention since the first experimental observation of topological property in a real material. In 2007, motivated by the theoretical prediction[1], König *et al.*[2] discovered a two-dimensional (2D) topological insulator state (quantum spin Hall state) in HgTe/CdTe quantum well structure, featuring an insulating surface state and two counter-propagating one-dimensional (1D) conducting edge channels. The most important ingredient to this novel effect is the strong spin-orbital coupling, which pushes the electrons from valence-band-edge state above the conduction-band-edge state, leading to the inverted band structure and non-trivial topology that is totally different from conventional band insulator.

The concept of 2D TI successfully extended to 3D regime by the prediction of another strong spin-orbital coupling material[3], $Bi_{1-x}Sb_x$, followed by the verification of its surface state through angle-resolved photoemission spectroscopy (ARPES)[4]. In a 3D TI, the bulk state has an inverted band structure and an insulating gap (the gap size is ~ 0.3 eV, meaning its non-trivial topology persists at room temperature), while the surface state holds a single Dirac cone protected by time reversal symmetry with linear dispersion[5-7]. The family of 3D TI soon expanded to include other three layered materials[8], Bi_2Te_3, Bi_2Se_3, Sb_2Te_3.

Another milestone of topological physics, the experimental realization of quantum anomalous Hall (QAH) effect, was firstly achieved by Chang *et al.* in 2013 on molecular-beam-epitaxy grown Cr-doped $(Bi_{1-x}Sb_x)_2Te_3$. In this magnetically doped 3D TI[9-13], a zero longitudinal resistance, as well as a quantized Hall conductance, can be unambiguously observed by electrical transport measurement, even when the magnetic field is withdrawn. This peculiar transport response is due to the formation of a conducting edge channel, known as chiral edge state, in which the electron momentum is locked to one direction perpendicular to the polarized spin. Till now, the quantized anomalous Hall state has only been reached in Cr-[9] and V-[14] doped $(Bi_{1-x}Sb_x)_2Te_3$ thin film, and mechanically exfoliated $MnBi_2Te_4$ (although the magnetic field is required to maintain QAH state in this material)[15]. The realization temperature of QAH state also increased from tens of millikelvin to 1.5 K in magnetically doped TI systems with the effort of different groups[16-17], and the newly-discovered intrinsic magnetic TI, $MnBi_2Te_4$, pushed the temperature up to 4.5 K[15]. The studies on the magnetic TI not only provide an ideal platform to engineer fundamental physics models[18-20], but also pave the way of the future application in room-temperature low-power-consumption spintronic for microelectronic circuits[21].

1.2 Crystal Structure

The bulk $Bi_{1-x}Sb_x$ crystal is a substitutional alloy without well-defined electronic band structure due to its random ordering of Bi and Sb atom in the crystal structure. However, Bi_2Te_3, Bi_2Se_3, Sb_2Te_3 are all layered materials with the identical rhombohedral crystal structure. It belongs to space group D_{3d}^5 with a triangle lattice within each layer, and five of atomic layers is defined as a quintuple layer (QL).

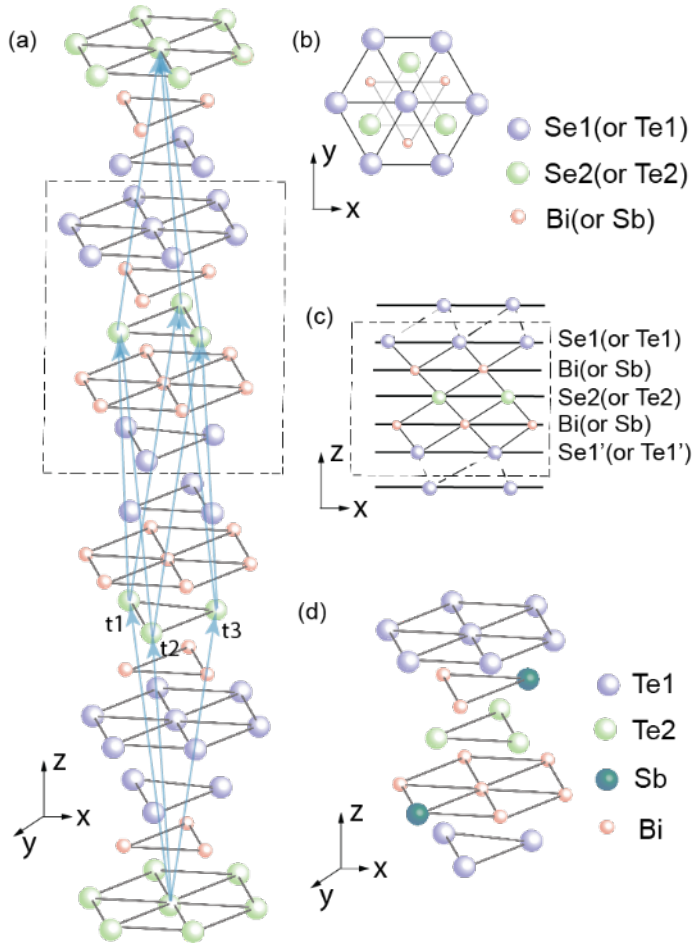

Figure 1.1 Crystal structure of Bi_2Se_3 family 3D TI. (a) Crystal structure of Bi_2Te_3, Bi_2Se_3, Sb_2Te_3 with three primitive lattice vectors labeled as t1, t2, t3. Dashed box includes one QL. (b) Top view. (c) Side view. (d) Crystal structure of $(Bi_{1-x}Sb_x)_2Te_3$. Doped Sb atoms randomly replace Bi and lower the chemical potential while maintaining the same crystal structure.

As seen in Fig. 1.1a, each quintuple layer consists of two equivalent Se/Te atoms (shown as Se1/Te1 and Se1'/Te1'), two equivalent Bi/Sb atoms (shown as Bi1/Sb1 and Bi1'/Sb1'), and a second Se/Te atom (shown as Se2/Te2). Each quintuple layer is terminated by Se/Te layers and

adjacent quintuple layers are bonded by Van der Waal force, while Bi/Sb and Se/Te atoms within a quintuple layer are strongly combined by chemical bonding.

In order to display topological properties in transport measurement, the chemical potential (or the Fermi surface) of the sample must be tuned closed to the Dirac point (or so-called 'charge neutral point' when the Dirac cone is gapped). However, the electrical transport (will be shown in Sec. 1.3.3) and ARPES measurement have proved that Bi_2Se_3 and Bi_2Te_3 exhibit n-type feature, meaning that the Fermi surface resides above the Dirac point, corresponding to the electron charge carrier. In Sb_2Te_3, Fermi surface is below the Dirac point, and the material is p-type.

In these 3D TIs, although the Fermi surface can be tuned by electrostatic gating technique, the tuning range is limited and the Dirac point is still far away. The most efficient way to control the level of the Fermi surface is doping impurities that can introduce the opposite type of charge carrier. Specifically, since Bi and Sb belong to the same element group, if Bi is doped into Sb_2Te_3 (Fig. 1.1d), Sb atoms can be substituted by Bi without disturbing crystal structure and topological property, while the Fermi surface rises significantly. The product TI, $(Bi_{1-x}Sb_x)_2Te_3$ becomes an ideal base material to host QAH effect. All the magnetic TI heterostructures studied in this dissertation are thus based on this material.

1.3 Electrical Properties

1.3.1 Electrical Band Structure

In the Bi_2Se_3 3D TI family, the strong spin-orbital coupling of heavy elements causes the crossing of the conduction and valence band, then reopens a gap in an inverted ordering[3]. This inverted band structure introduces a non-zero topological invariant[3, 22-23] ν_2. ν_2 equals to 1 in TI, while in vacuum or a trivial insulator, ν_2 is 0. The discontinuity of the ν_2 between the TI and the vacuum / substrate gives rise to a gapless Dirac cone on their interface (the surface of the TI), as shown in Fig. 1.2a.

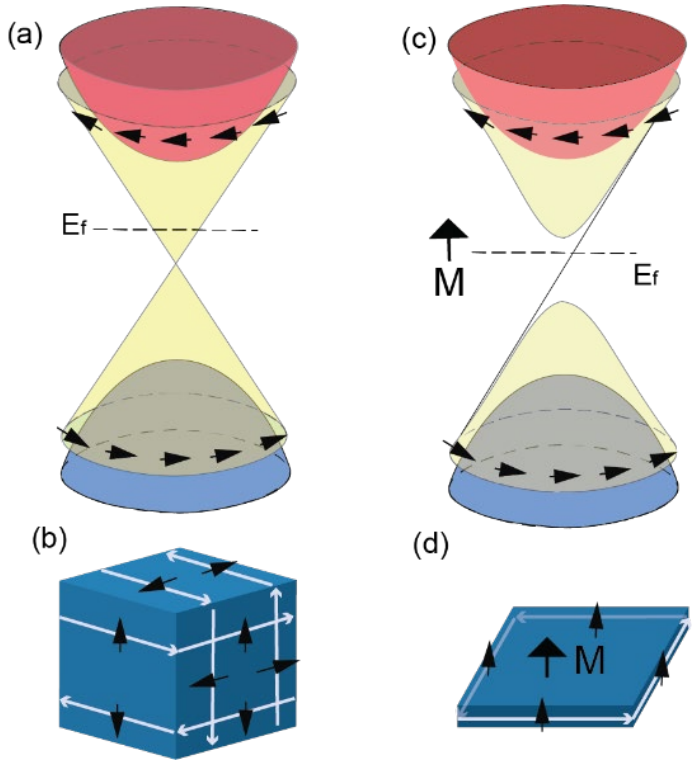

Figure 1.2 Electrical band structure of 3D TI and magnetically doped 3D TI. (a) Band structure of Bi_2Se_3 family of 3D TI. The red and blue bands represent the bulk conduction and valence band, respectively, and the yellow Dirac cone is the surface state. Black arrows represent the spin of the electrons. (b) Schematic of electrons propagating on the surface of a 3D TI in real space when the Fermi surface is in the charge neutral point. (c) Band structure of the magnetically doped $(Bi_{1-x}Sb_x)_2Te_3$ film. A line connecting surface bandgap is the chiral edge state. (d) Schematic of chiral edge state in real space in a magnetically doped $(Bi_{1-x}Sb_x)_2Te_3$ film.

This surface state is represented by the Hamiltonian[24-25],

$$H = v_F(-k_y\sigma_x + k_x\sigma_y),$$

in which v_F is Fermi velocity and σ_x, σ_y are Pauli matrices. This Hamiltonian shows that the spin is always perpendicular to the momentums (Fig. 1.2a), and in the real space (Fig. 1.2b) the electron with the different spin will move in an opposite direction.

1.3.2 Angle-resolved Photoemission Spectroscopy (ARPES)

Experimentally visualizing the electronic surface band structure of a 3D TI becomes possible with angle-resolved photoemission spectroscopy (ARPES). The schematic of the ARPES system is shown in Fig. 1.3a. A monochromatized light with preset photon energy hν is generated by a radiation source, then interacts with the electrons on the surface of the sample. The electrons will overcome the electron binding energy E_B and the work function ϕ, and be emitted from the sample to all directions with the kinetic energy E_{kin} = hν - E_B - ϕ. When photoelectrons pass through a hemispherical analyzer, their kinetic energy and emission angle will be resolved. Due to the transitional symmetry, the in-plane momentum of the photoelectron $K_{||}$ and the initial electron $k_{||}$ have the relation of $K_{||} = k_{||} = \frac{1}{\hbar}\sqrt{2mE_{kin}}\sin\theta$. Therefore, we can deduce the energy dispersion relation E(k) of the sample. Since the perpendicular momentum $k_\perp$ is not conserved due to abrupt potential change across the sample surface, ARPES is particularly useful and convenient to study the electronic band structure of 2D materials and the surface state of TI materials.

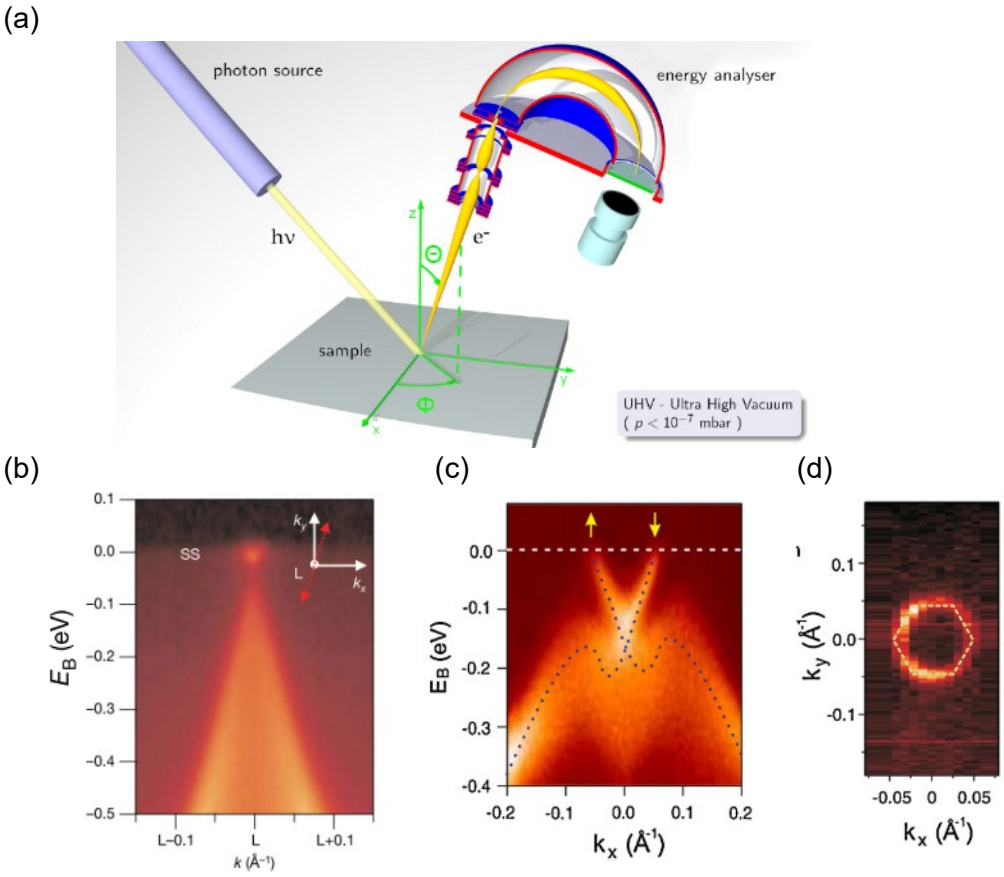

Figure 1.3 ARPES measurement on the electronic band structure of 3D TI. (a) Schematic of ARPES set-up. This figure is reproduced from https://en.wikipedia.org/wiki/Angle-resolved_photoemission_spectroscopy. (b) ARPES intensity maps of $Bi_{0.9}Sb_{0.1}$ with the photon energy of 29 eV. This figure is reproduced from Hsieh *et al.,* Nature, 2008. **452** (7190): p. 970-U5. (c) ARPES intensity map of the gapless surface state bands of cleaved Bi_2Te_3. The yellow arrow is the spin direction based on calculation. (d) Constant energy ARPES intensity map using photon energy of 35 eV. Figure (c) and (d) are reproduced from Hsieh *et al*., Physical Review Letters, 2009. **103** (14).

Figure 1.3b and c display the ARPES intensity mapping of the $Bi_{0.9}Sb_{0.1}$ and Bi_2Te_3 sample, which clearly show the gapless surface band with linear dispersion. Also, in Fig. 1.3d, the constant energy ($h\nu$ = 35 eV) ARPES intensity map shows a circle in the k_x-k_y plane. These observations are consistent with the Dirac-cone-like surface state in 3D TI.

1.3.3 Transport Characterization

The electrical transport measurement provides another reference for the band structure. Figure 1.4a shows the field dependent Hall resistance at 2 K of a 5 QL $(Bi_{1-x}Sb_x)_2Te_3$ grown by molecular beam epitaxy (MBE) technique on the $SrTiO_3$ (STO) substrate, and Bi/Sb ratio is fine-tuned so that the Fermi surface is closed to the Dirac point, i.e., charge neutral point.

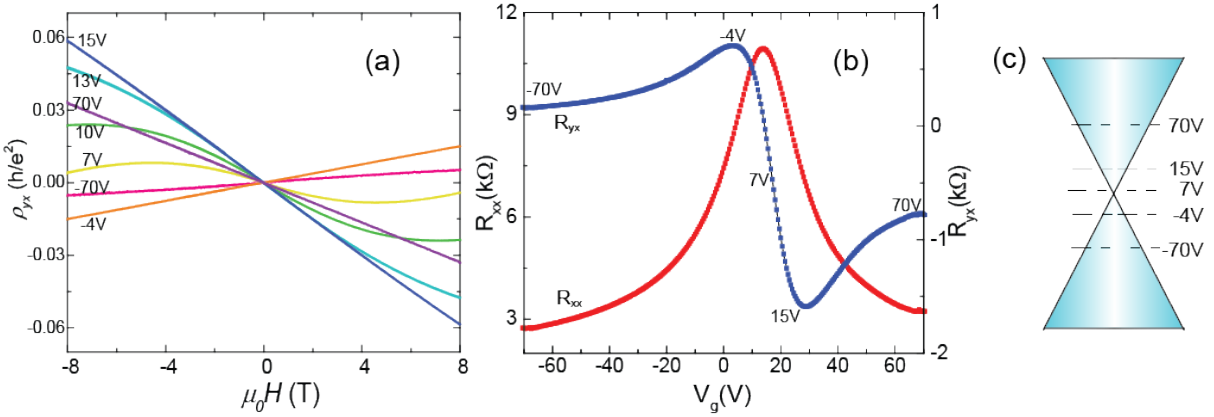

Figure 1.4 Electrical transport of a 5 QL $(Bi_{1-x}Sb_x)_2Te_3$ grown on STO substrate at 2 K. (a) $\mu_0 H$-dependent Hall traces at various V_g. (b) V_g-dependent Hall and longitudinal resistance at $\mu_0 H = 1$ T. (c) Estimated Fermi level respective to Dirac-cone surface state at different V_g.

By applying a gating voltage at the bottom of the substrate, the different type of carrier can be injected into the film. The chemical potential rises when applying a positive voltage, and decreases with a negative gating voltage. As we can see from Figure 1.4a, at $V_g = 70$ V and 15 V, the Hall coefficient is negative, indicating an n-type carrier in the system. The carrier density is calculated by $n_{2D} = \frac{1}{eR_H}$, where e is the charge of an electron, and R_H is the Hall coefficient. With a steeper slope, n_{2D} at $V_g = 15$ V is lower than that of $V_g = 70$ V, because the Fermi surface is closer to the Dirac point at $V_g = 15$ V. When $V_g = 7$ V, 10 V, 13 V, the Hall trace shows a non-linear behavior due to the crossing of Dirac point. At $V_g = -4$ V and -70 V, Hall coefficient becomes positive, meaning the charge carrier is converted to p-type. Figure. 1.4b shows the V_g - dependent

Hall resistance at 1 T. The magnetoresistance (red curve) displays a peak around 10 V, which indicates the smallest carrier density as the Fermi surface is the closest to the Dirac point. The Hall resistance (blue curve) shows a typical ambipolar behavior[26], corresponding to the switch of carrier type when crossing the Dirac point. The Fermi level positions of different V_g respective to the surface-state Dirac cone are illustrated in Figure 1.4c.

1.4 Quantum Anomalous Hall Effect

Another prominent breakthrough in topological physics is the experimental observation of the QAH effect. In magnetically doped 3D TI film, the time-reversal-symmetry in the Dirac-cone-like surface state is broken by exchange coupling of the magnetization normal to the sample surface. The surface state Hamiltonian can be expressed as,

$$H = v_F(-k_y\sigma_x + k_x\sigma_y) + m\sigma_z = \boldsymbol{d}\cdot\boldsymbol{\sigma},$$

where m is a material-related parameter, $\boldsymbol{d} = (-v_F k_y, v_F k_x, m)$, whose unit vector $\hat{\boldsymbol{d}} = \boldsymbol{d}/|\boldsymbol{d}|$ determines the topological property of the system, σ are the Pauli matrices for spins.

The electron band structure can be topologically characterized by the Chern number,

$$C = \frac{1}{4\pi}\sum_{top+bottom}\int_{\boldsymbol{BZ}}(\partial_{k_x}a_y - \partial_{k_y}a_x)dk_x dk_y,$$

where $a_{x(y)} = -i\sum_n\langle n\boldsymbol{k}|\frac{\partial}{\partial k_{x(y)}}|n\boldsymbol{k}\rangle$, $a = (a_x, a_y)$ is the Berry curvature, and the total Chern number consists of the integrals from both the top and bottom surface of a magnetic TI film[24-25]. Berry curvature a is the phase picked up by the wave function in an infinitely small loop around point (k_x, k_y) in momentum space. It can also be regarded as an equivalent magnetic field acting in the k-space. If we defined $\hat{\boldsymbol{d}}$ as the mapping from the momentum $\boldsymbol{k}$ to the unit vector $\hat{\boldsymbol{d}}$ on the sphere, we have

$$C = \frac{1}{4\pi}\sum_{top+bottom}\int_{\boldsymbol{BZ}}\hat{\boldsymbol{d}}\cdot(\frac{\partial\,\hat{\boldsymbol{d}}}{\partial k_x}\times\frac{\partial\,\hat{\boldsymbol{d}}}{\partial k_y})dk_x dk_y$$

Since $\hat{\boldsymbol{d}}\cdot(\frac{\partial\,\hat{\boldsymbol{d}}}{\partial k_x}\times\frac{\partial\,\hat{\boldsymbol{d}}}{\partial k_y})$ is the Jacobian of this mapping, C corresponds to the area $\hat{\boldsymbol{d}}$ covers when it integrates over the Brillouin zone. As we can see from the expression of $\boldsymbol{d}$, $\hat{\boldsymbol{d}}$ vector is

normal to the plane (direction is related to the sign of magnetization) when $k \to 0$ and lies in-plane when $k \to \infty$, so the integral leads to half of a unit sphere on one surface. If the top and bottom surface have the same magnetization, we will have $C = \pm 1$, meaning the band gap opened by magnetization is topologically non-trivial, and there will be a topology-protected boundary state on the 1D sample edge, as shown in Fig. 1.2c.

This edge state is non-dissipative with all the electrons spin-polarized and propagating along one direction (Fig. 1.2d), which is termed as chiral edge state. Experimentally, when the chemical potential is tuned into the exchange band gap, transport measurement can directly probe the chiral edge state by observing QAH effect with zero longitudinal resistance and the quantized Hall conductance $\pm \frac{e^2}{h}$, in which each surface contributes $\pm \frac{e^2}{2h}$. Quantum spin Hall state in 2D TI highly resembles this observation, while it has two conducting channels of opposite spin and propagating direction, and its Hall conductance is also twice of a quantized value. Its edge state is so-called 'helical edge state' and protected by time-reversal-symmetry. So, the QAH effect can be seen as half of a quantum spin Hall state.

QAH effect is proposed initially as a quantum Hall (QH) effect without Landau levels[27-28] and became promising to be achieved after the discovery of TI[24, 29-32]. It was first experimentally realized by Chang *et al.*[9] in a 5 nm thick Cr-doped $(Bi_{1-x}Sb_x)_2Te_3$ grown on STO substrate. Two years later, V-doped $(Bi_{1-x}Sb_x)_2Te_3$[14] was demonstrated to be the second material that shows the QAH effect with a much larger coercive field around 1 T. Figure 1.5 displays the experimental observation of QAH effect by electrical transport measurement in these two systems. As we can see, the Hall resistance ρ_{yx} shows quantized resistance $\pm \frac{h}{e^2}$ with its sign depending on the magnetization direction. The longitudinal resistance remains zero except at the coercive field,

where the sample is not yet fully magnetized and the chiral edge state is not established. The quantization still holds when the field is withdrawn, fulfilling the long-chasing dream of reaching QH effect without any external field.

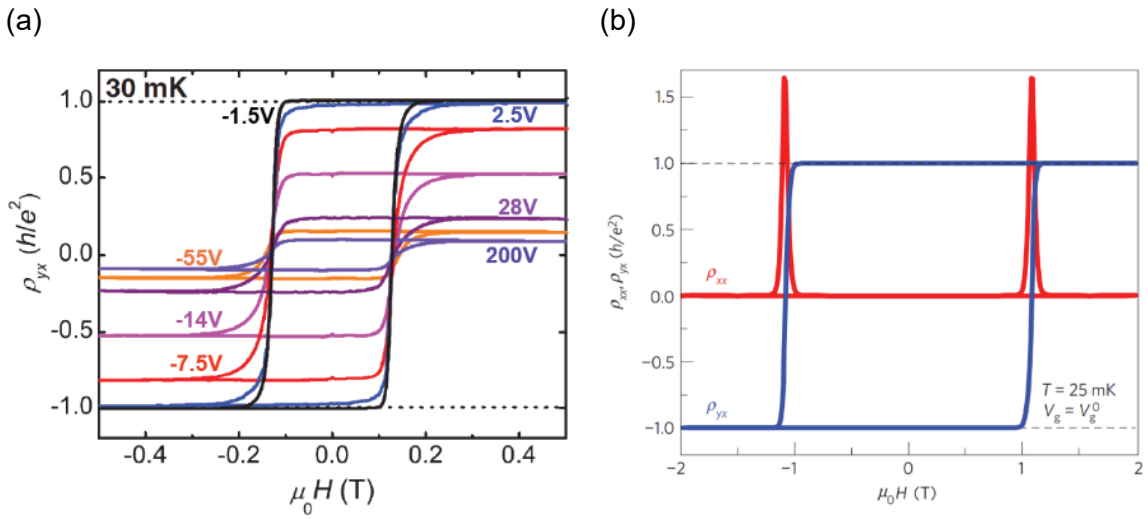

Figure 1.5 Experimental observation of QAH effect by ultra-low temperature electrical transport measurement. (a) Field-dependent Hall resistance ρ_{yx} under varying V_g in Cr-doped $(Bi_{1-x}Sb_x)_2Te_3$. The Fermi surface reaches charge neutral point V_g^0 at V_g = -1.5 V, and the ρ_{yx} becomes $\frac{e^2}{h}$. This figure is reproduced from Chang, C.Z., et al., Science, 2013. **340**(6129). (b) Field-dependent ρ_{xx} and ρ_{yx} at $V_g = V_g^0$ in V-doped $(Bi_{1-x}Sb_x)_2Te_3$. The coercive field increased to 1T. This figure is reproduced from Chang, C.Z., *et al.*, Nature Materials, 2015. **14**(5).

However, the condition of realizing the QAH effect is subtle due to a few reasons: (i) Tuning chemical potential into exchange surface gap by adjusting Bi/Sb ratio requires a tremendous effort. (ii) The magnetic dopants could introduce defects, resulting in unwanted conductive bulk bands and jeopardize the topological order, but the insufficient amount would also harm long-range ferromagnetic order. The balance between sample quality and magnetic order is exceptionally subtle. (iii) Size of the exchange surface gap is small, so the ultra-low temperature (< 100 mK) is a must to minimize the thermal excitation to probe the chiral edge state. Recently,

a lot of discoveries have been making during the attempts to address these challenges. Mogi *et al.* found the modulation magnetic doping[16] of Cr in a penta-layer $(Bi_{1-x}Sb_x)_2Te_3$ structure increased QAH effect temperature to 0.5 K with the residual resistance of 0.017 $\frac{h}{e^2}$, and Ou *et al.* further increased the observation temperature to 1.5 K by Cr/V codoping method[17]. The $MnBi_2Te_4$-family materials have also been discovered as intrinsic magnetic TIs[33-34] to avoid the disadvantage of magnetic doping[15].

In this dissertation, we grew high-quality magnetic-doped/non-doped TIs and stacked them into different heterostructures. The interplay of non-trivial topological properties between different layers gives rise to exotic quantum phenomena. We successfully characterized them using ultra-low temperature transport measurement.

Chapter 2

Experimental Procedure

2.1 Sample Growth

2.1.1 Substrate Preparation

$SrTiO_3$ (STO) is widely used as substrates due to its atomic-flat surface and low-lattice mismatch with various materials. In our experiments, STO (111) substrate with a clean and flat surface is crucial for TI growth. It was first rinsed by ethanol to remove the organic contaminations. Then it was soaked in deionized water at 90 °C for 1.5 hours to increase the chance of selecting Ti-related layer as termination layer[35]. After annealing at 985 °C for 3 hours in a tube furnace with flowing pure oxygen gas, most of the surface carbon and other organic contamination would be removed. Finally, it was outgassed at 550 °C for 1 hour prior to growth in an ultra-high vacuum chamber. A clear reconstruction of its surface can be observed by reflection high-energy electron diffraction (will be introduced in Sec. 2.2), indicating an atomic-flat surface for high-quality TI growth.

Un-doped STO is a good insulator with high dielectric constant[36] (ε) under low temperature ($\varepsilon \sim 20000$ at 4.2 K). It is particularly useful in the transport measurement of TI. A considerable number of carriers is accumulated on the STO/TI interface and lift the chemical potential of TI when a voltage difference is maintained between STO's bottom and the sample. When practicing the electrostatic gating technique, a layer of soft indium is applied on the bottom of STO in order to acquire a uniform electric field coverage over the whole area of the substrate.

2.1.2 Molecular Beam Epitaxy (MBE) Growth

Molecular beam epitaxy (MBE) is used for growing high-quality TI due to the following advantages: (i) The main chamber is required to reach ultra-high vacuum (~ 10^{-10} mbar), and the epitaxy growth is almost free from contamination. (ii) The growth rate is extremely slow (~ 10 nm/hr), so the thickness of the film can be precisely controlled. (iii) Minimum interaction between beams due to the long mean-free-path in the MBE chamber. With stable beam fluxes and sample surface temperature, reproducibility is guaranteed. (iv) MBE growth is a non-thermal equilibrium process. It enables the sample to acquire the structure and phase with elevated energy states or a higher doping level. The TI samples studied in this dissertation are grown by the collaborators in Nitin Samarth's group.

The schematic of an MBE chamber is shown in Figure 2.1. The key components in the system are listed as follows: (i) An ultra-high vacuum main chamber and load lock chamber pumped by turbopumps. Liquid nitrogen was circulated in the cryopanels to improve the background pressure. (ii) Sample holder with a radiant heater and a rotary stage. (iii) Knudsen effusion cell for high vapor pressure material and e-gun for high melting point material. (iv) A 20 keV RHEED gun and a kSA400 RHEED analyzer.

Our TI growth is carried out under the vacuum better than 2×10^{-10} mbar, and the substrate temperature is maintained at ~ 240 °C. Bi (99.999%), Sb (99.9999%), Te (99.9999%) and Cr (99.999%) are evaporated from Kundsen effusion cell, while V (99.995%) is doped by using e-gun. The flux ratio of Te/(Bi + Sb) is usually kept > 10 to minimize Te deficiency, and Bi/Sb ratio is optimized to tune the chemical potential into the charge neutral point. The flux of each element is adjusted by raising / lowering their effusion cell temperatures or e-gun power. The growth is ~ 0.25 QL/min. The typical growth parameters are listed in table 2.1.

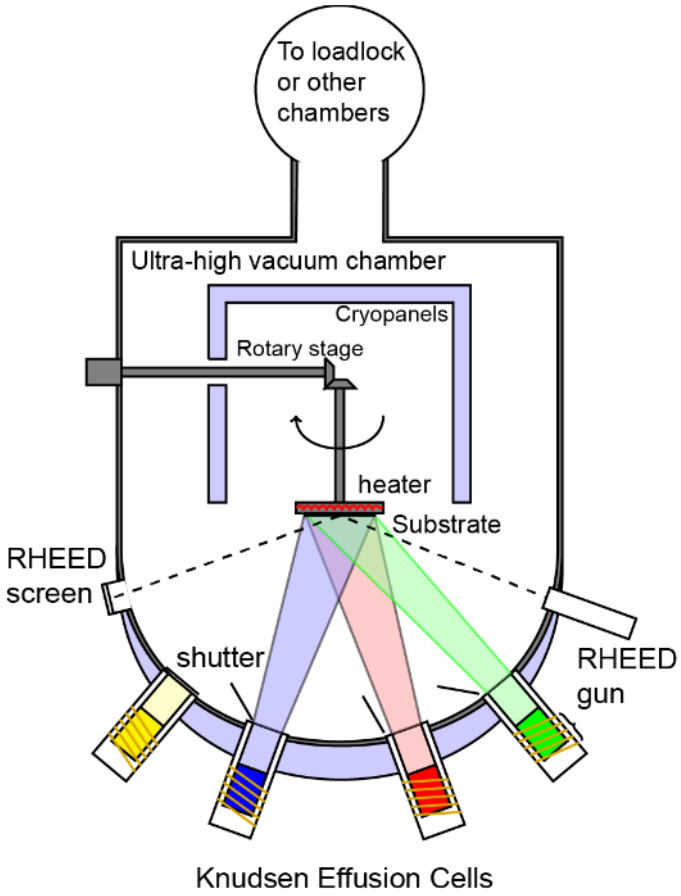

Figure 2.1 The schematic of the MBE system. MBE growth is carried out in an ultra-high vacuum chamber at the pressure < 2×10^{-10} mbar. The substrate is mounted on a rotary stage with and heated by a radiant heater. Knudsen effusion cells are used for evaporating Bi, Sb, Te, Cr sources, and e-gun is used for depositing V. RHEED system is used for *in situ* monitoring of the crystal quality during the growth.

Growth condition / TI type	Bi (°C)	Sb (°C)	Te (°C)	Cr (°C)	V (W)	Substrate (°C)
$(Bi_{1-x}Sb_x)_2Te_3$	491	408	300	N/A	N/A	315
Cr-$(Bi_{1-x}Sb_x)_2Te_3$	500	420	306	1130	N/A	315
V-$(Bi_{1-x}Sb_x)_2Te_3$	490	420	306	N/A	62	315

Table 2.1 The typical growth condition of doped/non-doped TI layers. Bi, Sb, Te, and Cr are evaporated from Kundsen effusion cell, and the table shows their typical temperatures during the growth process. The power of e-gun used for depositing V is also shown above. The temperature can be slightly adjusted (up to ±20 °C) to increase/decrease the sources' flux to tune the chemical potential of the sample into charge neutral point.

After the growth, the sample is annealed at 240 °C for 30 minutes to heal the crystal defects. Before the removal of the sample from the main chamber, a 10 nm thick Te layer is deposited at ambient temperature on top of the magnetic TI heterostructure to slow down the sample degradation. Te capping layer is insulating (> 100 MΩ) at low temperature[37], which is a few magnitudes higher than our heterostructure and have the negligible influence on the transport measurement.

2.1.3 Reflection High-energy Electron Diffraction (RHEED)

Reflection high-energy electron diffraction (RHEED) is an *in situ* surface characterization method that requires a high vacuum environment to prevent the backscattering and a clean incident surface to ensure effective diffraction. These requirements are also fulfilled in MBE growth so it is commonly integrated with the MBE system. In a RHEED measurement, the high energy (10 ~ 30 keV) electrons are collimated by RHEED gun and irradiated to the sample surface with an angle θ smaller than 3°, then they interact with the sample surface and yield a diffraction pattern on top of the RHEED screen.

The sample quality of the MBE growth can be indicated by the RHEED pattern: (i) A layered structure with single-crystalline surface gives a RHEED pattern of sharp parallel streaks, as shown in Fig.2.2a. The streak broadens if there are small domains smaller than the electron coherence length, and the distance between streaks depends on the azimuth angle. (ii) Rough surface caused by 3D islands will form a transmission diffraction pattern of a dot array, which is identical to the diffraction pattern of a 3D crystal. (iii) Sample with disordered crystal structures would not display a well-defined RHEED pattern. Proper reconstruction of substrate STO surface can also be told by the formation of Kikuchi lines that connect the sharp diffraction points on a RHEED pattern, as shown in Fig. 2.2b.

(a) (b)

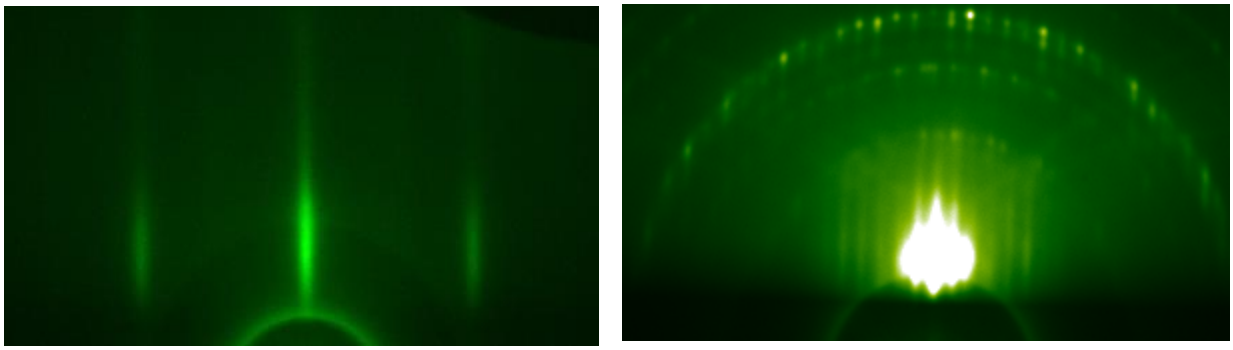

Figure 2.2 RHEED pattern taken from sample growth. (a) A typical RHEED pattern of $(Bi_{1-x}Sb_x)_2Te_3$ layer with the atomically flat crystalline surface. (b) A typical RHEED pattern of STO substrate prior to the growth. Kikuchi lines indicate a good reconstructed surface.

2.2 Sample Characterization Methods

The small exchange gap size in a magnetic doped TI makes the observation of quantized value in transport measurement only possible with the minimum thermal fluctuation (T< 200 mK). Besides, the growth condition of the sample that displays ideal quantization is so subtle that hundreds of attempts have to be made before acquiring the optimal growth parameters. Thanks to the thorough study of TI electric band structure, we can analyze the sample quality by a brief electrical characterization and make a little progress each time.

The growth of magnetic TI heterostructures studied in this dissertation is more complicated. In these samples, not only the chemical potential has to be tuned to the charge neutral point of every TI layer, but the magnetic doping level of a different layer need to be balanced to obtain the target phenomenon. However, samples with the potential of displaying novel quantum phenomenon under ultra-low temperature will show preliminary signs in the measurement at a higher temperature accessible to the physical property measurement system. So, in order to

increase the success rate, we can screen out inferior samples by using the following transport characterization methods prior to the ultra-low temperature measurement.

2.2.1 Physical Property Measurement System (PPMS)

Physical property measurement system (PPMS) is a commercial automated low-temperature (down to 1.9 K) electrical transport measurement system with an integrated 7 T superconducting magnet from Quantum Design (QD), Inc[38]. It includes a storage dewar with liquid ^{4}He reservoir, a PPMS probe with the sample space and a programmable controller (M6000) with DC transport measurement system for data acquisition (Fig. 2.3a).

The PPMS probe along with the superconducting magnet is submerged in the liquid ^{4}He bath (Fig. 2.3c) and its sample space is cooled by pulling the liquid ^{4}He through a dual impedance system via cooling annulus (Fig. 2.3e). Our sample is mounted on the mounting stage (puck) provided by QD that can be fitted to the bottom of the sample space. A circuit board is installed below the sample space and soldered to the feedthrough that makes the electrical contacts with heaters, thermometers, and the puck. It is linked with probe head through the long wires tapped on the outside wall of the sample space.

Figure. 2.3b shows the block diagram of electrical connections when conducting the transport measurements. The device under test (DUT) is wired to the sample puck and matched to individual BNC ports on the contact switcher, so the resistivity measurement system integrated in M6000 can practice 4-probe transport measurement from any electrode of the sample. M6000 conducts the transport measurement and sends acquired data to a computer via GPIB cable. The measurement sequence is programmed by the software *Multivu*.

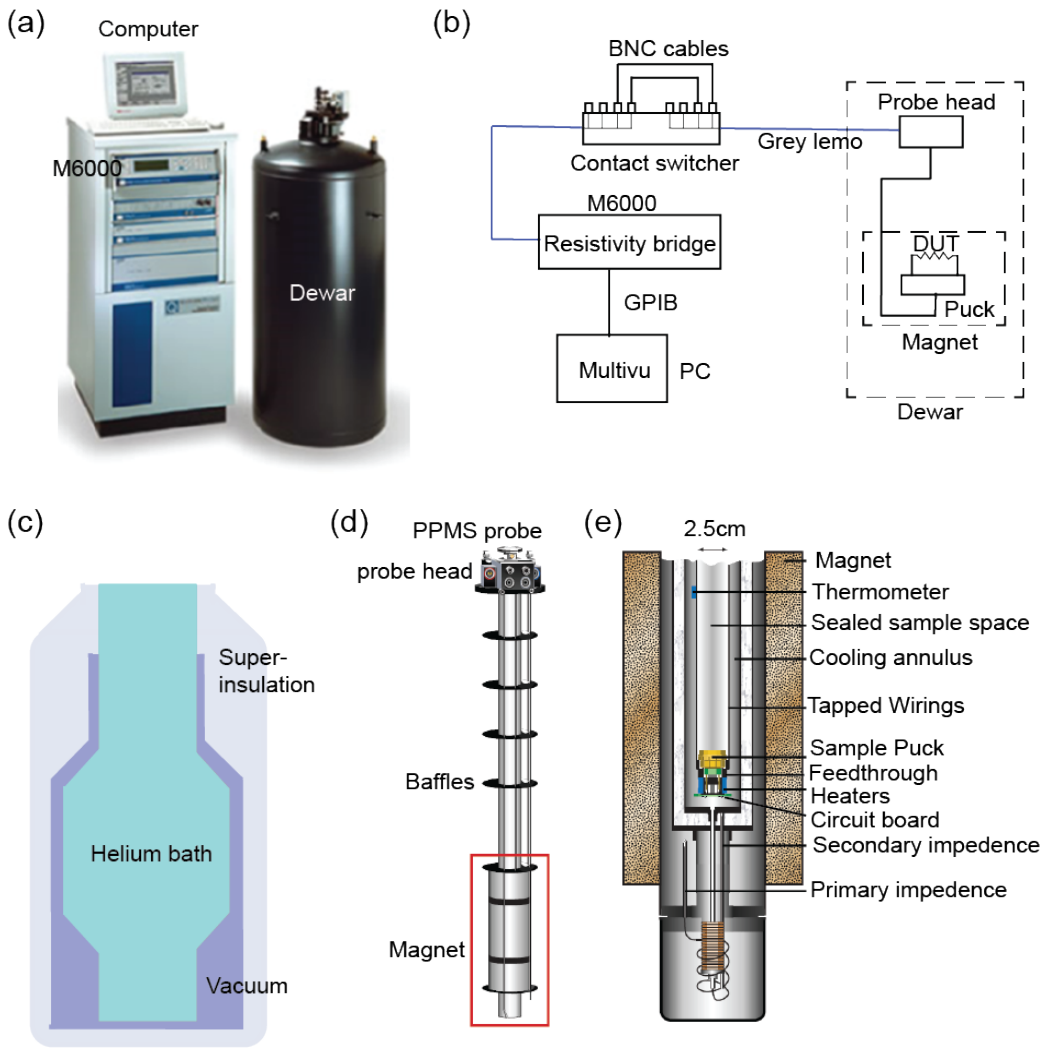

Figure 2.3 Physical property measurement system (PPMS). (a) Storage dewar and M6000 controller. (b) Block diagram of electrical connection. (c) Schematic of the storage dewar. (d) Schematic of the PPMS probe. It is submerged in the liquid ^{4}He bath. (e) Schematic of the cooling system and sample space. Figure (a), (d), and (e) are reproduced from Quantum Design website https://www.qdusa.com/.

2.2.2 Sample Configuration

Before the transport characterization, every magnetic TI heterostructure film is scratched into the same Hall bar geometry with an effective area of 1 × 0.5 mm^2 by a computer-controlled probe station. Then the soft indium metal is squeezed on the back of STO substrate to cover the whole area of Hall bar (in Fig. 2.4a, indium layer with silver-white color is shown in TI removed

area). The gating voltage is applied by connecting the indium layer to the potential HIGH of the source meter Keithley 2400, while the potential LOW is wired to the current drain electrode of the Hall bar (Fig. 2.4b). A 0.1 mm thick sapphire slide is glued (by GE varnish, aka, VGE7031) between the substrate and sample puck in order to insulate gating wire with the puck (made of copper) while keeping a good thermal contact.

When mechanically compressing an indium dot on the surface of the sample, indium penetrates through the Te capping layer and directly touches the TI. Gold wire is used to link the indium dot to the contact pins on the sample puck. An excitation of 1 μA is usually used at 1.9 K, and 1 nA is used at an ultra-low temperature to reduce the thermal fluctuation. Hall resistance ρ_{yx} and longitudinal resistance ρ_{xx} are measured simultaneously.

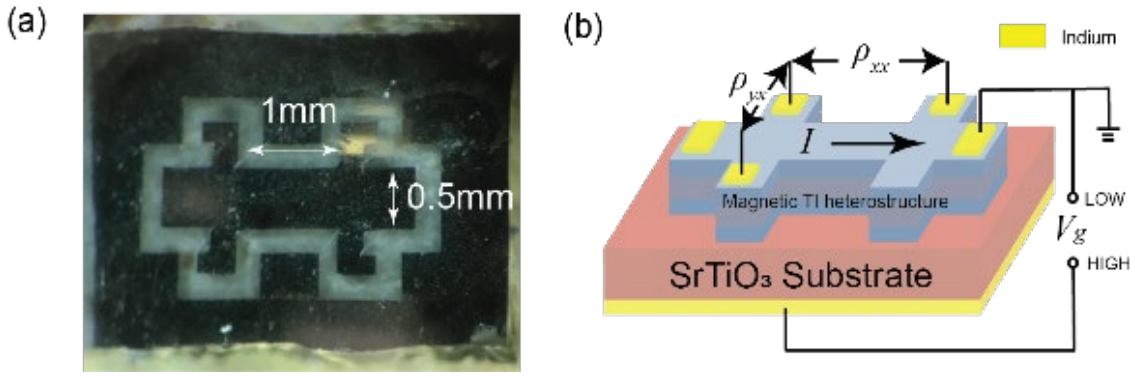

Figure 2.4 Sample configuration in the transport measurement. (a) Photo of a typical sample with Hall bar geometry. (b) Schematic of the sample configuration. It shows the current flow direction, ρ_{yx} & ρ_{xx} leads, and gating voltage V_g.

2.2.3 Hall Resistance

In a ferromagnetic material, the Hall resistance ρ_{yx} is expressed as:

$$\rho_{yx} = \rho_{yx}^{NH} + \rho_{yx}^{AH} + \rho_{yx}^{TH},$$

where ρ_{yx}^{NH} stands for normal Hall resistance, ρ_{yx}^{AH} is the anomalous Hall effect contribution, and ρ_{yx}^{TH} is an optional topological Hall component, which is observed in magnetic TI heterostructure that and be discussed in Chapter 4.

ρ_{yx}^{NH} is caused by the Lorentz force that deflects charge carriers' propagation direction, and it is proportional to the external field, $\rho_{yx}^{NH} = \mu_0 R_H H$. The sign of the Hall coefficient R_H reflects the carrier type, so the growth parameter can be adjusted accordingly. Specifically, we will increase the temperature of Sb by a few degrees Celsius to balance out the excessive n-type carrier in the case of a negative R_H, while we will raise the temperature for Bi with a positive R_H. Empirically, the optimal growth condition will give rise to an almost flat normal Hall resistance when $-10V < V_g < +10V$, and the sign of R_H is tunable within the range of the source meter.

ρ_{yx}^{AH} is the anomalous Hall (AH) resistance normally relating the magnetization M of the sample, $\rho_{yx}^{AH} = R_A M$. In our magnetically doped TI heterostructures, the coercive field is decided by the transition of ρ_{yx}^{AH}. The optimal growth parameters enable the magnetic TI to have a reasonable coercive field (0.1 T for Cr-doped TI; 1 T for V-doped TI) and a Hall angle ($\rho_{yx}/\rho_{xx}^{H=0T}$) > 1 at 2 K. Insufficient magnetic dopants will significantly reduce the coercive field and broaden the transition area of magnetization flipping.

Since the Hall effect produces the voltage difference transverse to the current flow, the Hall resistance is measured from the Hall electrodes perpendicular to the current leads. However, the voltage drop measured by Hall electrodes is impossible to be aligned perfectly perpendicular to the current direction, so it inevitably picks up a longitudinal component. Otherwise, ρ_{yx} of a magnetic TI layer would be strictly zero before applying any external field in the ideal sample with perfect Hall geometry. Measured ρ_{xx} also has a Hall 'pick-up' component by the same reason. A

'symmetrization' method is practiced after the data acquisition to eliminate the influence of such pick-up resistance. The principle of this method is described as follows.

We use $\rho_{yx}(H)$ to denote the measured Hall resistance at H in one half of the Hall loop (field sweeps from $+H$ to $-H$), while $\rho^{0}_{yx}(H)$ is the actual value. $\rho_{yx}(-H)$ denotes the Hall resistance at -H in the other half of Hall loop where field sweeps from $-H$ to H. Then we have,

$$\rho_{yx}(H)= \rho_{yx}^{0}(H) + \alpha\, \rho_{xx}^{0}(H),\ \rho_{yx}(-H) = \rho_{yx}^{0}(-H) + \alpha\, \rho_{xx}^{0}(-H),$$

$$\rho_{xx}(H)= \rho_{xx}^{0}(H) + \alpha\, \rho_{yx}^{0}(H),\ \rho_{xx}(-H) = \rho_{xx}^{0}(-H) + \alpha\, \rho_{yx}^{0}(-H),$$

where α is the pick-up coefficient. Since the actual Hall loop is anti-symmetric and the actual magnetoresistance is symmetric, we have $\rho_{yx}^{0}(-H) = -\rho_{yx}^{0}(H)$, and $\rho_{xx}(-H) = \rho_{xx}^{0}(H)$. Solving for $\rho_{yx}^{0}(H)$ and $\rho_{xx}^{0}(H)$ we will have $\rho_{yx}^{0}(H) = (\rho_{yx}(H) - \rho_{yx}(-H))/2 = -\rho_{yx}^{0}(-H)$ and $\rho_{xx}^{0}(H)=(\rho_{xx}(H)+\rho_{xx}(-H))/2 = \rho_{yx}^{0}(-H)$.

For most of the cases, the pick-up resistance is negligible, especially at the QAH state with non-dissipative edge state. However, the symmetrization process is indispensable when ρ_{xx} is more than one order of the magnitude larger than ρ_{yx} (e.g. the axion insulator state).

2.2.4 Arrott Plot

The Curie temperature (T_c) is another reference for the quality of magnetically doped TI. Cr-doped TI that displays QAH has T_c around 20 K, and T_c for V-doped TI is around 60K. Unusually low T_c indicates the lack of long-range ferromagnetic order in TI.

T_c can be experimentally determined by magnetization measurement (using a Superconducting QUantum Interference Device (SQUID) based Magnetic Property Measurement System from QD) or the transport measurement of AH effect. However, the STO substrate used in

our experiment has background magnetization signal comparable to the signal of magnetic dopants, making the T_c hard to decide with SQUID magnetometer. The emergence of AH effect is a reasonable criterion for the ferromagnetic order, although the hysteresis loop and the anomalous Hall magnitude sometimes became too small to distinguish at a higher temperature.

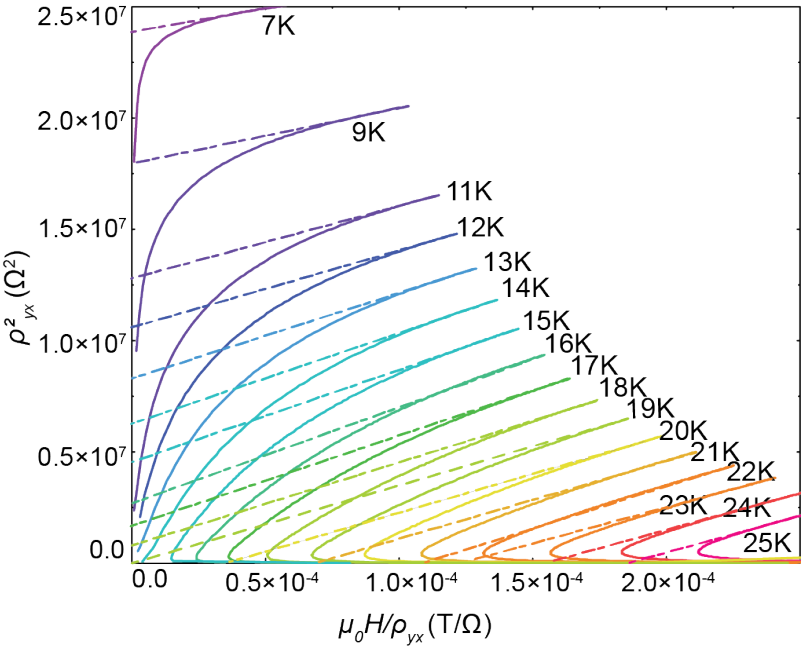

Figure 2.5 Arrott plot of a Cr-doped TI (3QL)/non-doped (5QL)/Cr-doped TI (3 QL) heterostructure. The T_c of this sample is around 19 K.

Arrott plot is another method to determine T_c using transport data[39]. The Arrott plot is expressed as $\rho^2_{yx} = a + b\ \mu_0 H/\rho_{yx}$, where $a \propto \frac{T-T_c}{T_c}$ and b are material-related constants. With the increasing temperature, a changes sign from positive ($T < T_c$, sample is ferromagnetic) to negative ($T > T_c$, sample is paramagnetic). Therefore, the back-tracing extension line of isothermal ρ^2_{yx} - $\mu_0 H/\rho_{yx}$ curve that pass through the origin is taken at T_c. Figure 2.5 displays the Arrott plot of a Cr-doped TI (3QL)/non-doped (5QL)/Cr-doped TI (3 QL) heterostructure for example. The extension line of the isothermal curve at $T_c = 19$ K has an intercept of zero, the curves above T_c have negative intercept, while those below T_c have positive intercept.

2.2.5 Conductance Conversion

In the electrical transport measurement, the measurable parameters are current, voltage and resistance (or it can be directly calculated from Ohm's law using former parameters). However, conductance is more commonly used in the theoretical description of two-dimensional systems, so the conversion from resistance to conductance is vital to characterize the topological quantum phenomenon. In our topological heterostructure films, resistance and conductance are tensors in nature, and their conversion relations are listed as follows.

$$\rho_{xx} = \frac{\sigma_{xx}}{\sigma_{xx}^2 + \sigma_{yx}^2}, \rho_{yx} = \frac{\sigma_{yx}}{\sigma_{xx}^2 + \sigma_{yx}^2};$$

$$\sigma_{xx} = \frac{\rho_{xx}}{\rho_{xx}^2 + \rho_{yx}^2}, \sigma_{yx} = \frac{\rho_{yx}}{\rho_{xx}^2 + \rho_{yx}^2}.$$

Extra caution should be used in ρ_{yx} and ρ_{xx} around H_c to prevent the artifacts formed by the conductance conversion. Figure 2.6 shows two common artifacts taken place during the magnetization reversal in field-dependent conductance relation of QAH effect. Figure 2.6a and c display perfectly quantized ρ_{yx} and ρ_{xx} in V-doped and Cr-doped TI under 30 mK, respectively. When converted to σ_{yx} , however, Fig. 2.6b shows a 'zero plateau' (boxed by dashed lines) around H_c, while Fig. 2d displays a 'peak' overshooting the quantized conductance. Mathematically, 'zero plateau' is due to the much higher bulk resistance ρ_{xx} ($> 2\frac{h}{e^2}$) than ρ_{yx}($< 0.5\frac{h}{e^2}$) around H_c, and the 'overshoot' happens because ρ_{xx}^2 is negligible when ρ_{yx} is close but still smaller than $\frac{h}{e^2}$. These artifacts have no particular physical meaning and they are unambiguously different from the features of the quantum phenomena in the next two chapters. Merely induced by the method errors in the field scan under ultra-low temperature, these artifacts can be avoided if we set a uniform sampling/field-sweeping rate and take an enough amount of data points.

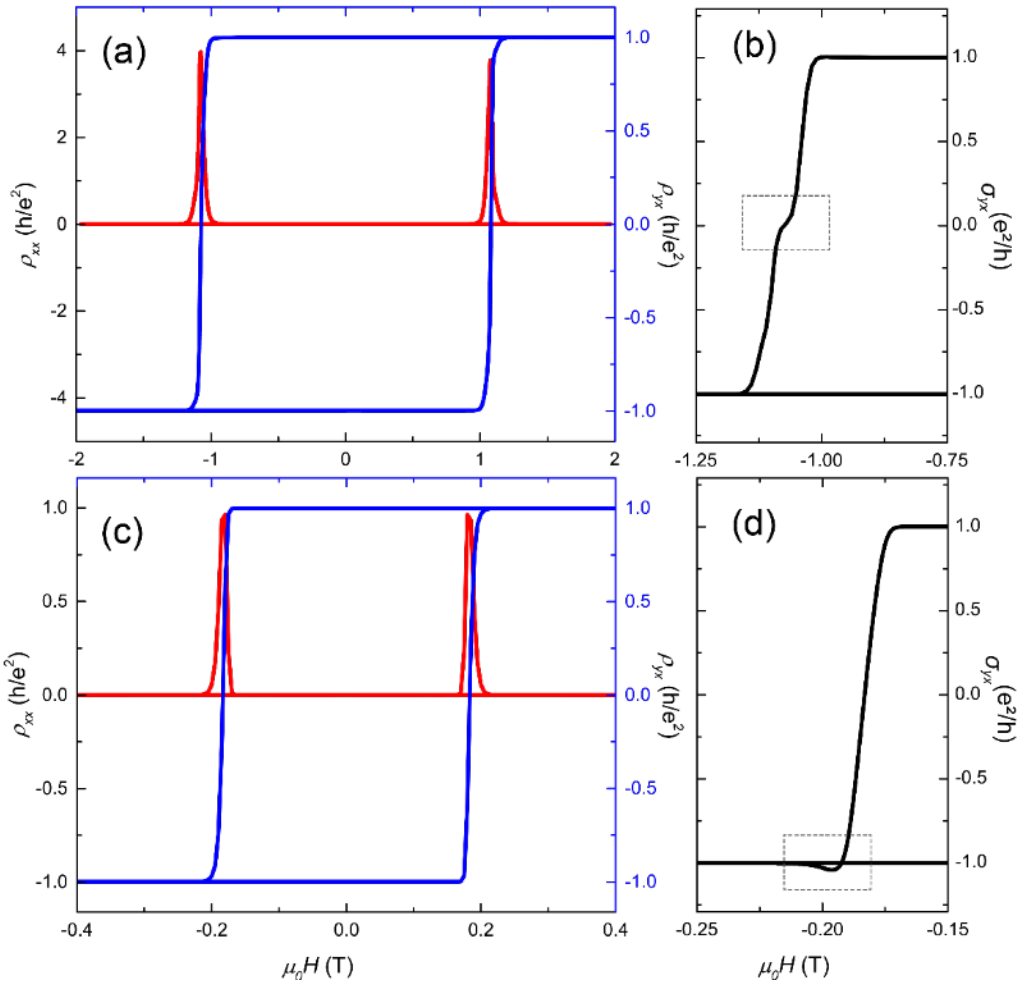

Figure 2.6 Two common artifacts when conducting conductance conversion from resistance. (a) $\mu_0 H$-dependent ρ_{yx} and ρ_{xx} of V-doped TI showing QAH effect. (b) the 'zero plateau' of σ_{yx} around H_c. (c) $\mu_0 H$-dependent ρ_{yx} and ρ_{xx} of Cr-doped TI showing QAH effect. (d) the 'peak' overshoots quantized conductance $\frac{e^2}{h}$.

2.3 Ultra-low Temperature Transport Measurement

When the energy of electron thermal fluctuations (in the order of $k_B T$, where k_B is Boltzmann constant, T is the temperature) is comparable to the small exchange gap size of the magnetic TI in size, the electron would induce excessive conducting channels other than the chiral edge state. In the magnetic TI heterostructure with two magnetic TI layers, their exchange gap

overlap is even smaller. In order to reach the quantized value, the ultra-low temperature is required to minimize the thermal fluctuation.

We use a commercial MiniKelvin 126-TOF series dilution refrigerator (DR) from Leiden Cryogenics[40] to create an ultra-low temperature environment down to 30 mK, and pair it with an AVS-47 resistivity bridge to conduct the electrical transport measurement. Here, we will introduce the working principle and experimental set-up.

2.3.1 Operation Principle of Dilution Refrigerator

The helium storage dewar used for the DR is more thermally conservative than a PPMS dewar shown in the Figure 2.3c: a liquid nitrogen jacket is buffered between the outer vacuum jacket and the ^{4}He bath in order to reduce the heat exchange with the ambient environment. The DR insert is submerged in liquid helium ($T \sim 4.2$ K), and the dilution circuit ($T << 4.2$ K) is sealed (vacuum shield is removed to show components in Fig. 2.7b) at high vacuum in the inner vacuum chamber (IVC) to prevent the heat exchange with ^{4}He bath. Figure 2.7a shows the DR working principle. The mixture of two isotopes of helium, ^{3}He and ^{4}He, is circulating inside this closed-loop dilution circuit.

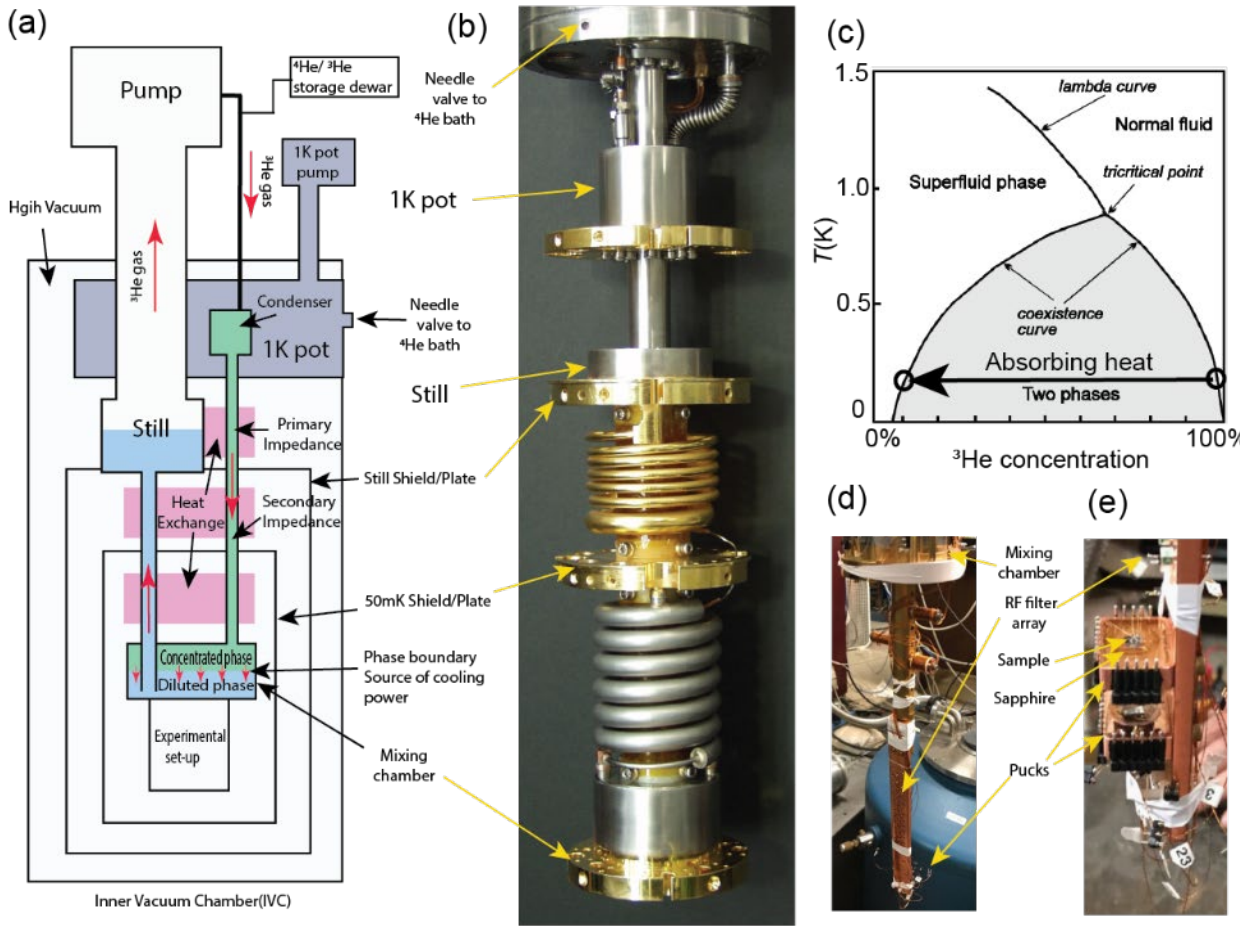

Figure 2.7 Operating principle of a dilution refrigerator. (a) The schematic diagram of a DR insert, the dilution circuit and other key components are labeled. (b) Picture of the DR insert used in our experiment with the shields removed. (c) Phase diagram of ^{3}He/^{4}He mixture[41]. (d) Picture of the experimental set-up of transport measurement, it is attached to the mixing chamber. (e) Picture of the sample puck and the sample.

The 1K pot provides the preliminary cooling power by pumping liquid helium from the ^{4}He bath through the needle valves, and the mixture is also initially liquefied in the 1 K pot (T ~ 1.2 K). When pumping the still using turbo pump, higher-vapor-pressure (compared to ^{4}He under low temperature) ^{3}He would be extracted and lower the still temperature down to 0.6 K. Once the T is below 0.86 K (the tri-critical point in Fig. 2.7c), ^{3}He/^{4}He mixture separates into two phases: the 'lighter' ^{3}He-rich 'concentrated phase' shown in green; and the 'heavier' ^{4}He-rich 'diluted phase' shown in blue[42]. The ^{3}He/^{4}He ratio is carefully chosen (10 - 20 %) so that the phase

boundary is inside the mixing chamber. When ^{3}He in ‘concentrated phase’ enters ‘diluted phase’ through the phase separation surface (shown with the horizontal arrow in Fig. 2.6c) in the mixing chamber, it will absorb heat and gradually bring the chamber down to the ultra-low base temperature. The cooling power of this DR model at 120 mK is designed to be 700 μW, and the base temperature is below 10 mK.

The circulation of ^{3}He enables the system to maintain a dynamic equilibrium. In Fig. 2.7a, ^{3}He flow is labeled in red arrows, and let’s study the circulation starting from the Still. Once the ^{3}He is pumped out of the ‘diluted phase' in the Still (heat can be applied in the still to increase the flow), it enters the ambient environment. Then it is cleaned by liquid nitrogen traps, goes back to the condenser and is liquefied once again by the 1K pot. ^{3}He is further cooled by the heat exchangers (shown in pink) when it passes through the impedances and flows back to the mixing chamber. ^{3}He will always re-enter the ‘diluted phase’ and finish another round of circulation because the pumping of the Still prevents ^{3}He from being saturated.

2.3.2 Sample Space and Superconducting Magnet

The experimental set-up is closely attached to the mixing chamber, shown in Fig. 2.7d, by using a copper rod to maximize the thermal conductance. The samples are prepared in the way described in Section 2.2.2 on a custom-made sample puck (Fig. 2.7e). They are mounted at the far end of the rod to reach the center of the magnet. The wires for the transport measurement are rounded around the rod branches for increasing the heat capacity (or thermal stability). Each wire connects to an individual RF filter before contacting the sample. Since the sample is in direct metallic contact with these contacting wires, the heat of the sample conducted through the wires is comparable to the heat exchanged with the sample puck. A nonlinear thermometer RuO_2, whose

resistance can rise from 400 Ω to 22 kΩ when the temperature changes from 300 K to 10 mK, is used in the mixing chamber.

A solenoid-style superconducting magnet made from winding NbTi wire is installed in the bottom of the ^{4}He bath. The critical field and maximum current density of NbTi enable the magnet to host the magnetic field up to 9 T. The sample space is loaded into the center of the solenoid, where the magnetic field is concentrated and uniform.

During the magnet operation under ultra-low temperature, the magnetization process when applying field introduces heat to the system, resulting in the rise of sample temperature by a few millikelvin. This heating effect is rather pronounced at magnetization direction flipping when the magnet sweeps over zero field. By the same token, the demagnetization process of withdrawing the field decreases the temperature, similar to the adiabatic demagnetization technique used to achieve sub-millikelvin. This millikelvin temperature difference will give non-negligible deviance from actual resistance.

To obtain consistent temperature in field-dependent transport measurement, low field sweeping rate ~ 10 Oe/s is used and the magnetic field is held when taking data. An additional data acquisition delay of a few minutes is also taken after each target field value is achieved and stabilized. A Hall loop up to 1.5 T usually takes hours to finish, so a proper arrangement of the holding fields is vital for balancing data quality and time efficiency. A large field step size is often used in monotonously changing regions (quantized or zero resistance plateau in magnetic TI samples), while a finer but uniform field step size is practiced in feature-rich regions (around H_c). The step size shall be adjusted to avoid possible data artifact. However, in the PPMS measurement, high-quality data can be easily acquired with continuous field-sweeping due to the smaller ratio of temperature fluctuation at 2 K.

2.3.3 AC Resistivity Bridge

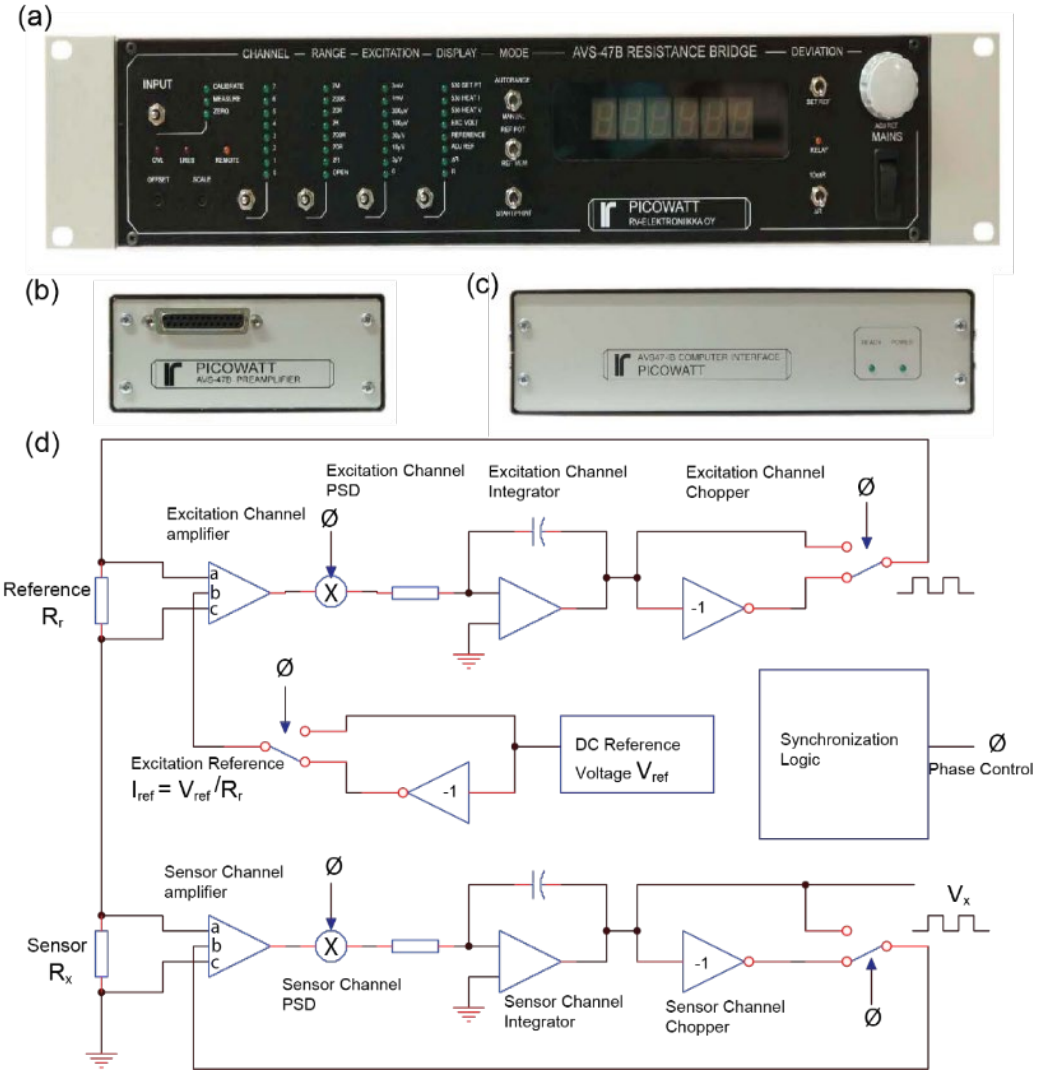

Figure 2.8 AVS-47 AC resistivity bridge. (a) The front panel of AVS-47. The reference resistance R_r and the reference excitation voltage V_{ref} is adjustable. (b) The digital interface for AVS-47. (c) Block diagram that shows the working principle of AVS-47. Figure (a), (b), and (c) are reproduced from AVS-47 manual from http://www.picowatt.fi.

The AVS-47 AC resistivity bridge from Picowatt is used for conducting four-probe transport measurement[43]. It is an analog resistance bridge without any built-in microprocessor. Except for the main unit, it also has a digital interface for GBIP connection and the low-noise pre-amplifier located in two separate units (Fig. 2.8 b & c). The computer interface provides a long

physical distance between AVS-47 and the noisy bus, while the pre-amplifier can decrease the radio frequency noise by minimizing the lead length to the sample. AVS-47 has an 8-channel multiplexer, an adjustable reference resistance R_r ranging from 2 Ω to 2 MΩ and the reference excitation voltage V_{ref} ranging from 3 μV to 3 mV. These parameters can be toggled in the front panel (Fig. 2.8a).

The working principle of AVS-47 is illustrated by the block diagram in Fig. 2.8d. A precision DC reference output first sends out a preset excitation voltage signal V_{ref}, then it is converted to a square wave (frequency is between 10 to 20 Hz) by the chopper and sent to channel 'b' in the excitation channel pre-amplifier. If the difference 'a-c' doesn't correspond to 'b', the pre-amplifier will output a square wave. Then the square wave is rectified but still synchronized to be in-phase with the excitation. The rectified signal is accumulated in an analog integrator, chopped again and superposed on the total output in order to adjust the excitation current. This feedback loop continues until 'a-c' is equal to 'b', which means the voltage drop across R_r is the same as the DC reference output $V_{ref.}$ Since the reference resistor R_r is in series with the sensor (DUT), the current excitation for both is $I_{ref} = 2\,V_{ref}/R_r$.

The second feedback loop measures the voltage drop of the sensor R_x. The sensor channel pre-amplifier will keep outputting a square wave and slewing either up or down the integrator until the V_x (channel 'b') matches the R_x voltage drop ('a - c'). Hence, the resistance R_x is measured as $R_r V_x / V_{ref.}$ AVS-47 provides high-precision measurement under ultra-low temperature due to its special design and practical working principle. In our experiments, AVS-47 is able to characterize quantized Hall resistance up to 0.9991 $\frac{h}{e^2}$ and the resistance of non-dissipative edge channel as low as $2\times10^{-5}\,\frac{h}{e^2}$.

Chapter 3

Realization of the Axion Insulator State

3.1 Topological Magnetoelectric Effect

3.1.1 Basic Concepts

Topological magnetoelectric effect (TME)[24, 44-45] is a unique magnetoelectric effect for topological insulators that an electric field could induce a topological contribution to the bulk magnetization, and in turn, a magnetic field could also induce a quantized electrical polarization. In contrast to the ordinary Maxwell electromagnetic dynamics, the induced magnetic field is co-linear with the electric field, and vice versa. Both of these two magnetoelectric responses,

$$M_t = \frac{\theta}{2\pi}\frac{e^2}{hc}E, \text{and } P_t = \frac{\theta}{2\pi}\frac{e^2}{hc}B.$$

originate from the additional $E \cdot B$ term,

$$S_\theta = \frac{\theta}{2\pi}\frac{e^2}{h}E \cdot B,$$

to the usual Maxwell Lagrangian, in which θ is the dimensionless pseudo-scalar parameter characterizing the topology of an insulator. In an ordinary insulator, θ is 0, while for a TI, θ equals to π. These topological magnetoelectric responses provide a condense matter approach to the axion electro-dynamics from particle physics[46], and a system being able to facilitate such TME effect is termed as an 'axion' insulator[45, 47].

In a magnetic doped TI film that is able to realize the QAH effect, a half-integer quantum Hall effect with spins polarized to the magnetization occurs on both top and bottom surfaces (Sec. 1.3). When the magnetizations of both surfaces are aligned to the same direction, chiral edge

current emerges on the quasi-1D side surfaces, and QAH is observable with a full quantized Hall value $\pm\frac{h}{e^2}$ when the chemical potential is tuned into the magnetic exchange gap (Figure 3.1a). However, when the magnetizations have the anti-parallel alignment, TME effect can be obtained. The two surfaces have a fixed edge Hall conductance $\sigma_H = \frac{e^2}{2h}$, but with opposite directions and form a circulating current on the side surface normal to the electric field E_x (Circulation loop in red of Fig. 3.1b). This circulating current displays TME effect by inducing a magnetic field B_x parallel or anti-parallel to E_x. Similar induction of charge polarization will occur parallel/anti-parallel to the applied magnetic field. In a TI system hosting TME effect, all surfaces, including the side surfaces, should be gapped to eliminate non-topological contribution.

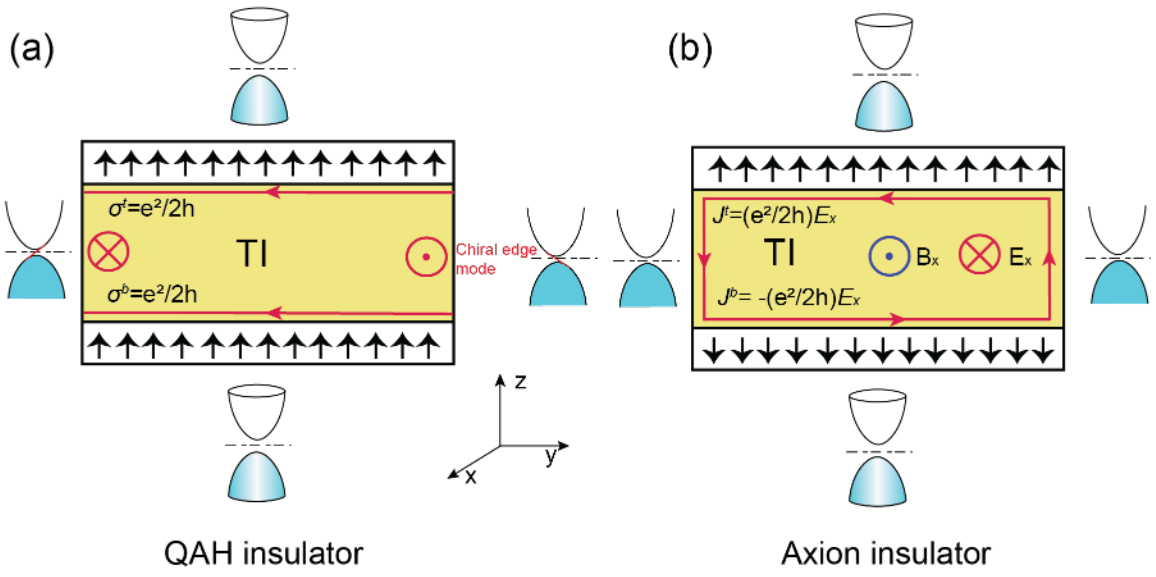

Figure 3.1 Schematics of the QAH insulator and the axion insulator shows TME effect. (a) The realization of the QAH effect in TI with the magnetizations of both top and bottom surfaces aligned to the same direction. (b) Axion insulator state with the magnetization and quantized Hall conductance of two surfaces in opposite directions. With the application of an electric field E_x, it forms a circulating current that gives rise to a magnetic field B_x. This is a unique magnetoelectric effect for topological insulators and termed as the TME effect.

3.1.2 Requirements for Topological Magnetoelectric Effect

In order to realize the TME in the TI system, many proposals[24, 45, 47] have been made and they sum up to the following requirements. (i) The thickness of TI film should be in the 3D regime to minimize the influence of the hybridization between the top and bottom surfaces; (ii) Time reversal symmetry of top and bottom surfaces should be broken in order to gap their 2D Dirac cones, then the chemical potential should be tuned into these gaps to give rise to the half-integer quantum Hall effect on each surface. The side surfaces should also be gapped to satisfy the adiabatic condition for TME effect; (iii) The interior of the TI should maintain the time reversal symmetry in order to keep $\theta = \pi$ in the bulk.

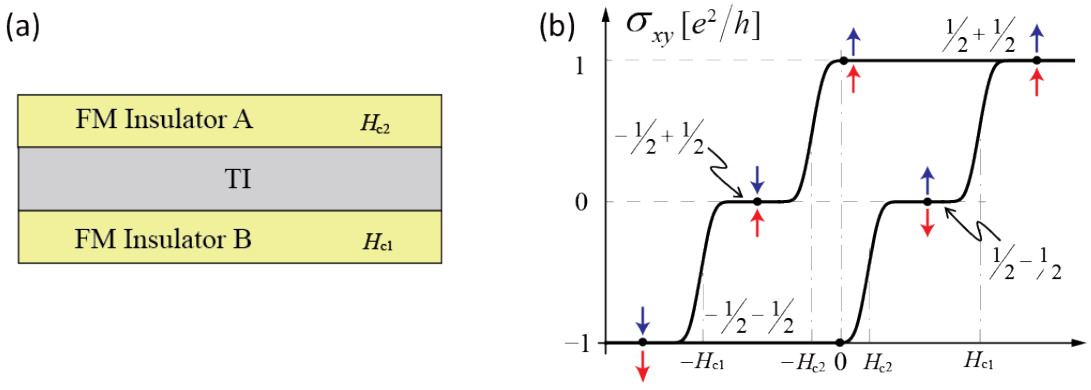

Figure 3.2 Proposed axion insulator structure and its $\mu_0 H$ dependence of σ_{yx}. (a) Schematic of a magnetic / nonmagnetic/magnetic TI sandwich heterostructures for realizing axion insulator state. (b) $\mu_0 H$ dependence of σ_{yx}, the blue and red arrows represent the magnetization alignment of magnetic TI layers. The axion insulator state occurs at $\mu_0 H_{c1} > \mu_0 H > \mu_0 H_{c2}$. It displays zero Hall conductance and anti-parallel magnetization alignment. This figure is reproduced from Wang, J., *et al.*, Physical Review B, **92,** 081107 (2015).

The most commonly proposed experimental structure design for realizing an axion insulator is the magnetic/nonmagnetic/magnetic TI sandwich heterostructure[45], in which the top and bottom magnetic TI layers have two coercive fields, H_{c1} and H_{c2}, shown in Fig. 3.2a. Here we set $H_{c1} > H_{c2}$ and both magnetic TI has an out-of-plane easy axis for simplicity. The axion insulator

state can be achieved as follows: we first align the magnetization of both magnetic layers to one direction by applying $\mu_0 H > \mu_0 H_{c1}$, then we withdraw and increase $\mu_0 H$ to an opposite direction; Once $\mu_0 H_{c1} > \mu_0 H > \mu_0 H_{c2}$, the magnetization of H_{c2} layer is reversed while the 'harder' H_{c1} layer remains the same (shown by the red and green arrows in Fig. 3.2b). Two surfaces thus acquire opposite magnetization alignment, as shown in Fig. 3.1b.

We emphasize that the 'surface' mentioned above is the interface between the entities with different topology, e.i., bottom magnetic TI/STO substrate, top magnetic TI/Te capping, side surface/vacuum. Since the middle non-magnetic TI maintains the same topology of heterostructure throughout three TI layers, the magnetic/non-magnetic TI interface cannot be seen as an additional 'surface' that could host a half-integer quantum Hall effect. In other words, the magnetic/nonmagnetic/magnetic TI sandwich heterostructure is one TI film with adjustable surface magnetization rather than two QAH insulators connected in parallel.

In the ultra-low temperature transport measurement using a typical Hall bar configuration (introduced in Fig. 3.2), when the TI sandwich heterostructure is showing the QAH effect, the only conducting channel is the chiral edge state where the backscattering is prohibited. The σ_{xx}, as well as ρ_{xx}, thus vanishes. While at the axion insulator state, any excitation current sent into the sample will be totally reflected by the counter-propagating half-quantized edge channels, so the $\rho_{xx} = \infty$ and $\sigma_{xx} = 0$. The ρ_{yx} and σ_{yx} should all reduce to 0 because the lack of conducting electrons blocks the Hall response. Figure 3.2b shows the $\mu_0 H$ dependence of σ_{yx} in such TI sandwich heterostructure displaying a 'zero-plateau' feature on top of QAH hysteresis loop.

3.1.3 Previous Experiments

Early studies discovered 'axion electrodynamics' features in uniformly Cr-doped TI[48-49] or V-doped TI[50], although these observations didn't serve as solid evidence of the axion insulating state. In Cr-doped $(Bi_{1-x}Sb_x)_2Te_3$, a 'zero-plateau' feature in $\mu_0 H$ - σ_{yx} relation[45, 48-49] was observed during the magnetization reversal (Fig. 3.3a), and the corresponding ρ_{xx} was up to a few megaohms (Fig. 3.3b). However, as shown in Fig. 3.3c, the insulating behavior of ρ_{xx} is more likely due to the formation of multi-domain and the chiral edge states at the domain walls[20, 48] rather than the counter-propagating edge state between the top and bottom surface. Since the conduction σ_{yx} is converted from $\frac{\rho_{yx}}{\rho_{xx}^2+\rho_{yx}^2}$, its 'zero-plateau' is due to the large ρ_{xx} (See Sec. 2.2.5 for further discussion). In V-doped $(Bi_{1-x}Sb_x)_2Te_3$[50], a scaling behavior, which has two semi-circles (the dark gray curve in Fig. 3.3d) centered at (σ_{xx} , σ_{yx}) = ($\frac{e^2}{2h}$, 0) and (- $\frac{e^2}{2h}$, 0), connecting ($\frac{e^2}{h}$, 0), (- $\frac{e^2}{h}$, 0), and (0, 0), represents two independent integer quantum Hall effect observed at thickness d = 6nm[50]. It developed to one semi-circles (green dots in Fig. 3.3d) centered at (0, 0), connecting ($\frac{e^2}{h}$, 0), (- $\frac{e^2}{h}$, 0) when d = 9 nm, which represents the QAH effect. The authors believe that the QAH effect observed in 3D TI can be regarded as an 'axion insulator'. This observation, again, cannot guarantee the credibility of zero σ_{yx} as it was converted from ρ_{xx} and ρ_{yx}. Also, the chiral edge state at 3D regime makes the side surfaces gapless and contradicts the requirement (ii) for TME effect. Generally speaking, a uniformly doped TI film is unlikely to host the axion insulator state because the time reversal symmetry of its interior is broken by the magnetic dopants, and the strong exchange coupling between the top and bottom surfaces makes it impossible for it to have opposite magnetization directions.

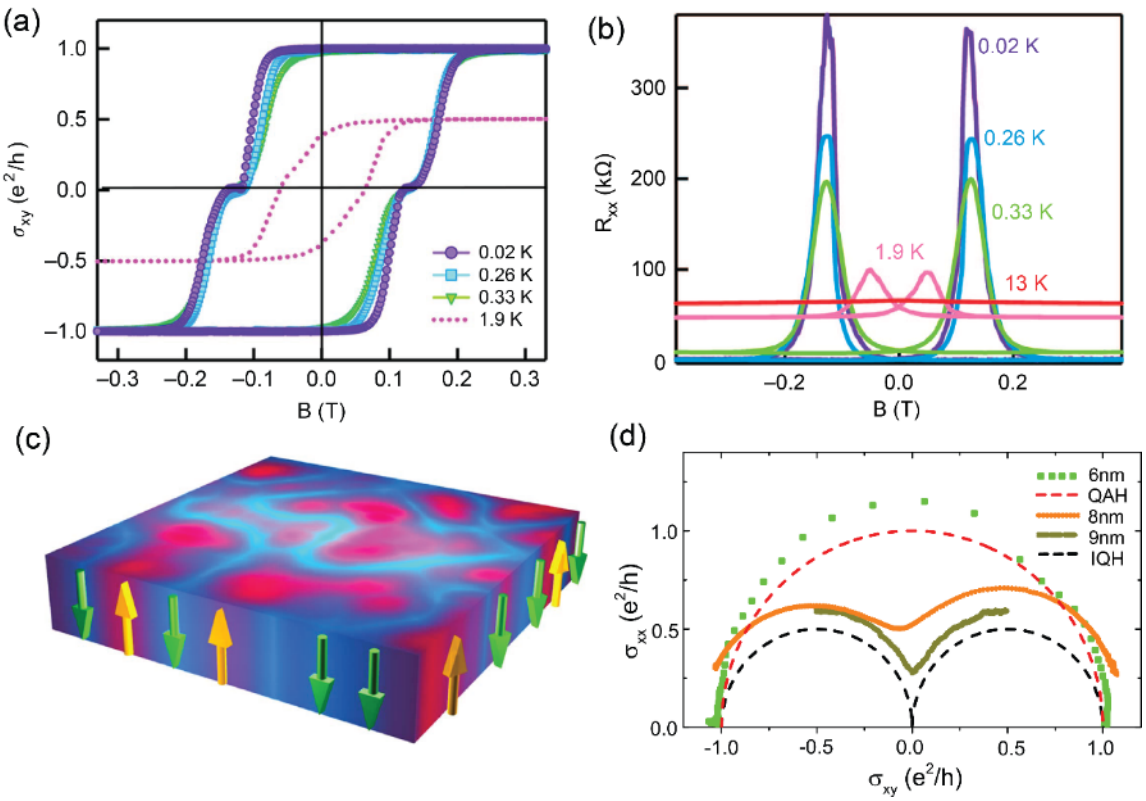

Figure 3.3 'Zero-plateau' feature in uniformly doped TI. (a) $\mu_0 H$ dependence of σ_{yx} in Cr-doped $(Bi_{1-x}Sb_x)_2Te_3$ at different temperatures. σ_{yx} is quantized when the sample is magnetized and a 'zero-plateau' feature appears during the magnetization reversal. (b) $\mu_0 H$ dependence of ρ_{xx} at different temperatures. Huge peaks with resistance up to a few megaohms appear around H_c. (c) Schematic of samples' magnetization with randomly-formed multi-domains. Orange arrows and red color region represent upward magnetization while green arrows and blue color region represent the opposite direction. (d) Flow diagram of (σ_{xx}, σ_{yx}) of V-doped $(Bi_{1-x}Sb_x)_2Te_3$ films with thickness d = 6 nm (green), 8 nm (orange), 9 nm (gray). The two dashed black semi-circles represent the scaling behavior of integer quantum Hall effect, while the red dashed semi-circle represents the QAH state. Figure (a - c) are reproduced from Kou, X., *et al*., Nature Communications, **6**, 8474 (2015); Figure (d) is reproduced from Grauer, S., *et al.,* Physical Review Letters, **118**, 246801 (2017).

Another study[51] fabricated Cr-doped/non-doped/Cr-doped TI heterostructure with different H_c between two magnetic layers caused by the structural asymmetry. At 40 mK, it also acquired 'zero-plateau' in σ_{yx} and two Cr-doped TI can potentially possess opposite magnetization

alignment. However, subsequent nanoSQUID-on-tip magnetic imaging studies[52] failed to confirm the antiparallel magnetization.

We noticed that important evidence of 'axion electrodynamics', the 'zero-plateau' in $\mu_0 H$-ρ_{yx} relation, was absent in all previous studies, even with Cr-doped/non-doped/Cr-doped TI heterostructure. So, it's natural for us to suspect that in that study, the H_c difference of two Cr-doped TI surfaces was so small that the higher H_c layer already started the domain nucleation before the lower H_c layer's magnetization was entirely reversed. This speculation motivates us to look for two magnetic materials that have much bigger H_c difference to realize the axion insulator state.

3.2 Realization of the Axion Insulator State in TI Heterostructures

3.2.1 Sample Configuration and Structural Characterization

We follow the proposed magnetic/nonmagnetic/magnetic TI sandwich heterostructure but use different magnetic dopants in the top and bottom TI layer to increase the H_c discrepancy. So, our design for the axion insulator is 3 QL V-doped $(Bi_{1-x}Sb_x)_2Te_3$/4-6 QL $(Bi_{1-x}Sb_x)_2Te_3$/3 QL Cr-doped $(Bi_{1-x}Sb_x)_2Te_3$ (Fig. 3.4a), here we refer them as 3-4-3, 3-5-3, and 3-6-3 heterostructure. The V-doped TI and Cr-doped TI are the best candidates since they have large H_c difference (at 30 mK, H_c = 1 T for V[14] and 0.15 T for Cr[9], as shown in Fig. 3.4b) and prior observations of QAH effect.

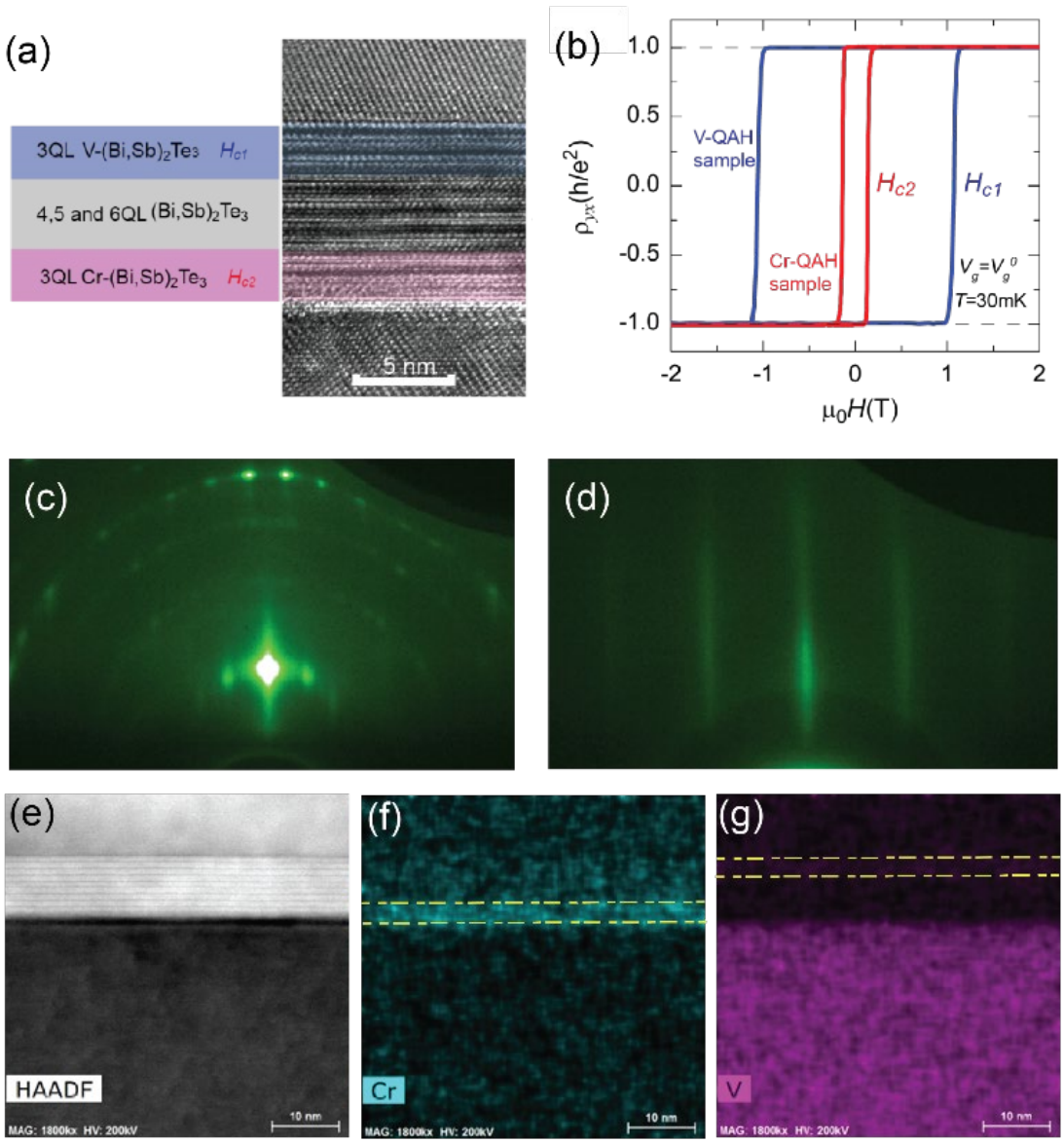

Figure 3.4 Structural characterization of 3QL V-doped $(Bi_{1-x}Sb_x)_2Te_3$ / 4-6QL $(Bi_{1-x}Sb_x)_2Te_3$ / 3QL Cr-doped $(Bi_{1-x}Sb_x)_2Te_3$ sandwich heterostructure. (a) The schematic of the sample configuration and its cross-sectional HR-TEM image. The V-doped TI layer is labeled by blue color, while the Cr-doped layer is labeled by red color. (b) QAH effect of uniformly V-doped TI (blue curve), and Cr-doped TI (red curve) at 30 mK. H_c of V[14] is 1 T and that of Cr[9] is 0.15 T. (c - d) RHEED pattern of heat-treated STO substrate before growth and the 3-6-3 heterostructure after the growth. (e) The cross-sectional HAADF-STEM image of 3-4-3 heterostructure and the EDS mapping of Cr and V element.

We keep our magnetic layer thickness as 3 QL to maintain the long-range ferromagnetic order and avoid the possible influence of the bulk carrier. Undoped middle $(Bi_{1-x}Sb_x)_2Te_3$ layer serves two important proposes: (i) Maintaining the interior's time-reversal symmetry for reaching the requirement (iii) of TME effect ($\theta = \pi$ in the bulk); (ii) Decoupling two magnetic layers for realizing the anti-parallel alignment. To fulfill the requirement (ii) for the TME effect (all surfaces gapped), we first optimized growth condition for each TI layer by tuning the chemical potential to the charge neutral point. Then we systematically change the thickness of middle layer from 4 QL to 6 QL in order to find the appropriate thickness that minimizes the exchanging coupling between two magnetic layers, while still gaps the side surfaces via quantum confinement.

The RHEED pattern in Fig. 3.4c shows dot array in concentric circles, indicating the atomically flat surface of heat-treated STO (111) substrate. The sharp and streaking '1×1' pattern observed after the growth of 3-6-3 heterostructure in Fig. 3.4d also demonstrates its highly-ordered crystal structure.

Figure 3.4a and Fig. 3.4e respectively shows the cross-sectional of high-resolution transmission electron microscopy (HR-TEM) and high-angle annular dark-field scanning transmission electron microscope image (HAADF-STEM) of the 3-4-3 heterostructure. The crystal structures of Te capping layer, the 10 QL heterostructure, and the STO substrate can be distinguished. The Energy-dispersive X-ray spectroscopy (EDS) measurements (Fig. 3.4f and g) shows weak but distinguishable signals in Cr-/V- doped layer (highlighted with yellow dashed lines). It reflects the doping (~ 5 %) levels of these ions in our 3-4-3 heterostructure.

3.2.2 Transport Characterization at 2K

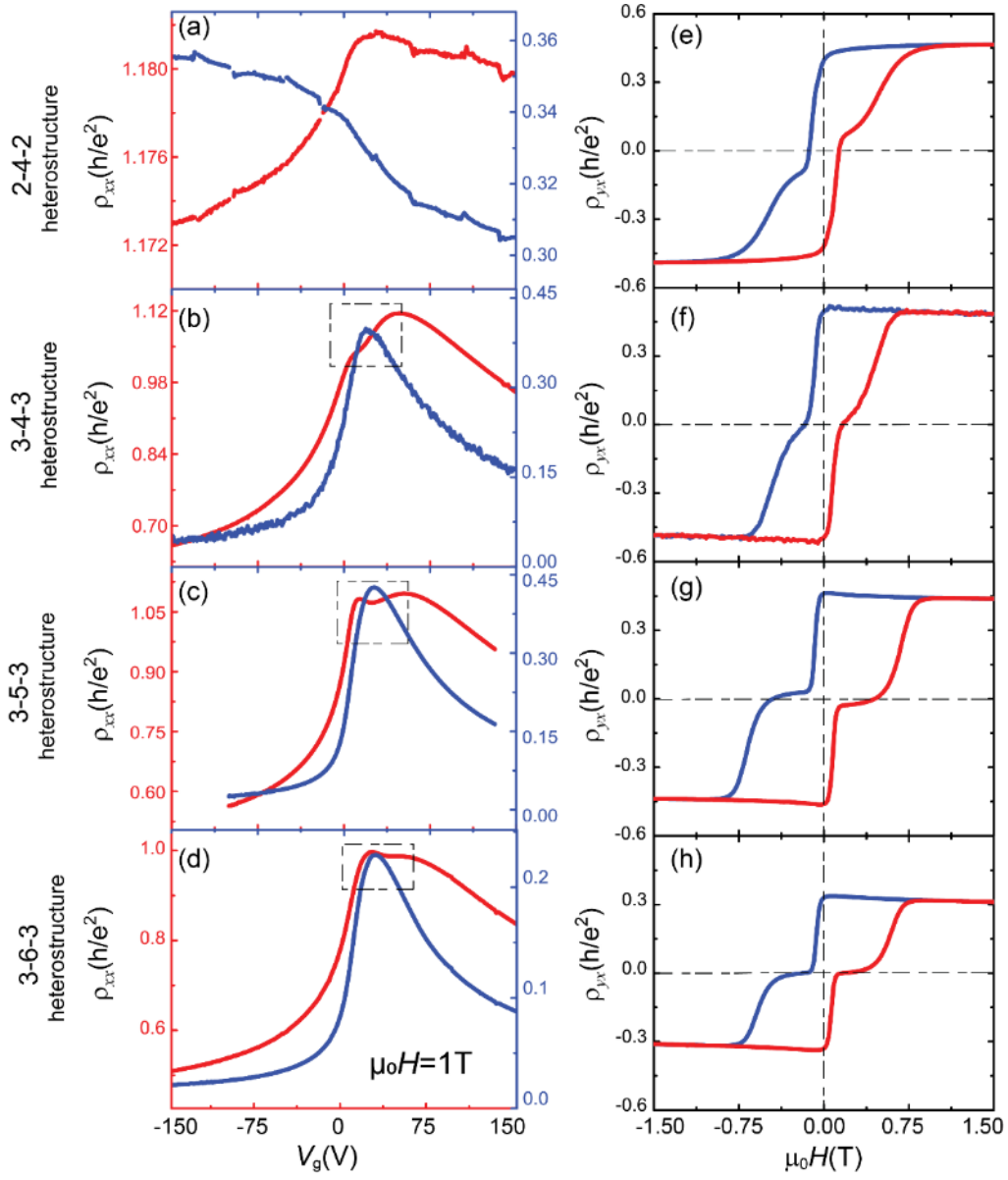

Figure 3.5 Electrical transport characterization of the best sample in each thickness configuration at 2 K. (a - d) V_g dependent ρ_{yx} and ρ_{xx} at 2 K of 2-4-2, 3-4-3, 3-5-3, and 3-6-3 heterostructures. The feature included inside the dashed box indicates the emergence of QAH effect. Figure (e - h) $\mu_0 H$-ρ_{yx} relation that displays a 'plateau' feature due to two H_c of V-/Cr- doped TI layers.

A good growth condition would feature the sample with both an overall quantization and a 'plateau' feature residing on zero. Figure 3.5 shows the electrical transport characterization of

the best sample in each thickness configuration at 2 K during the sample screening process. The most important indication of the QAH effect in the sample screening process is included in the dashed box in Fig. 3.5b - d. When the chemical potential is tuned into the magnetic exchange gap, the ρ_{yx} (blue curves) would reach the maximum and display a peak, while the ρ_{xx} (red curves) would show a dip indicating the influence of dissipationless chiral edge state.

The 'plateau' feature in $\mu_0 H$ - ρ_{yx} relation in Fig. 3.5 is due to two H_c, and the position of the 'plateau' is influenced by the bulk/surface contribution of the two magnetic TI layers. As we can see from Fig. 3.5e - h, the 2-4-2 heterostructure has ρ_{yx} closest to quantized value due to its minimal thickness (ρ_{yx} decreases monotonically as thickness increases from 10 to 12 QL), but the 'plateau' is rather narrow and off from the zero resistance, representing a comparatively weak perpendicular magnetic anisotropy and imbalanced conducting channels from V- and Cr- doped TI layers.

The 3-4-3, 3-5-3, 3-6-3 heterostructures are all showing both 'zero-plateau' feature and a good sign of reaching QAH effect under ultra-low temperature. So, in the following section, we will introduce the transport result of these three configurations under 30 mK.

3.2.3 Gate Dependence of Transport Properties

We systematically studied the magnetoresistance ρ_{xx}, Hall resistance ρ_{yx} under different V_g using a small excitation of 0.3 nA and converted them into conductance. The charge neutral point V_g^0 of these three samples are at +16 V (Fig. 3.6e), +18 V (Fig. 3.7e), -16 V (Fig. 3.8d), respectively, and the theoretically predicted quantized TME effect can be achieved in this V_g. In $\mu_0 H$ dependence of σ_{yx} , we can see an apparent 'plateau' feature representing the anti-parallel alignment of the V- and Cr-doped TI layers with the coercive field of H_{c1} and H_{c2}. At $\mu_0 H > \mu_0 H_{c1}$, two magnetic TI layers have ferromagnetic alignment, and QAH effect emerges with quantized ρ_{yx}, σ_{yx} and vanishing ρ_{xx}, σ_{xx}. When $\mu_0 H_{c1} > \mu_0 H > \mu_0 H_{c2}$, the counter-propagating edge states between the top and bottom surface make ρ_{xx} insulating that exceeds the maximum resistance range of the AC resistivity bridge (~ 40 h/e^2). Large ρ_{xx} can be picked up by ρ_{yx}, so the 'zero-plateau' in our $\mu_0 H$ - ρ_{yx} becomes a rather random electrical fluctuation with the magnitude of a few h/e^2. However, the conductance picture is displaying a textbook 'zero-plateau' in $\mu_0 H$ - σ_{yx} relation and a twin-peak feature in $\mu_0 H$ – σ_{xx}, demonstrating the magnetization reversal of V- and Cr- doped TI layer. Between the twin peaks, σ_{xx} is also zero due to the large ρ_{xx}. Now we confirm the predicted transport response for an axion insulator: $\rho_{yx} = 0$, $\sigma_{yx} = 0$, $\rho_{xx} = \infty$, and $\sigma_{xx} = 0$.

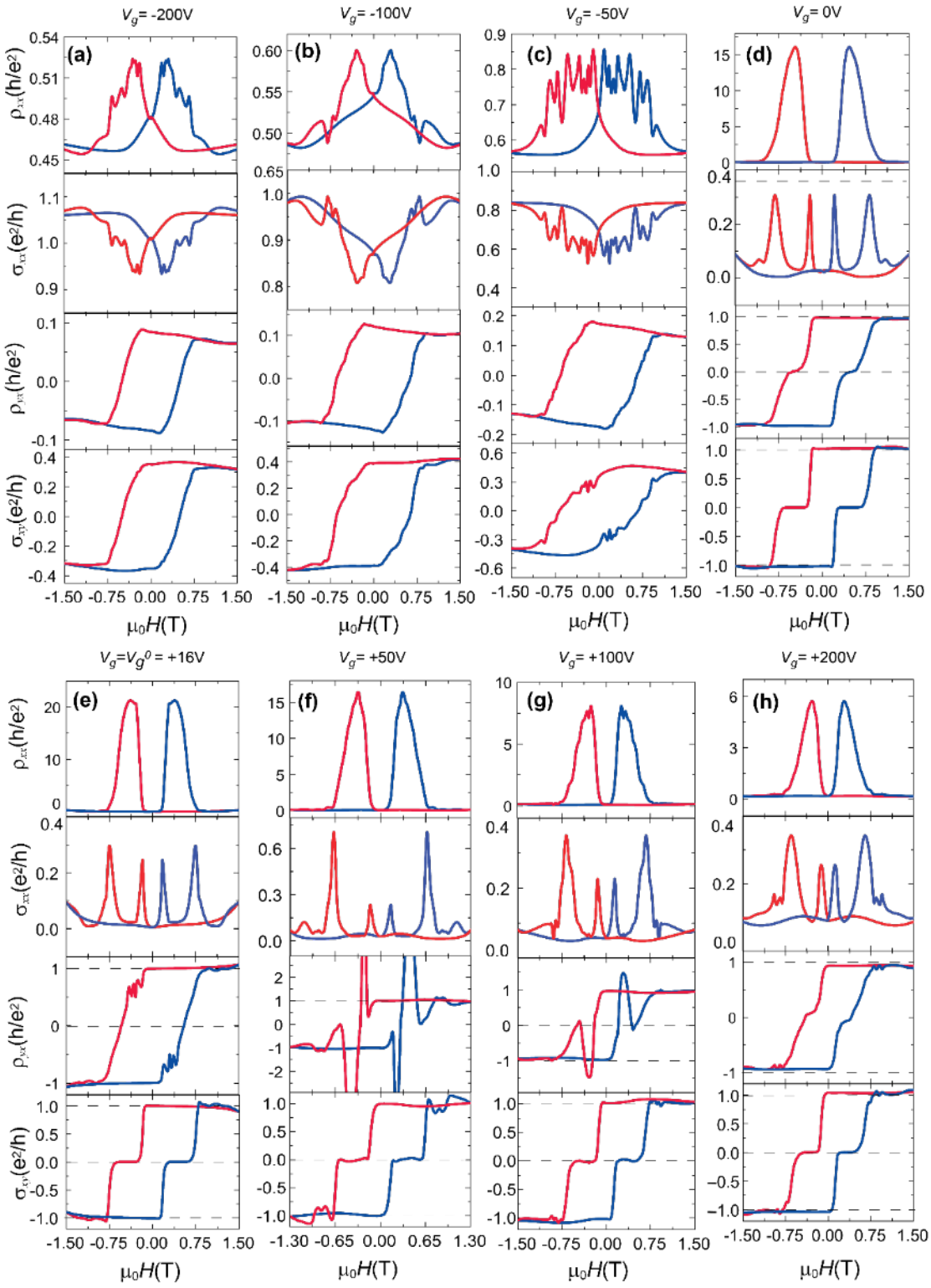

Figure 3.6 $\mu_0 H$ dependence of ρ_{xx}, σ_{xx}, ρ_{yx}, and σ_{yx} of the 3-4-3 heterostructure at 30 mK under different V_g.

(a) -200 V, (b) -100 V, (c) -50 V, (d) 0 V, (e) 16 V, (f) +50 V, (g) +100 V, and (h) +200 V.

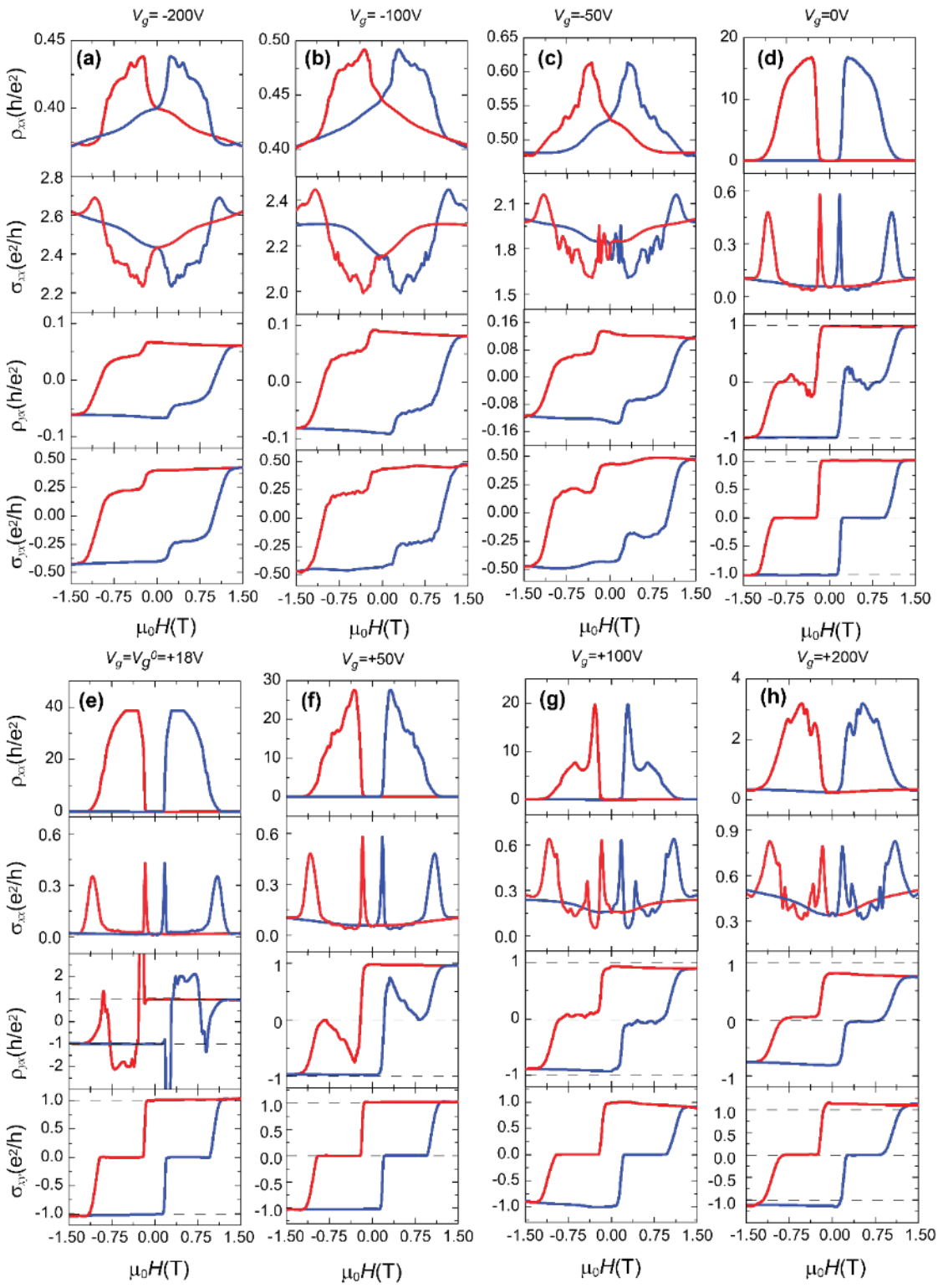

Figure 3.7 μ_0H dependence of ρ_{xx}, σ_{xx}, ρ_{yx}, and σ_{yx} of the 3-5-3 heterostructure at 30 mK under different V_g.

(a) -200 V, (b) -100 V, (c) -50 V, (d) 0 V, (e) 18 V, (f) +50 V, (g) +100 V, and (h) +200 V.

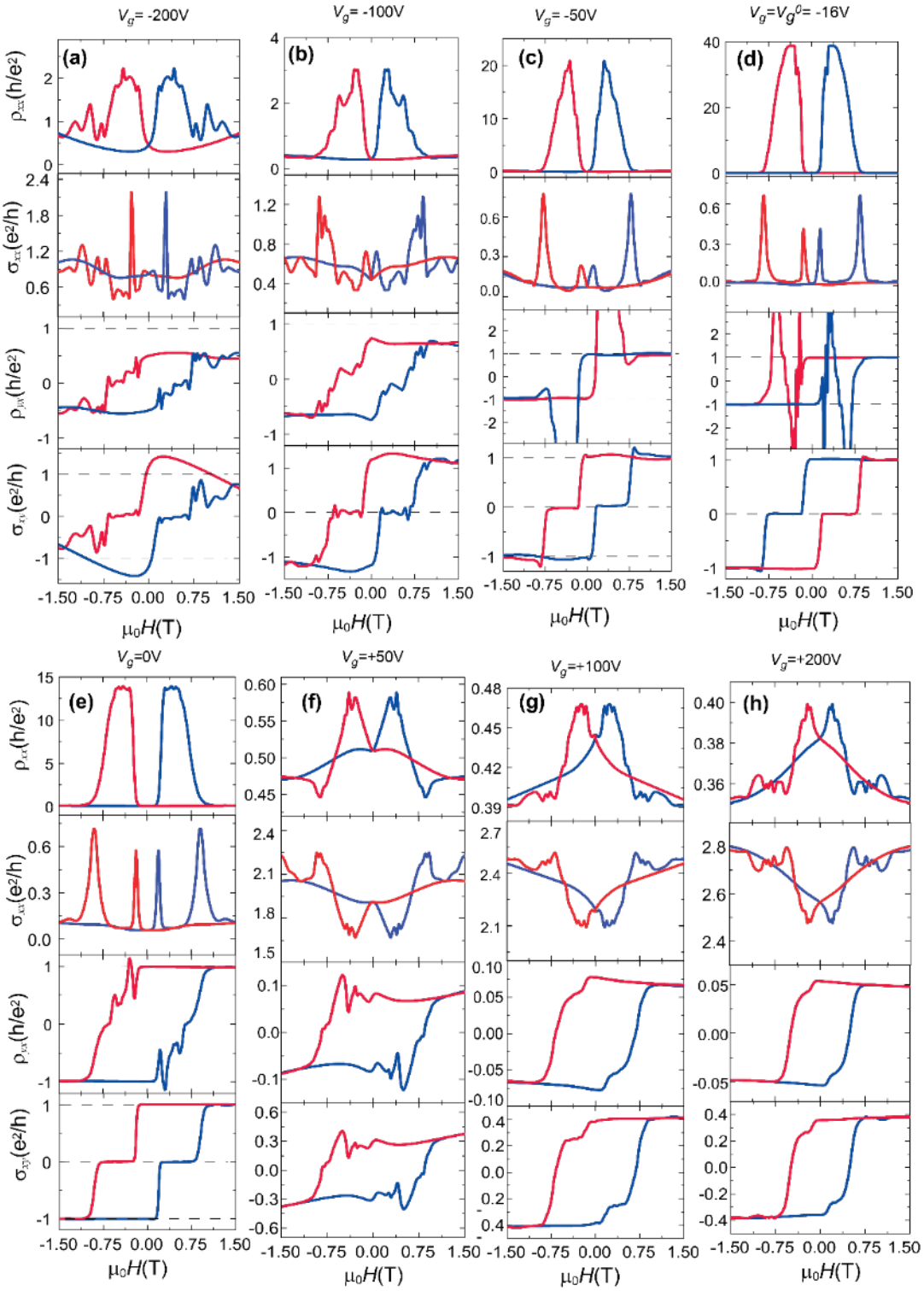

Figure 3.8 μ_0H dependence of ρ_{xx}, σ_{xx}, ρ_{yx}, and σ_{yx} of the 3-6-3 heterostructure at 30 mK under different V_g. (a) -200 V, (b) -100 V, (c) -50 V, (d) -16 V, (e) 0 V, (f) +50 V, (g) +100 V, and (h) +200 V.

With the V_g slightly deviated from V_g^0, the ρ_{xx} is dramatically reduced and has weakened influence to the Hall resistance at $H_{c1} > \mu_0 H > H_{c2}$, so ρ_{yx} starts to show '"real" zero-plateau' feature (Fig. 3.6d, Fig. 3.7d-g), giving us an unambiguous observation of zero Hall resistance feature that is absent in all previous studies.

The transport properties of these three heterostructures when V_g is tuned away from V_g^0 have notable differences between each other. In the 3-4-3 heterostructure, when $V_g < -50$ V, the 'plateau' disappears and only one magnetic transition is seen in the hysteresis loop. This is because the exchange coupling between two magnetic TI layers is greatly enhanced by the substantial amount of the hole-carriers in the system (modulated by the Ruderman-Kittel-Kasuya-Yosida (RKKY) interaction). Thus Cr-/V- doped TI layers in 3-4-3 heterostructure are coupled with each other and act as one uniformly doped magnetic TI, while in other two samples with thicker pure TI spacer, the 'step' feature persists, meaning two magnetic TI layers are not totally coupled with each other. In both 3-5-3 and 3-4-3 heterostructures, the Hall resistance is much smaller at negative V_g (< 0.1 h/e^2) than that at positive V_g (> 0.5 h/e^2) because the exchange gap is closer to the valence band than the conduction band. The 3-6-3 heterostructure shows an opposite V_g dependent behavior. Its small ρ_{yx} at $V_g > 50$ V indicates that the chemical potential may have crossed the bulk conduction band, and the 'step' feature in this V_g region is also similar to the Hall response of 3-5-3 heterostructure at $V_g < V_g^0$.

3.2.4 Exchange Coupling in Heterostructures

In order to demonstrate the weak exchange coupling between the Cr- and V-doped TI layers, we carried out the minor loop measurement at these three samples at $V_g = V_g^0$ under $T = 30$ mK. The magnitude of exchange coupling H_E can be expressed as $\frac{|H^L_{c,minor} - H^R_{c,minor}|}{2}$, where $H^L_{c,minor}$ and $H^R_{c,minor}$ respectively represents the left and right H_c of minor loop[53-54]. From Fig. 3.9, we can calculate the H_E to be ~ 135 Oe (3-4-3), 115 Oe (3-5-3), 65 Oe (3-6-3). The H_E decreases as the thickness of the pure TI increases, and it is at least one order of the magnitude smaller than the difference between H_{c1} and H_{c2}, confirming this heterostructure configuration as a practical platform for antiparallel magnetization. We could expect further weakened H_E as the spacer thickness increases, however, additional dissipative channels may also be introduced and make the realization of the axion insulator state more challenging.

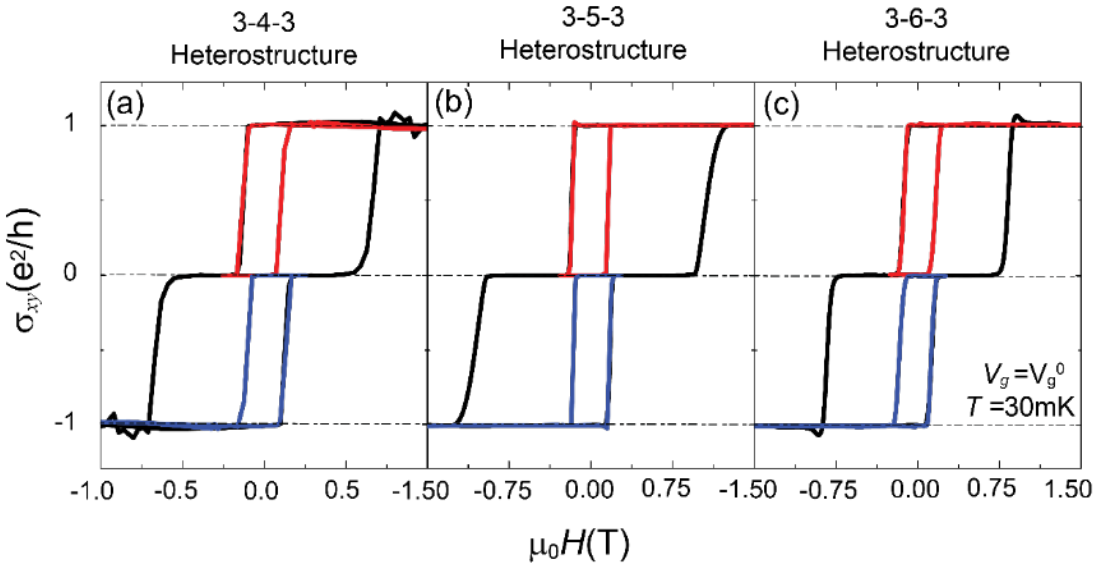

Figure 3.9 Minor loop of $\mu_0 H$ dependence of σ_{yx} at $V_g = V_g^0$ under $T = 30$ mK. (a) 3-4-3 heterostructure, (b) 3-5-3 heterostructure, (c) 3-6-3 heterostructure.

3.2.5 Magnetic Force Microscopy (MFM) Measurements

Apart from the transport measurement, magnetic force microscopy (MFM) measurement also provides conclusive evidence for antiparallel magnetization rather than randomly-formed multi-domains. MFM is based on an Atomic Force Microscope, but with a magnetically coated scanning tip that enables the measurement of magnetic properties on the sample surface. MFM images shown in Fig. 3.10 were taken in 3-5-3 heterostructure at $V_g = 0$ V under T= 5.3 K from -0.1 T to -1 T, and the *in situ* electrical transport is also displayed in Fig. 3.10a. At -0.01 T, the MFM image shows a uniform red color that represents the upward parallel magnetization. As the $\mu_0 H$ ramps up, we can see the domains with opposite spins, presumably from the magnetization reversal of Cr-dope layer, nucleates and shows neutralized magnetization in green color (Fig. 3.10d). The green color prevails as $\mu_0 H$ further increases (Fig. 3.10e) and at -0.09 T, the whole area shows a uniformly green color, corresponding to the 'zero-plateau' in the Hall loop.

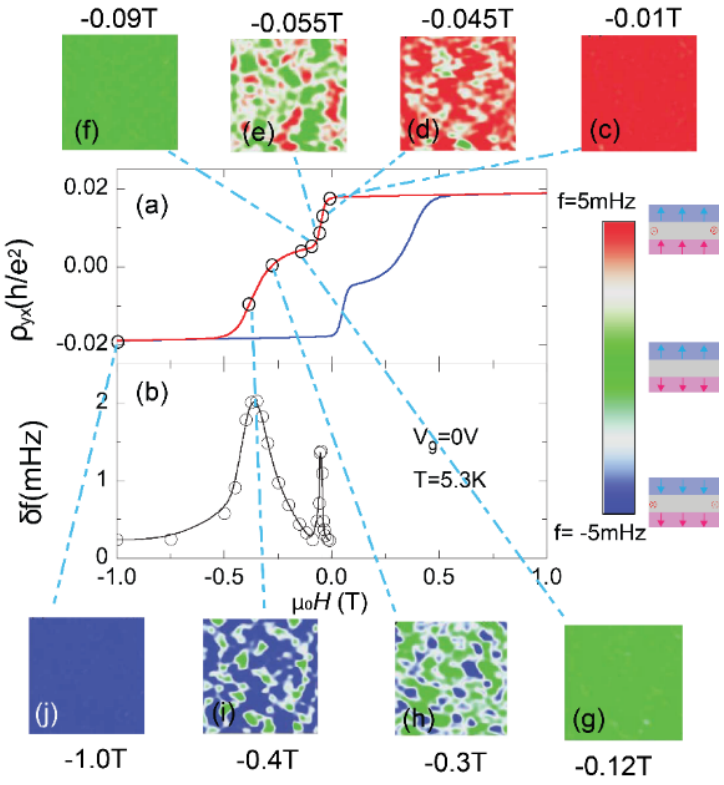

Figure 3.10 $\mu_0 H$ dependence of ρyx and corresponding MFM images of the 3-5-3 heterostructure. (a) $\mu_0 H$ dependence of ρ_{yx} at 5.3 K under $V_g = 0$ V. (b) $\mu_0 H$ dependence of magnetic domain contrasts (δf) from 0 T to 1 T. (c - j) The MFM images of selected $\mu_0 H$ respectively representing the magnetization alignment transiting from parallel upward, then antiparallel, and finally parallel downward. Corresponding Hall resistance is labeled by black circles in (a).

Since the top and bottom layer are not coupled to each other, the pure green color can only be explained as the antiparallel alignment between two magnetic TI layers. We can safely claim that at the lower temperature, with better a quantization and the broadened 'zero-plateau' $\mu_0 H$ window, the TI heterostructures indeed possess an anti-parallel magnetization alignment that gives rise to axion insulator state. In Fig. 3.10h - i, MFM image shows the emergence of the domains with blue color, representing the magnetization reversal of V-doped TI layer. When $\mu_0 H$ is increased to -1T, Fig. 3.10j shows a purely blue color, meaning both two magnetic layers is aligned downward.

Figure 3.10b is the $\mu_0 H$ dependence of magnetic domain contrasts (δf) estimated from the root-mean-square value of the MFM image (Fig. 3.10c - j). It shows two peaks that coincide with the H_{c1} and H_{c2} extracted from the transport result in Fig. 3.10a. Therefore, MFM measurements further verify our heterostructures' capability of hosting an axion insulator state.

3.3 Conclusions and Discussion

We successfully fabricated a series of Cr-doped/non-doped/V-doped TI heterostructures displaying QAH effect and a 'zero-plateau' feature in $\mu_0 H$ dependence of both ρ_{yx} and σ_{yx}. The ρ_{xx} also shows an insulating behavior at the 'zero-plateau' $\mu_0 H$ windows caused by totally reflected conducting electrons. Complemented by MFM measurements, we confirmed the antiparallel magnetization alignment of the top and bottom magnetic layers. Therefore, the transport response unambiguously proves that the quantized Hall conductance in QAH effect is contributed equally by the top and bottom surfaces, and most importantly, it reveals a material system that hosts the axion insulator state and possibly, the TME effect.

However, the magnitude of TME response is expected to be weak, and we have not yet seen its evidence. The recent theoretical study found that by applying a dynamical in-plane magnetization, an axion insulator, unlike the trivial insulator, could host a response current a few orders larger than that of the TME effect[55]. Future experiments can utilize the Cr-doped/non-doped/V-doped TI heterostructure system to explore novel phenomena originate from magnetic dynamics and topological magnetoelectrics. The realization of the axion insulator also paves the way for the applications of a new type of spintronic based on axion electrodynamics.

Chapter 4

Crossover of Quantum Anomalous Hall to Topological Hall Effects

4.1 Chiral Spin Textures and Topological Hall Effect

4.1.1 Spin Textures

A topological insulator has an inverted band structure that gives a non-trivial topology in *k*-space. It cannot be converted to a trivial band insulator by the adiabatic transformation. Interestingly, the real space counterpart of electron momentum, electron spin, can also be represented by topological non-trivial textures in magnetic materials. To characterize the real-space topology, we define a topological charge[56-58] Q to be similar to the Chern number discussed in Chapter 1.3. In magnetically doped TI, topological $\widehat{\boldsymbol{d}}$ vector covers half of a unit sphere and gives a Chern number of $\pm\frac{1}{2}$ on one surface. By borrowing the definition of Chern number and replacing the *k*-space parameters with the real-space equivalents, we have

$$Q = \frac{1}{4\pi}\int \widehat{\boldsymbol{n}} \cdot \left(\frac{\partial\, \widehat{\boldsymbol{n}}}{\partial x} \times \frac{\partial\, \widehat{\boldsymbol{n}}}{\partial y}\right) d^2r$$

where the unit vector $\widehat{\boldsymbol{n}}$ is the direction of magnetization. Q corresponds to the surface the spins cover when mapping the spin texture to the order-parameter space.

These topologically non-trivial spin textures are intensely-studied and can be put into the following categories: spin vortex, meron, bubble, skyrmion, and the chiral domain wall.

Spin vortex is commonly seen in 2D easy-plane magnet, and its spins rotate an angle of 2π around its core. The spins can either always stay in-plane (Fig. 4.1a), or gradually gain an S_z when approaching the center and become out-of-plane at the vortex core (Fig. 4.1b). In this 'out-of-plane'

vortex, the spins are in-plane on the boundary and out-of-plane in the center, the unit vector cover half of a unit sphere, so its topological charge[59] Q is $\pm\frac{1}{2}$. The sign of Q represents the magnetization of the texture core.

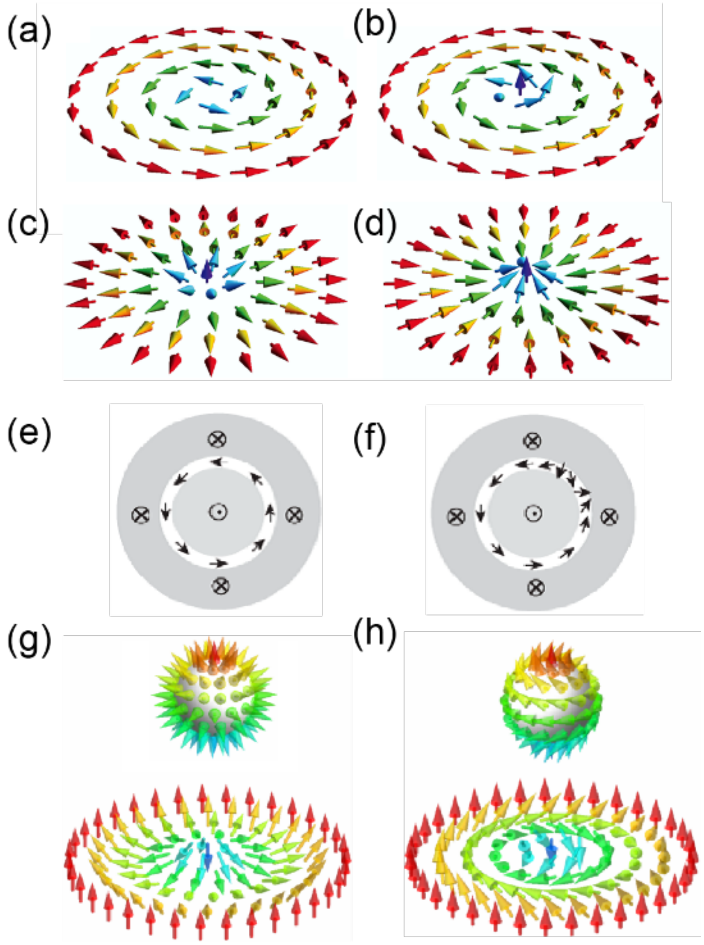

Figure 4.1 Spin textures. (a) Vortex with in-plane spins. (b) Vortex with out-of-plane core with $Q=\pm\frac{1}{2}$. (c) Meron with surrounding spins radially pointing outward. (d) Meron with spins pointing inward. (c) Spin bubble with $Q=\pm 0$. (f) Spin bubble with $Q=\pm 1$. (g) Neel-type skyrmion projected from a hedgehog sphere. (h) Bloch-type skyrmion projected from a combed hedgehog sphere. These figures are reproduced from Liu, J. *et al*., 'Skyrmions: topological structures, properties, and applications.', CRC Press, 2016.

Meron is the spin texture with an out-of-plane core and in-plane surrounding spins radially pointing outward or inward (Fig. 4.1c & d). Its Q is also $\pm\frac{1}{2}$ for the same reason of an 'out-of-plane' vortex[59]. The meron always comes in pairs with the same charge and opposite vorticity[60-61] and gives a total $Q = \pm 1$. The meron pairs are observed in materials with ferromagnetism mediated by RKKY-interaction[61] or have two magnetic layers with antiferromagnetic alignment[62].

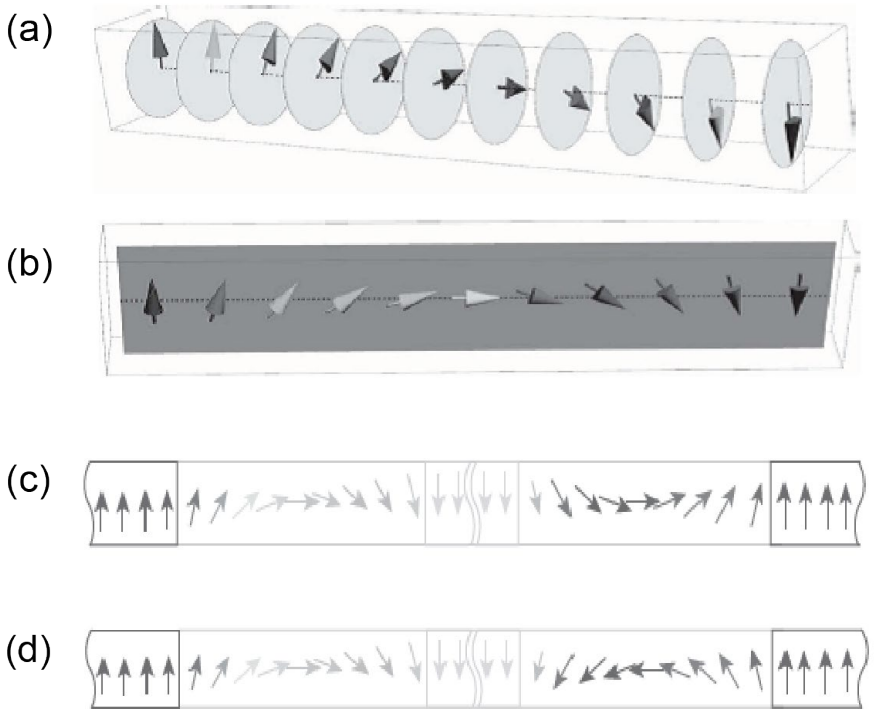

Figure 4.2 The spin configuration of domain walls. (a) Bloch-type domain wall. (b) Neel-type domain wall. (c) Domain wall with zero topological charge. (d) Chiral domain wall with a non-zero winding number. These figures are reproduced from Liu, J. et al., 'Skyrmions: topological structures, properties, and applications.', CRC Press, 2016.

The spin bubble is the spin texture that has opposite perpendicular spin direction between the inner and outer regions[63]. It has a narrow in-plane domain wall. There are two types of domain walls with different topological charges. The one with the spins forming closed-circle domain wall

(Fig. 4.1 e) has $Q = \pm 1$ (Fig. 4.1e), while the other has two vertical Bloch lines[64] with $Q = 0$ (Fig. 4.1f). This kind of spin texture is often seen in magnetic material with strong perpendicular anisotropy.

Skyrmion attracts enormous research attention due to its promising application to spintronic device and its frequent emergence in various kinds of materials. Skyrmion has opposite perpendicular spin direction between its core and the boundary, and a comparatively large intermediate region with continuously rotating spins[65]. Skyrmion also has two types based on the in-plane spin component's orientation. The Bloch-type has the texture by projecting a combed hedgehog sphere into a plane (Fig. 4.1h), and the spins' in-plane orientation is normal to the direction pointing to the core; The Neel-type is the projection of a hedgehog sphere, and the spins' in-plane orientation is pointing toward/outward the core[66] (Fig. 4.1f). Both types have $Q = \pm 1$ and topologically protected stability.

Domain wall is a transitional region filled with canting neighboring spins connecting two domains with opposite magnetization. Similar to the spin-texture of the skyrmion, domain wall can also be categorized into Bloch-type and Neel-type. The Bloch wall has the spins rotating in the plane parallel to the tangential direction of the domain wall (or normal to the dashed line in Fig. 4.2a), while the spins of a Neel wall are all in the plane normal to the domain wall (Fig. 4.2b). When the domain wall encloses a finite area and its spins respect the rotational symmetry, it becomes a chiral domain wall with non-trivial topology. Chiral domain wall has a finite winding number with non-zero Q[67], while the domain wall with zero chirality has no winding number and breaks the rotational symmetry, as shown in Fig. 4.2d.

4.1.2 Origin of Chiral Spin Textures

The dominating interactions in a magnetic system are the Heisenberg exchange interaction and the Zeeman energy term from the external field. In a material with broken inversion symmetry, a noncollinear Dzyaloshinskii-Moriya (DM) interaction that favors the spin canting other than parallel / anti-parallel alignment should be taken into consideration[68-71]. DM interaction is usually decided by the crystal structure, and it can also be found in the transition metal interface of asymmetric magnetic heterostructures.

Thus, the total Hamiltonian of such ferromagnetic material can be written as,

$$H = \sum_{<i,j>} -J\, \boldsymbol{S_i} \cdot \boldsymbol{S_j} + \boldsymbol{D_{ij}} \cdot (\boldsymbol{S_i} \times \boldsymbol{S_j}) - \sum_{i} g\mu_B \boldsymbol{B S_i}$$

where J is the coefficient for Heisenberg exchange interaction, whose sign determines the parallel / anti-parallel alignment. $\boldsymbol{D_{ij}}$ is the DM interaction vector, g is the Landau g-factor and μ_B is the Bohr magneton. The DM interaction makes adjacent spins acquire a finite angle between each other and it is responsible for the formation of chiral spin textures[72-75]. The Hamiltonian also reveals the competition between different interactions, so the chiral spin textures can only be stabilized in a narrow field or temperature range.

4.1.3 Experimental Observations

The chiral spin textures were first verified in bulk MnSi, a cubic B20 compound without space-inversion symmetry in the crystal lattice, using small angle neutron scattering. Three phases of chiral spin textures were observed (Fig. 4.3a - c): conical, helical, and an 'A-phase' representing the formation of skyrmion lattice[76]. Soon the similar results were acquired in Co and Fe doped MnSi[77] and $Fe_{0.8}Co_{0.2}Si$[78].

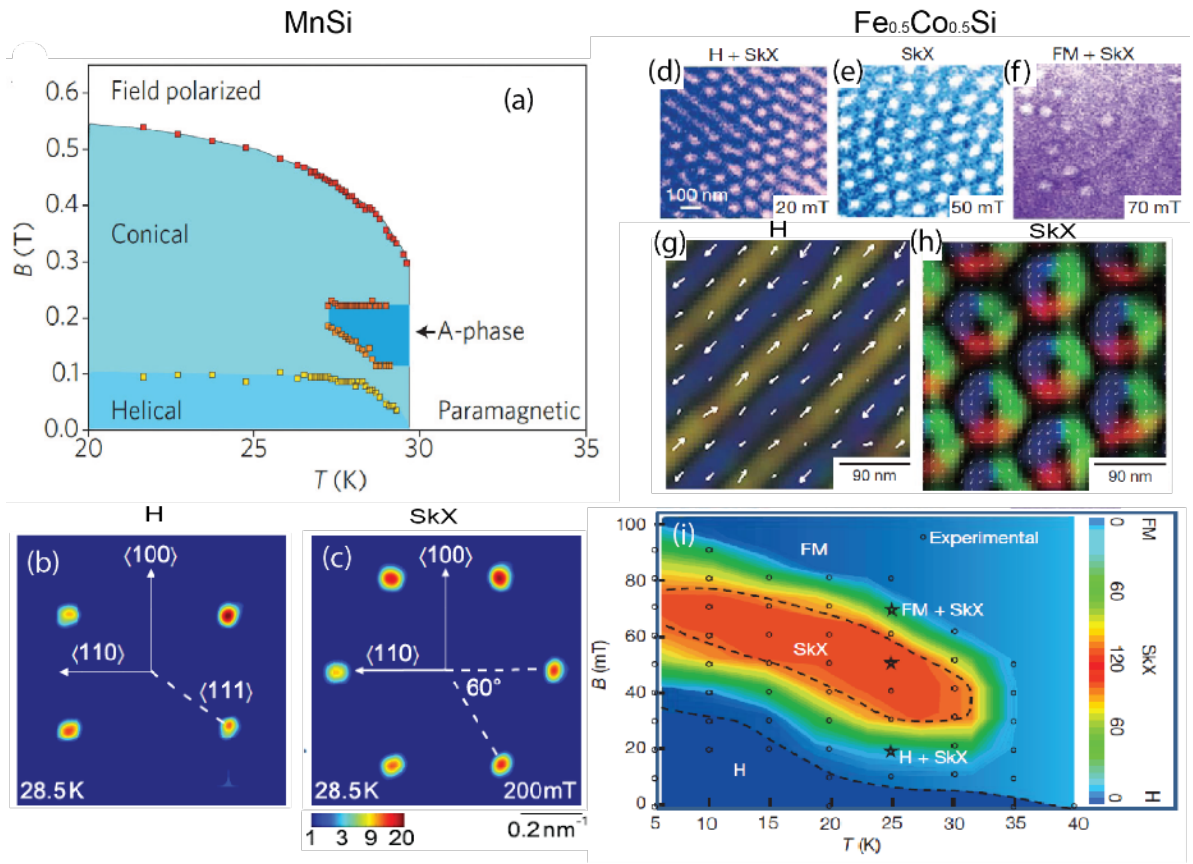

Figure 4.3 Phase diagram for the formation of chiral spin textures. (a) Magnetic phase diagram of MnSi in *B*-*T* parameter space. Three phases were observed: conical, helical, and an 'A-phase' with skyrmion lattice. (b) The small angle neutron scattering data from a helical spin structure at 28.5 K under zero external fields. (c) The small angle neutron scattering result of skyrmion lattice under a finite field of 200 mT. (d - f) LSTM image of helical + skyrmion phase, skyrmion phase, and ferromagnetic + skyrmion phase of $Fe_{0.5}Co_{0.5}Si$ under finite fields. (g) – (h) The Lorentz TEM observation is combined with a magnetic transport-of-intensity equation calculation to show the magnetic components of the helical and skyrmion phase. The spin direction is shown by the white arrows. (i) The magnetic phase diagram of $Fe_{0.5}Co_{0.5}Si$. The stars are corresponding to the *B* - *T* conditions in Figure (d - f). Figure (a - c) are reproduced from Muhlbauer, S., *et al*., Science, 2009. **323** (5916). Figure (d - i) are reproduced from Yu, X.Z., *et al*., Nature, 2010. **465** (7300).

Many spin sensitive imaging tools are used to observe real-space spin textures, such as magnetic force microscopy (MFM)[79-80], magneto-optical Kerr effect (MOKE) microscopy[81-82], Lorentz transmission electron microscopy (LTEM)[72], spin-polarized low energy electron

microscopy (SPLEEM), and spin-polarized scanning tunneling microscopy (SP-STM) [59]. Among these, MFM and MOKE microscopy are extensively utilized for studying the dynamics of the spin textures[81-82], while the latter techniques can microscopically disclose the topology of chiral domain walls and skyrmions.

LTEM is used in the first observation of the skyrmion lattice in $Fe_{0.5}Co_{0.5}Si$[72] (Fig. 4.3d-f). With the help of magnetic transport-of-intensity equation calculation, it can resolve in-plane magnetization along the *x*-*y* direction (Fig. 4.3g - h). It's also able to differentiate the Bloch-type and Neel-type skyrmion[83], although it cannot determine the chirality of the latter spin texture. MnSi[84], FeGe[85] and a multiferroic insulator, Cu_2OSeO_3[86], subsequently exhibited the skyrmion lattice by using LTEM. These materials are measured in the form of thin film and they have a comparatively larger temperature and field range for stable skyrmion lattice than their bulk form[72, 84-89].

SPLEEM can precisely determine the spin chirality. It maps the three-dimensional spin textures on the sample surface with the resolution down to a few nanometers by spatially imaging the deflected or emitted electrons in three orthogonal directions[67, 90-91].

SP-STM combines the conventional STM with a magnetic tip. The tunneling current corresponds to the relative sample-tip magnetization orientation so that the spin structure can be spatially resolved down to the atomic scale. This technique leads to the discovery of atomic-sized skyrmion lattice in Fe/Pd bilayer structure on Ir (111) substrate[92], which is much smaller than the skyrmions in other magnets.

Recently, with the help of continuously developing imaging techniques, spin textures are being found in new materials under more achievable temperature / field conditions:

$La_2Cu_{0.97}Li_{0.03}O_4$ is found to be the first antiferromagnetic material that can host skyrmion lattice[93]; Room temperature ground state skyrmion without the need of external field is artificially realized in patterned Co non-dots on top of a Co/Pd thin film and confirmed by scanning electron microscopy with polarization analysis[80].

4.1.4 Topological Hall Effect

The studies in the last section have revealed spin textures' potential in memory technology. Their intriguing electrical transport property could provide a unique way for the information readout, which also paves the way to future applications.

Topological Hall (TH) effect is a signature transport phenomenon for chiral spin texture. When a conducting electron meets the chiral spin texture, its spin will adiabatically follow the spatial spin distribution of the texture, like it sees a time-dependent emergent virtual magnetic field. The spin would pick up a Berry phase based on the solid angle of the magnetization along the path it travels. A non-zero Berry phase leads to an additional non-zero Hall component, ρ_{yx}^{TH}, superposed on top of the ordinary and anomalous Hall resistance. The magnitude of ρ_{yx}^{TH} is determined by the total topological charge of the spin texture acquired by the conducting electron. So, we have the total Hall resistance:

$$\rho_{yx} = \rho_{yx}^{NH} + \rho_{yx}^{AH} + \rho_{yx}^{TH} \text{ (} \rho_{yx}^{TH} \text{ is non-zero when chiral spin texture emerges)}$$

The TH effect has been experimentally observed in many magnetic materials, such as MnSi[94-95], MnGe[96], FeGe[97], and $SrIrO_3/SrRuO_3$ interface[98-99]. The capable system includes bulk magnets, magnetic thin films / interface, and even nanowires[100].

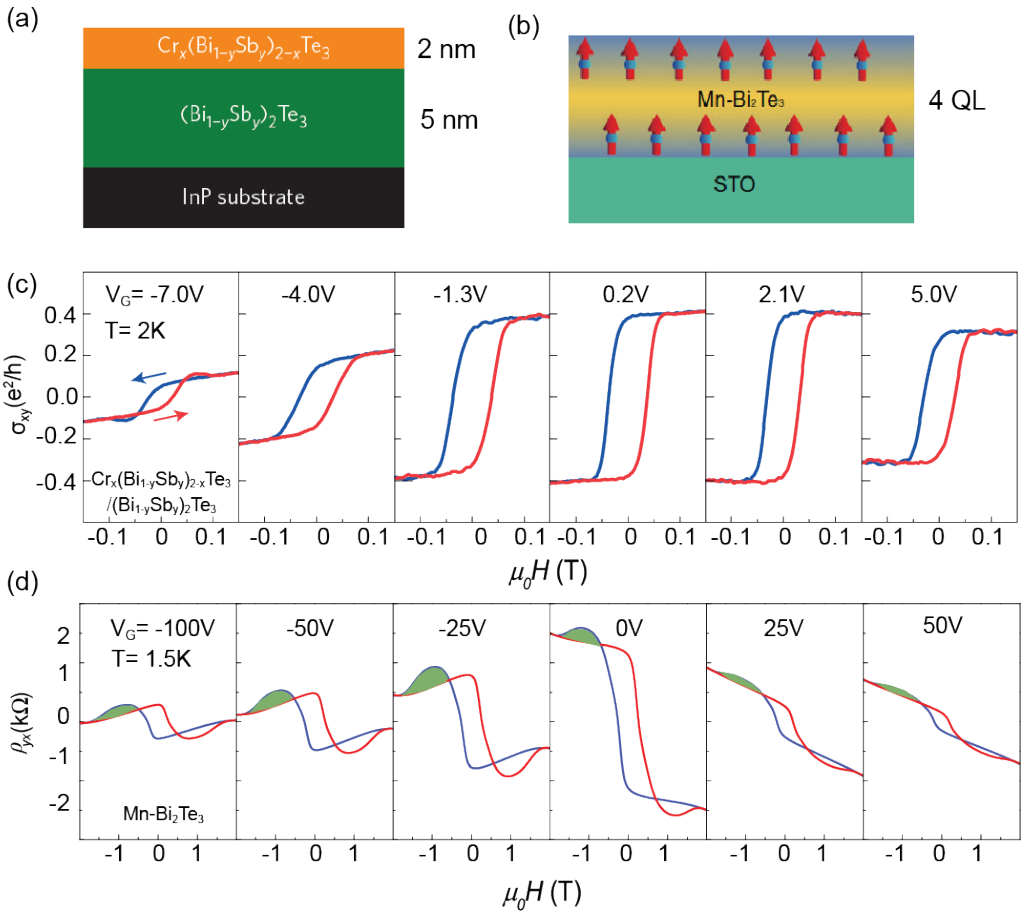

Figure 4.4 TH effect in magnetic TI structures. (a) Schematic of a 2 nm $Cr_x(Bi_{1-y}Sb_y)_{2-x}Te_3$ / 5 nm $(Bi_{1-y}Sb_y)_{2-x}Te_3$ magnetic TI heterostructure. (b) Schematic of a 4 QL Mn-doped Bi_2Te_3. (c) Top gate-dependent Hall conductance of the Cr-doped TI / non-doped TI heterostructure at 2 K. The 'hump' feature emerges at negative top gating voltage. (d) Bottom gate-dependent Hall resistance of the Mn-doped TI at 1.5 K. The TH effect persists at both positive and negative gating voltages. Figure (a) and (c) are reproduced from Yasuda, K., *et al.*, Nature Physics, 2016, **12**, 555-559. Figure (b) and (d) are reproduced from Liu, C., *et al.*, Physical Review Letters, 2017, **119** (176809).

Recently, the TH effect was also reported in magnetically doped TI films and heterostructures[101-102]. Yasuda *et al.* systematically studied the topological Hall effect in a 2nm $Cr_x(Bi_{1-y}Sb_y)_{2-x}Te_3$/5nm $(Bi_{1-y}Sb_y)_{2-x}Te_3$ heterostructures grown on the InP substrate (Fig. 4.4 a). They found the Hall resistance, as well as the Hall conductance, 'overshot' the ordinary Hall

resistance during the magnetization reversal and produced a 'hump' feature around the coercive field at the negative top gating voltages (Fig. 4.4 c). Their theoretical calculation agreed with the observation and indicated that this TH effect is originated from the Neel2-type skyrmion formation. No ρ_{yx}^{TH} was found when they increased the thickness of $Cr_x(Bi_{1-y}Sb_y)_{2-x}Te_3$ from 2 nm to 3 nm while keeping the $(Bi_{1-y}Sb_y)_{2-x}Te_3$ as 5 nm, indicating the less favorable skyrmion formation when the magnetic exchange coupling prevailed over the DM interaction.

Another instance for magnetic TI that hosts TH effect is the epitaxy-grown Mn-doped Bi_2Te_3 on STO substrate (Fig. 4.4 b) discovered by Liu *et al.* [102]. In this uniformly doped TI film, ρ_{yx}^{TH} was found to be non-zero when the thickness was 4 QL at both positive and negative bottom gating voltages (Fig. 4.4 d), while no TH effect was observed in a thicker or thinner film. This finding indicated the possible correlation between the effective DM interaction and surface electronic band structure, where the DM term was suppressed under the large hybridization gap in a less than 4 QL thick Mn-Bi_2Te_3. Their experimental result showed that the TH effect disappeared when the 4 QL thick Mn-Bi_2Te_3 was capped with Te layer, in which the asymmetric potential was dramatically reduced. This research further verified the importance of broken inversion symmetry to the DM term.

These two studies provide us a guideline to realize TH effect in a magnetic TI: (i) The DM interaction has to be balanced with the magnetic exchange couplings. The magnitude of the exchange coupling can be roughly controlled by the thickness of the magnetic TI layer. Similar to the narrow B-T window for the stable skyrmion texture, there also exists an optimal magnetic TI thickness; (ii) Inversion symmetry needs to be broken for achieving non-zero DM interaction. Since the bulk of TI respects the inversion symmetry, the only place to host the DM interaction are the surfaces. In a uniformly doped magnetic TI film, the top and bottom surfaces are strongly

coupled, so their DM vectors have opposite directions and cancel out each other. In the $Cr_x(Bi_{1-y}Sb_y)_{2-x}Te_3/(Bi_{1-y}Sb_y)_{2-x}Te_3$ heterostructure, the bottom surface is non-magnetic TI, so only the top surface has DM interaction and the total topological charge is non-zero. In the Mn-Bi_2Te_3 film, the top surface is exposed to vacuum while the bottom surface is on the substrate. The potential difference between two surfaces also results in a finite net DM term.

Since both the QAH and TH effect can be realized in the magnetic TI films, it is natural to ask whether these two topology-related phenomena can be achieved in a single sample. In the previous two studies, their exchange gap is overlapped by other bands and the chemical potential is buried under the bulk band, so their Hall resistances are far away from the quantized value. Thus, those systems are unlikely to unify both phenomena. In the next chapter, we will discuss our sample configuration to address this question.

4.2 Unifying Topological Hall and Quantum Anomalous Hall Effect

4.2.1 Sample Configuration

A magnetic TI film should satisfy three conditions to simultaneously facilitate QAH and TH effect: (i) The time-reversal (TR) symmetry is broken, which is the common prerequisite for both the QAH and TH effect; (ii) The chemical potentials of the top and bottom surfaces can be simultaneously tuned into the magnetic exchange gaps, which is essential for the QAH effect; (iii) A significant DM interaction can be created, which is required for the TH effect.

To meet the listed specifications, we started with a TI-based heterostructure with an undoped TI layer sandwiched between two Cr-doped TI layers. Then we tried different thickness of each layer to find the optimal configurations for unifying both phenomena. Such sandwich heterostructure has the following advantages: (i) Both the top and bottom surface states are

separately gapped by the magnetization, so the QAH effect is reachable. With our previous successful experience of growing 'axion' insulator heterostructures, we are able to tune the chemical potential into the charge neutral point of each layer. A similar tri-layer heterostructure is even reported to have a higher realization temperature of QAH effect[13]. (ii) The nonmagnetic TI layer serves as a spacer to decouple the magnetic exchange interaction between the two magnetic TI layers[18, 103-104]. As a result, the magnetic moments in each magnetic TI layer interact only with their own surface state, so the DM interaction of each layer independently makes a contribution to the total topological charge and maximizes the TH effect.

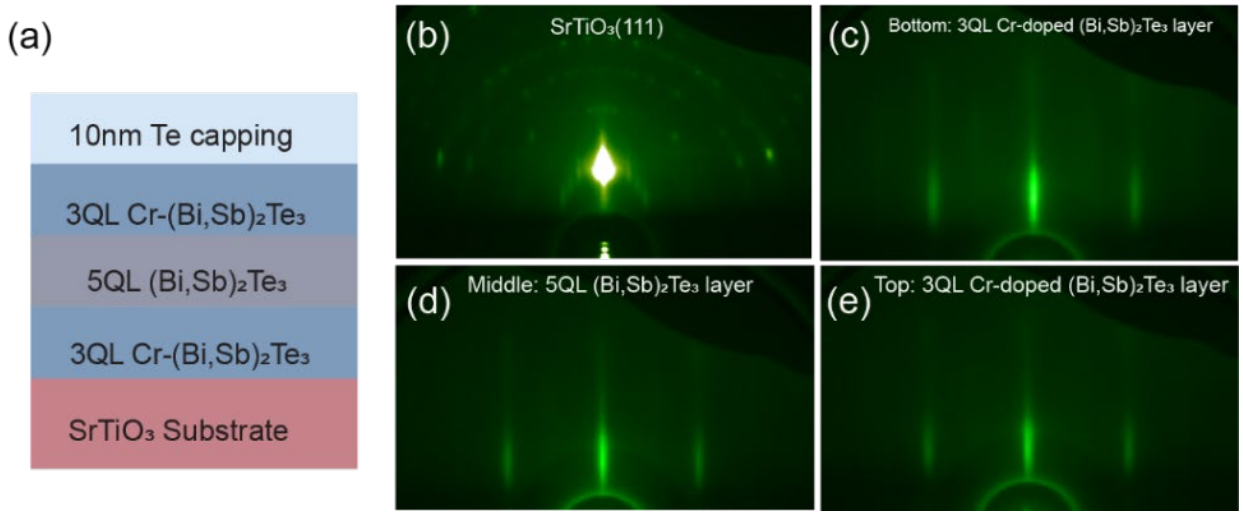

Figure 4.5 Schematic of the 3-5-3 sample and its RHEED pattern during the MBE growth. (a) Schematic of the 3QL $(Bi_{1-x}Sb_x)_{1.85}Cr_{0.15}Te_3$/5QL $(Bi_{1-x}Sb_x)_2Te_3$/3QL $(Bi_{1-x}Sb_x)_{1.85}Cr_{0.15}Te_3$ sample. (b) RHEED pattern of the heat-treated substrate. (c)-(e) RHEED patterns of the TI layer during each stage of the MBE growth.

Our sample screening results using PPMS shows target transport response in the structure of a 3 QL $(Bi_{1-x}Sb_x)_{1.85}Cr_{0.15}Te_3$/5 QL $(Bi_{1-x}Sb_x)_2Te_3$/3 QL $(Bi_{1-x}Sb_x)_{1.85}Cr_{0.15}Te_3$, and the sample schematic is shown in Fig. 4.5a. We will show the transport results of 3-5-3 sandwich structure in Sec. 4.2.3 and discuss other thickness configuration in Sec. 4.2.6.

4.2.2 Sample Structure Characterization

Figure 4.5b - d shows the RHEED patterns during the MBE growth of the sandwich heterostructure. The clear reconstruction pattern of heat-treated STO (111) substrate indicated the highly smooth surface, which is crucial for epitaxy growth. The sharp and streaking '1×1' pattern observed in each stage of the growth indicates the high-quality of the magnetic/non-magnetic/magnetic TI sandwich heterostructure samples.

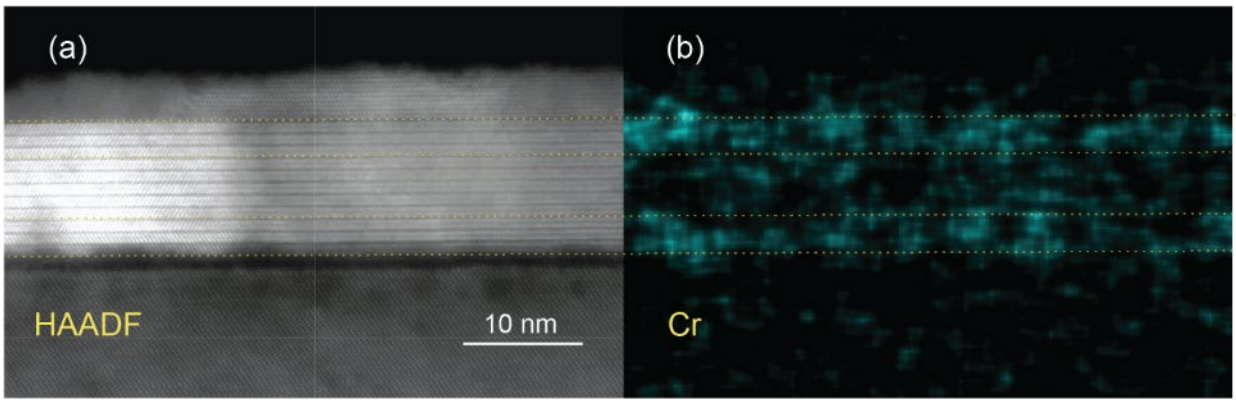

Figure 4.6 HAADF-STEM image and EDS mapping of the 3-5-3 sample. (a) The HADDF-STEM image of the sample cross section. Te capping layer, the 11 QL heterostructure, STO substrate can be distinguished. (b) EDS map of the Cr ions of this 3-5-3 sample.

Figure 4.6 shows a HAADF-STEM image of the 3-5-3 sample. The crystal structures of Te capping layer, the 11 QL heterostructure, and the STO substrate can be distinguished. The corresponding EDS mapping of Cr (Fig. 4.6b) shows that the Cr signal is stronger in the top and the bottom 3 QL TI layers, consistent with the Cr doping (~ 7.5 %) in these two layers.

4.2.3 Transport Results

In the 3-5-3 sample, the FM order at low-temperatures gaps out the top and bottom surface states, and the chemical potential is located inside the magnetic exchange gaps of both surfaces, so the transport result shows a good QAH effect with a perfectly quantized Hall value and

vanishing longitudinal resistance at the base temperature of 30 mK under the $V_g = 0$ V (Figure 4.7). With the increasing temperature, the sample deviates from the QAH state and shows transport properties of a conventional FM material: hysteretic ρ_{yx} loops and butterfly-shaped ρ_{xx}. The H_c is around 0.18 T at 30 mK. Since the peaks in ρ_{xx} are caused by the insulating bulk state when the edge state is disturbed during the magnetization reversal, they indicate a decreasing H_c as temperature increases, which is also reflected in the ρ_{yx} with a shrinking hysteretic loop. The T_c of this sample is determined to be ~ 19 K (Fig. 2.4).

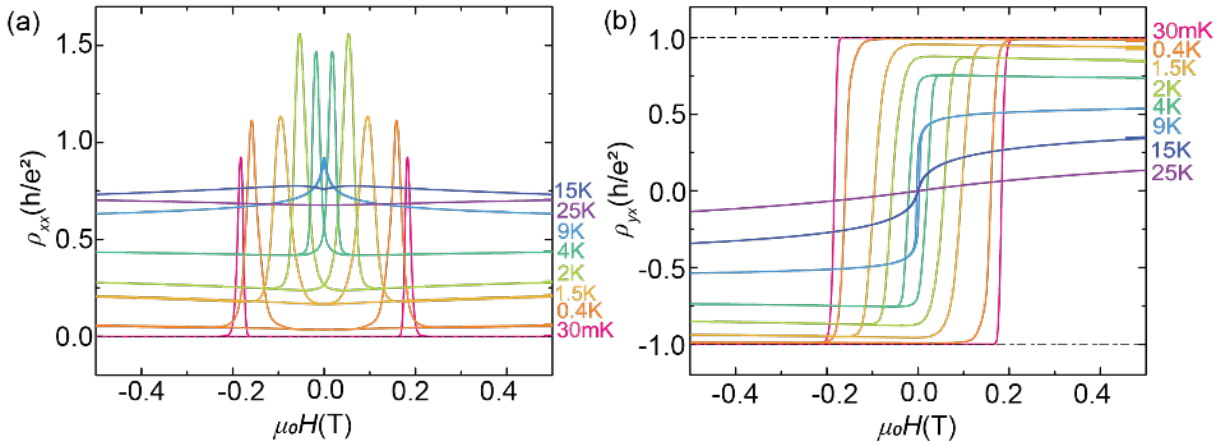

Figure 4.7 The $\mu_0 H$-dependent transport data at $V_g = 0$ V of 3-5-3 sample under various temperatures. (a) $\mu_0 H$ dependence of ρ_{xx} at varying temperatures under $V_g = 0$ V. (b) $\mu_0 H$ dependence of ρ_{yx}. At $T = 30$ mK, the quantized ρ_{yx} and the vanished ρ_{xx} suggest this sandwich sample in the QAH state when $V_g = 0$ V. ρ_{yx} deviates from quantized value as temperature increases.

With the application of V_g, the measured ρ_{yx} during the magnetization reversal 'overshoots' the conventional Hall resistance, and a 'hump' feature extending a few hundred oersteds above $\mu_0 H_c$ appears in ρ_{yx} curves. At a much higher field, where the spins are presumably aligned to the same direction, the 'hump' merges with normal Hall resistance and it is muted until the next magnetization reversal. Similar to the result in Mn-doped Bi_2Te_3, the 'hump' feature is observed

under both positive and negative gating voltage, and it is a shred of strong evidence for the existence of chiral magnetic textures in the real-space.

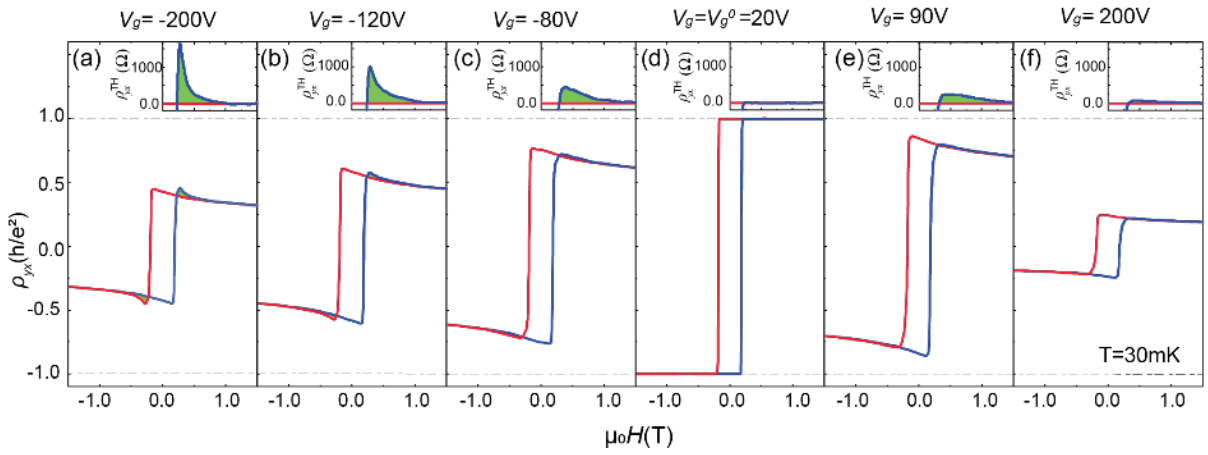

Figure 4.8 Crossover of QAH to TH effects at T = 30 mK. (a - f) $\mu_0 H$ dependence of ρ_{yx} under varying V_g. The sample harbors a perfect QAH state when $V_g = V_g^0 = +20$ V. ρ_{yx} deviates from the quantized value and a "hump" feature appears in ρ_{yx} (green shadowed) when V_g is tuned away from V_g^0. Inset of (a - f): the offset resistance of ρ_{yx} when the external $\mu_0 H$ is swept upward and downward, which is used as TH component ρ_{yx}^{TH}.

In order to single out the TH component ρ_{yx}^{TH}, we subtract ρ_{yx}^{NH} and ρ_{yx}^{AH} from ρ_{yx}. Here we interpret the offset resistance between upward and downward $\mu_0 H$ sweeps (green shadow in the insets of Fig. 4.8) as the ρ_{yx}^{TH} for the following reasons: In the positive $\mu_0 H$ regime, during the downward $\mu_0 H$ sweep (red curves in Fig. 4.8), the system should be in a ferromagnetic state without any spin texture and thus the ρ_{yx} should include ρ_{yx}^{NH} and ρ_{yx}^{AH}. For the upward $\mu_0 H$ sweep (blue curves), the system undergoes a magnetic transition around the $\mu_0 H_c$ and chiral spin textures can be formed. In this situation, all three Hall contributions exist and $\rho_{yx}^{NH} + \rho_{yx}^{AH}$ keeps the same value during the downward $\mu_0 H$ sweep. Thus, the ρ_{yx}^{TH} can be extracted by the magnitude difference between the red and blue curves.

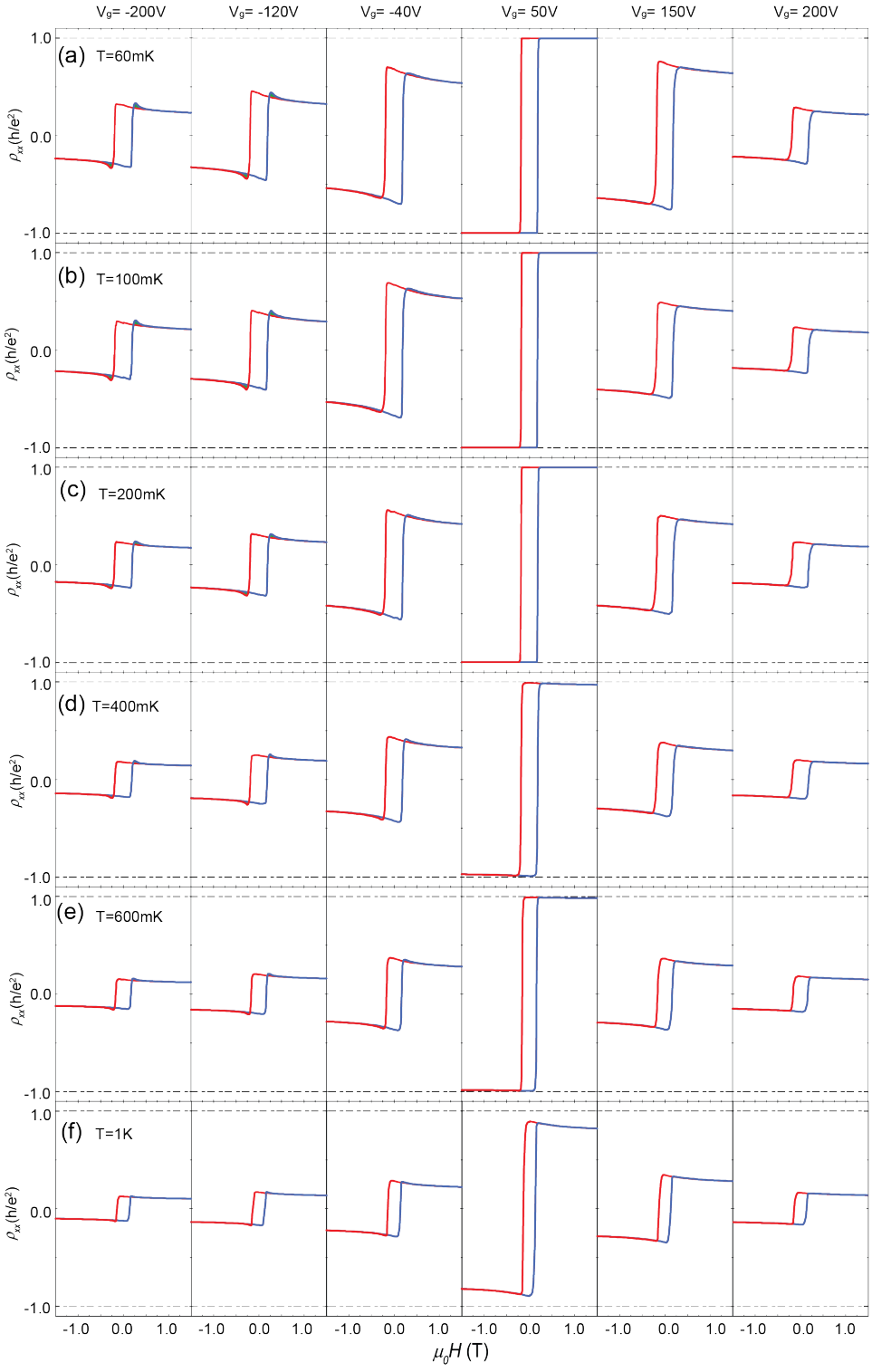

Figure 4.9 μ₀H dependence of ρ_{yx} of the 3-5-3 sample under different V_g and temperatures. (a) 60 mK, (b) 100 mK, (c) 200 mK, (d) 400 mK, (e) 600 mK, and (f) 1 K.

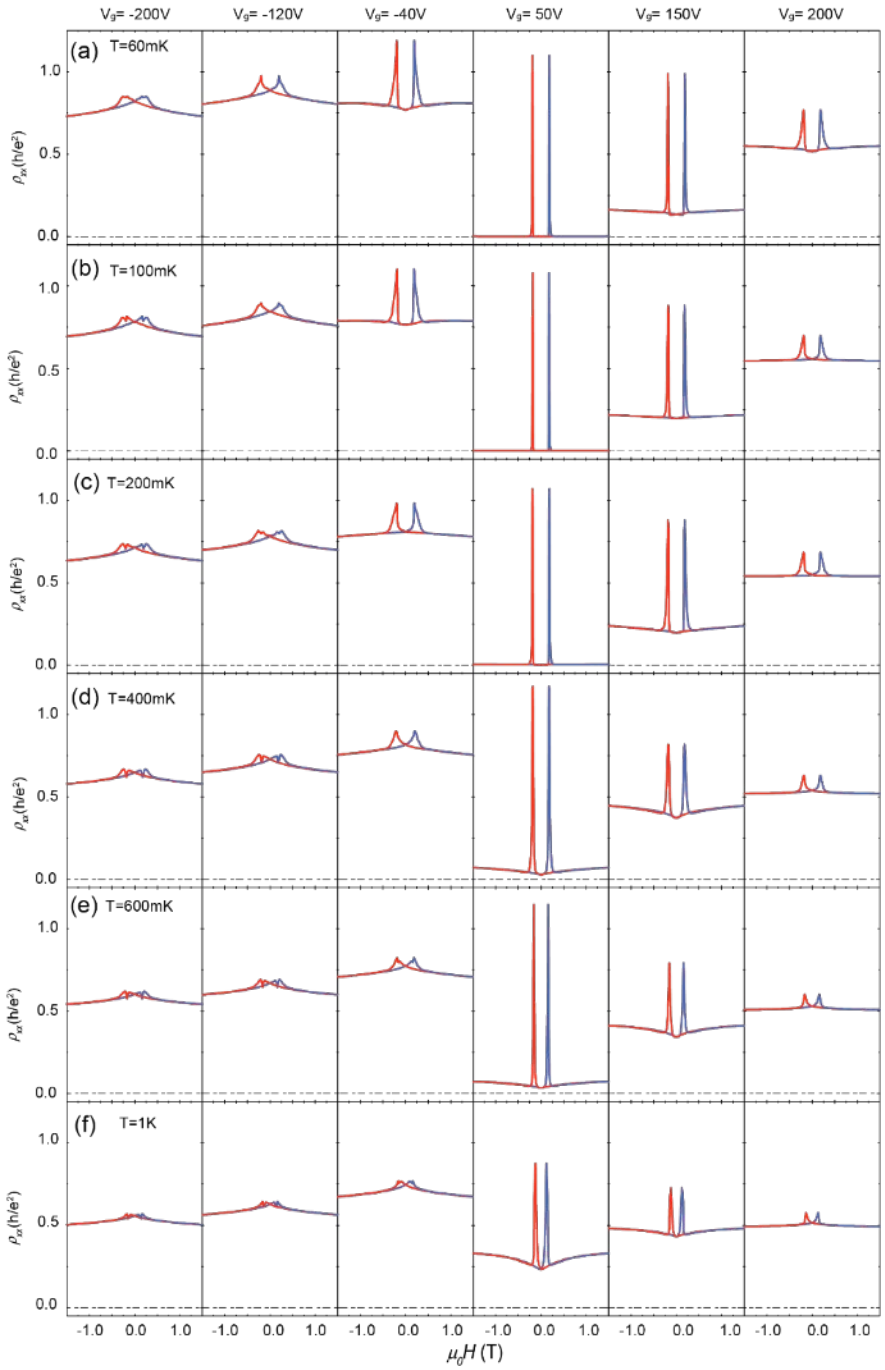

Figure 4.10 $\mu_0 H$ dependence of ρ_{xx} of the 3-5-3 sample under different V_g and temperatures. (a) 60 mK, (b) 100 mK, (c) 200 mK, (d) 400 mK, (e) 600 mK, and (f) 1 K.

To further study the crossover of the QAH to the TH effect, we systematically measured the $\mu_0 H$ dependence of ρ_{yx} under various V_g from 60 mK to 1 K. Figure 4.9 and 4.10 display the magnetic field $\mu_0 H$ dependence of the Hall resistance ρ_{yx} and the longitudinal resistance ρ_{xx} of the 3-5-3 sample. When $V_g = V_g^0 = +50$ V and $T < 400$ mK, this sample exhibits the perfect quantum anomalous Hall (QAH) state with quantized ρ_{yx} and vanishing ρ_{xx}. For $V_g < V_g^0$ or $V_g > V_g^0$, with increasing the dissipative channels, ρ_{yx} decreases and ρ_{xx} increases. We note that ρ_{xx} shows a twin-peak feature near H_c regime when $V_g = -200$ V and $T = 60$ mK, and this twin-peak feature at $V_g = -200$V become more obvious with increasing T. The V_g at which ρ_{xx} shows this twin-peak feature extends to -40 V at $T = 1$ K. This phenomenon is likely due to the weakened magnetic proximity induced FM orders in the middle TI spacer layer. More systematic studies about the dip feature in the ρ_{xx} near $\mu_0 H_c$ are needed.

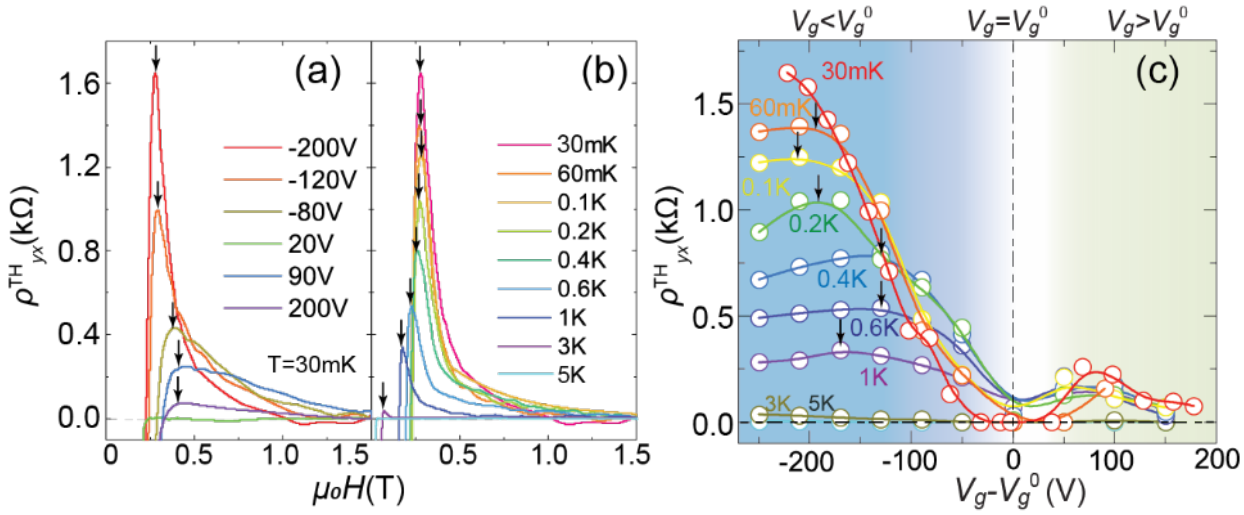

Figure 4.11 TH component ρ^{TH}_{yx} at different V_g and T. (a) $\mu_0 H$ dependence of the ρ^{TH}_{yx} at varying V_g under T=30 mK. (b) $\mu_0 H$ dependence of the ρ^{TH}_{yx} when $V_g = V_g^{TH, max}$ at different T. Maximum ρ^{TH}_{yx} =1.65 K at $T = 30$ mK and disappears at $T = 5$ K. (c) The maximum ρ^{TH}_{yx} as a function of (V_g - V_g^0) at different T. ρ^{TH}_{yx} shows a peak denoted by the arrows when $V_g < V_g^0$.

We summarize the behavior of ρ_{yx}^{TH} in Fig. 4.11. At T = 30mK (Fig. 4.11a), ρ_{yx}^{TH} shows high and narrow peaks up to 1.6 kΩ at negative V_g, a flat zero plateau at $V_g = V_g^0 = 20$ V, as well as board but smaller humps at positive V_g. The peak location (denoted by the arrows) in each curve increases as V_g is tuned from negative to positive. Figure. 4.11b shows ρ_{yx}^{TH} - $\mu_0 H$ curves at different temperatures highlighting the TH hump. These curves show that the TH effect persists up to at least 3 K. The peak location decreases as temperature increases, tracking the decreasing H_c. The maximum ρ_{yx}^{TH} is much larger than the TH resistances observed in all previous studies on metallic systems[94-99, 101-102, 105]. A larger ρ_{yx}^{TH} indicates the higher density or the smaller size of the chiral magnetic textures in our sandwich heterostructures[99, 102, 106].

Figure 4.11c summarized the V_g - dependent maximum ρ_{yx}^{TH} under varying temperatures. The graph clearly shows three regions: the QAH region, the $V_g < V_g^0$, and the $V_g > V_g^0$ regions. In the QAH region, we noted that the DM interaction is still able to give rise to chiral spin textures (see details in Sec. 4.3.2), however, the only conducting channel is the dissipationless chiral edge state. So ρ_{yx} is fully quantized and ρ_{yx}^{TH} is able to reach 0 when T is below 60 mK. When 0.1 K < T < 1 K, however, ρ_{yx}^{TH} becomes non-zero due to the thermally excited electrons in the surface / bulk band. At T > 1K, ρ_{yx}^{TH} vanished again because the thermal fluctuation prevents the formation of the spin textures.

In the $V_g < V_g^0$ region, when V_g is tuned from -10 V to -200 V under any T smaller than 1K, ρ_{yx}^{TH} increases to its maximum and then saturates, if not decreases, at a finite $\mu_0 H$. In the $V_g > V_g^0$ region, ρ_{yx}^{TH} also at peak around $V_g - V_g^0 = +90$ V, but with a much smaller peak magnitude than $V_g > V_g^0$ region. We attribute the asymmetry between $V_g < V_g^0$ and $V_g > V_g^0$ to the asymmetric surface / bulk band structure of TI. Prior theoretical and experimental studies[107-109] show that the Dirac points of the surface band are closer to the top bulk valence band than the conduction band.

Naively, we can regard the ρ_{yx}^{TH} in $V_g < V_g^0$ region is attributed to both the bulk valence band and surface states. A hint of 'kink' is found at V_g = -60 V for the temperature scan T = 30 mK. This is likely due to the initial crossing of the maximum of the bulk valence bands. While in the ρ_{yx}^{TH} in $V_g < V_g^0$ region, chemical potential cannot be tuned into the bulk conduction band, so the TH feature is solely induced by the chemical potential crossing the surface states[108-109]. Theoretical calculations and other details will be discussed in Section 4.3.

The results reported here have been reproduced on two samples measured in the dilution refrigerator and more than ten samples measured in PPMS.

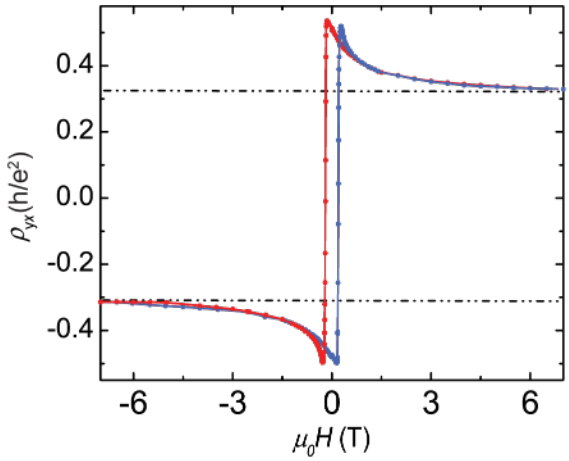

Figure 4.12 $\mu_0 H$ dependence of ρ_{yx} of the 3-5-3 sample under V_g = -180 V at T = 30 mK.

We note that the slope of the Hall traces at high magnetic fields (0.5 T < μ_0H < 1.5 T) is always negative in both the $V_g < V_g^0$ and the $V_g > V_g^0$ regions, which suggests that the standard Hall coefficient R_N cannot be used to estimate carrier density near the QAH insulating regime. Figure 4.12 shows the high $\mu_0 H$ Hall traces of the 3-5-3 sample under V_g = -180 V at T = 30 mK. At low $\mu_0 H$, we can see the feature of the TH effect, while at high $\mu_0 H$, the Hall trace shows negative slope and the ρ_{yx} saturates when $\mu_0 H$ = 7 T.

4.2.4 Conductance Results

In order to exclude the possibility of large ρ_{xx} for causing the 'hump' feature in ρ_{yx} near $\mu_0 H_c$ regime, we convert the ρ_{yx} into the Hall conductance σ_{xy}. We can still see the TH-like 'hump' feature in both the $V_g < V_g^0$ and the $V_g > V_g^0$ regimes, but the V_g for the maximized σ_{xy} is changed. Figure 4.13 shows $\mu_0 H$ dependence of σ_{xy} under different V_g, and the insets show the offset conductance, σ_{xy}^{TH}. When $V_g < V_g^0$, σ_{xy}^{TH} still displays the 'hump' feature. We note that the σ_{xy}^{TH} show a maximum at V_g= -80 V instead of -200 V for ρ_{yx}^{TH}. This is because the chemical potential crosses the top of the bulk valence band, consistent with the 'kink' in ρ_{yx} at V_g = -60 V shown in Fig 4.11c. When $V_g = V_g^0 = 20$ V, σ_{xy}^{TH} vanishes due to the existence of the QAH effect. When V_g = 200 V, only a trace of σ_{xy}^{TH} is observed.

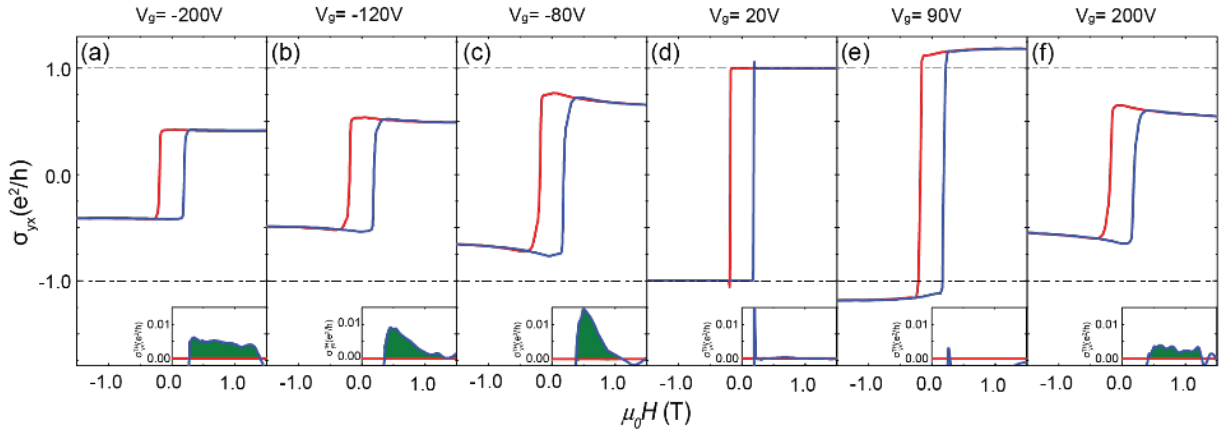

Figure 4.13 $\mu_0 H$ dependence of the Hall conductance σ_{xy} of the 3-5-3 sample under different V_g and T = 30 mK. (a) -200 V, (b) -120 V, (c) -80 V, (d) 90 V, (e) 200 V. Inset: the offset conductance σ_{xy}^{TH} when the external $\mu_0 H$ is swept upward (blue) and downward (red).

4.2.5 Angular Dependence of Topological Hall Effect

In addition to the TH effect in the perpendicular $\mu_0 H$, we systematically studied the TH effect by rotating the sample with respect to the $\mu_0 H$, as shown in Fig. 4.14 a. We found that the chiral spin textures in the 3-5-3 sample at T = 2 K, V_g = -180 V is exceptionally stable under the tilting of the $\mu_0 H$ and the "hump" feature of the TH effect survives as the $\mu_0 H$ is tilted as much as 60º (Fig. 4.14 b to i), which is much higher than the destruction angle of the 2D skyrmion or other topological spin texture phase in the EuO film at $\theta \leq 10^{\circ}$ [110].

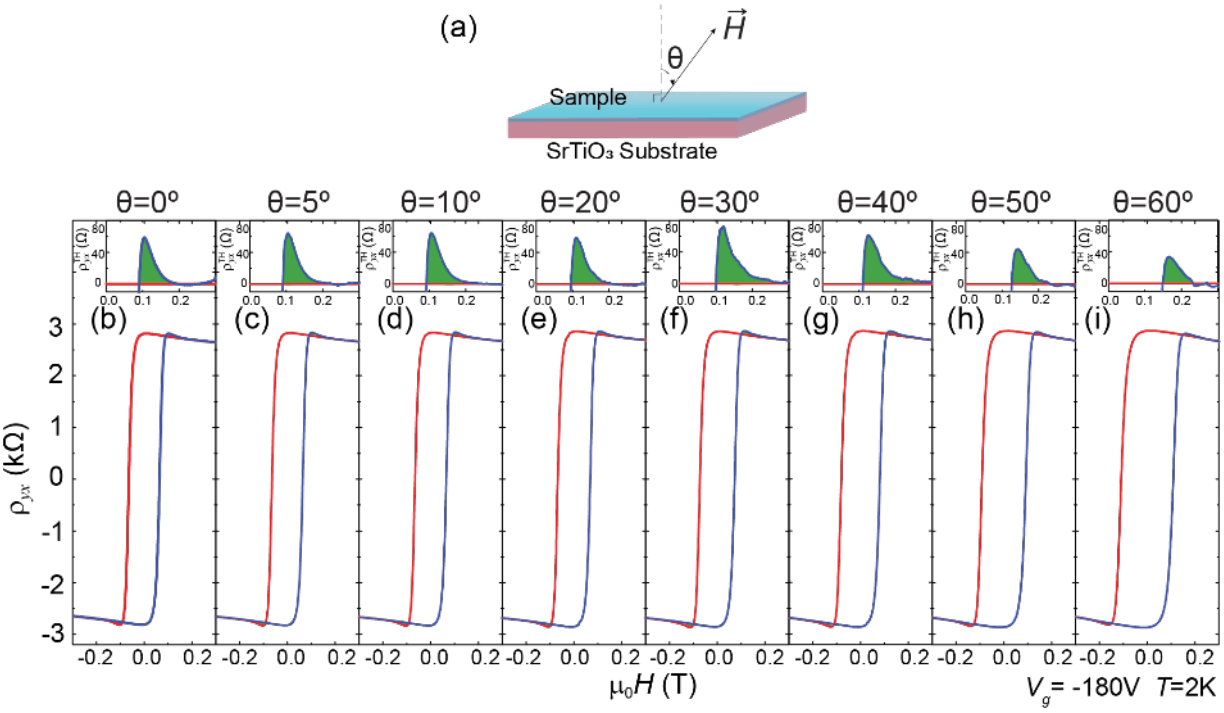

Figure 4.14 Tilt-angle dependence of TH effect for the 3-5-3 sample under V_g= -180V at T=2K. (a) Schematic showing the tilt-angle θ. The external $\mu_0 H$ is tilted at an angle θ from the normal of the film. (b-i) The ρ_{yx} of the 3-5-3 sample at the various angles of the $\mu_0 H$ inclination. (b) θ = 0º, (c) θ = 5º, (d) θ =1 0º, (e) θ = 20º, (f) θ = 30º, (g) θ = 40º, (h) θ = 50º, (i) θ = 60º. Inset of (b - i): the TH resistance ρ_{yx}^{TH} with the normal Hall and anomalous Hall contributions (ρ_{yx}^{NH} and ρ_{yx}^{AH}) subtracted. This is accomplished by subtracting the red curve from the blue curve. In the inset, the blue (red) curve represents the trace in sweeping $\mu_0 H$ upward (downward).

4.2.6 Thickness Dependence of Topological Hall Effect

As noted in Sec. 4.2.1, the balance between the exchange coupling and DM interaction in magnetic TI layers with asymmetric chemical potentials are critical for the formation of the TH effect[101]. In order to single out the appropriate sandwich heterostructure, in which the TH effect coexists with the QAH effect, we first kept the middle layer of $(Bi_{1-x}Sb_x)_2Te_3$ film to be 5 QL and systematically varied the thicknesses of the top and bottom magnetic TI layers (Fig. 4.15). We found 3 QL to be the optimal thickness for magnetic TI to realize the crossover of the QAH to TH effect. Then we kept the top and bottom Cr-doped $(Bi_{1-x}Sb_x)_2Te_3$ film to be 3 QL and fine-tuned the exchange coupling strength between two magnetic TI layers by varying the thickness of the middle undoped TI layer. We found the 3-5-3 configuration indeed shows the best QAH state at $V_g = V_g^0$ and the TH effect appears when the sample is doped by electrostatic gating (Fig. 4.15).

Figure 4.15 shows the $\mu_0 H$ dependence of the ρ_{yx} at $V_g = V_g^0$ and V_g = -200 V of the 1-5-1, 2-5-2, 3-5-3, 4-5-4 and 5-5-5 samples. The left column of Fig. 4.15 shows the ρ_{yx} at $V_g = V_g^0$. We can see that the ρ_{yx} of the 3-5-3 sample is close to the quantized value at T = 500 mK, while the ρ_{yx} of other four samples are still far away from h/e^2. The lower ρ_{yx} in 1-5-1 and 2-5-2 samples is likely due to the weak magnetization of the thinner magnetic TI layers. This can also be seen from the smaller $\mu_0 H_c$ in these two samples. For 4-5-4 and 5-5-5 samples, the lower ρ_{yx} is possibly a result of the thickness-induced dissipative channels in the heterostructures. The right column of Fig. 4.15 shows the ρ_{yx} at V_g = -200 V, where the TH effect is shown if applicable. We can see that the 3-5-3 and the 4-5-4 sample show the 'hump' feature of the TH effect. The TH component ρ^{TH}_{yx} decreases as the magnetic TI layer increases from 3 QL to 5 QL, which is due to the weakened DM interaction caused by strong exchange coupling. Therefore, the QAH and TH effects can coexist in the 3-5-3 configuration.

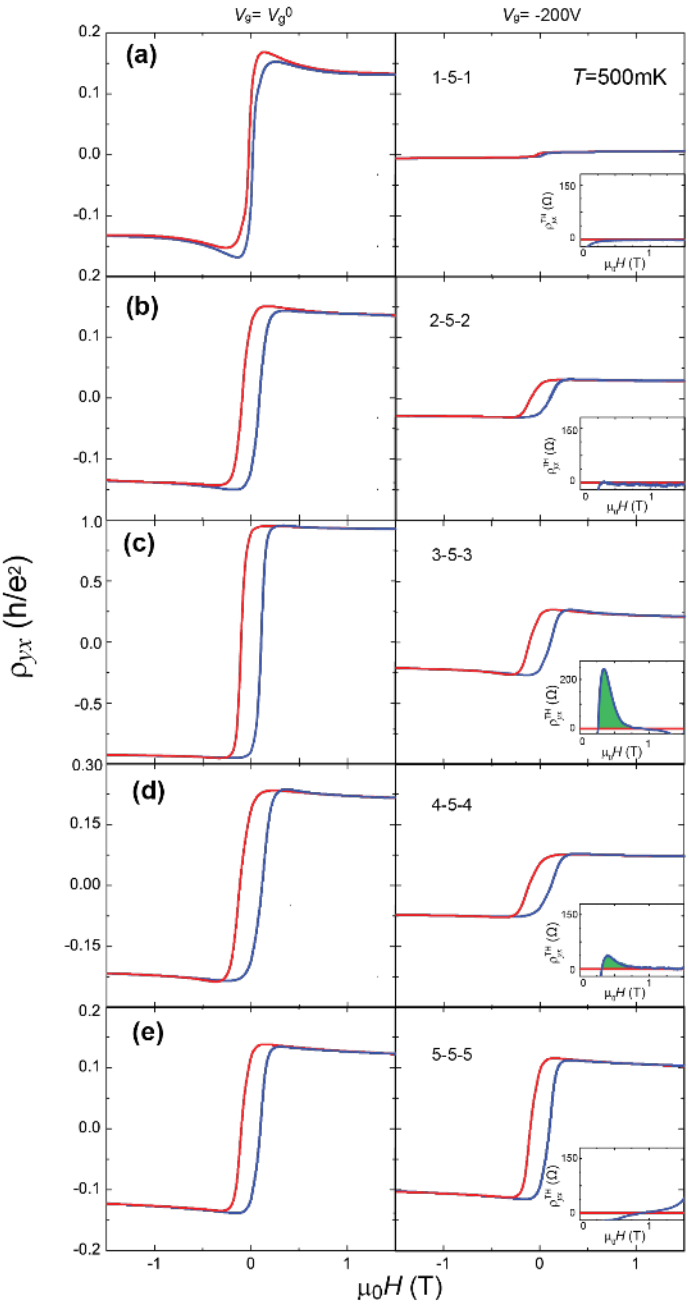

Figure 4.15 $\mu_0 H$ dependence of ρ_{yx} at $V_g = V_g^0$ and V_g = -200 V of the samples 5 QL $(Bi_{1-x}Sb_x)_2Te_3$ film sandwiched magnetic TI layers with different thicknesses at T = 500 mK. (a) 1-5-1, (b) 2-5-2, (c) 3-5-3, (d) 4-5-4, and (e) 5-5-5. Inset: the offset resistance, ρ^{TH}_{yx} at V_g = -200 V between upward (blue) and downward (red) $\mu_0 H$ sweep.

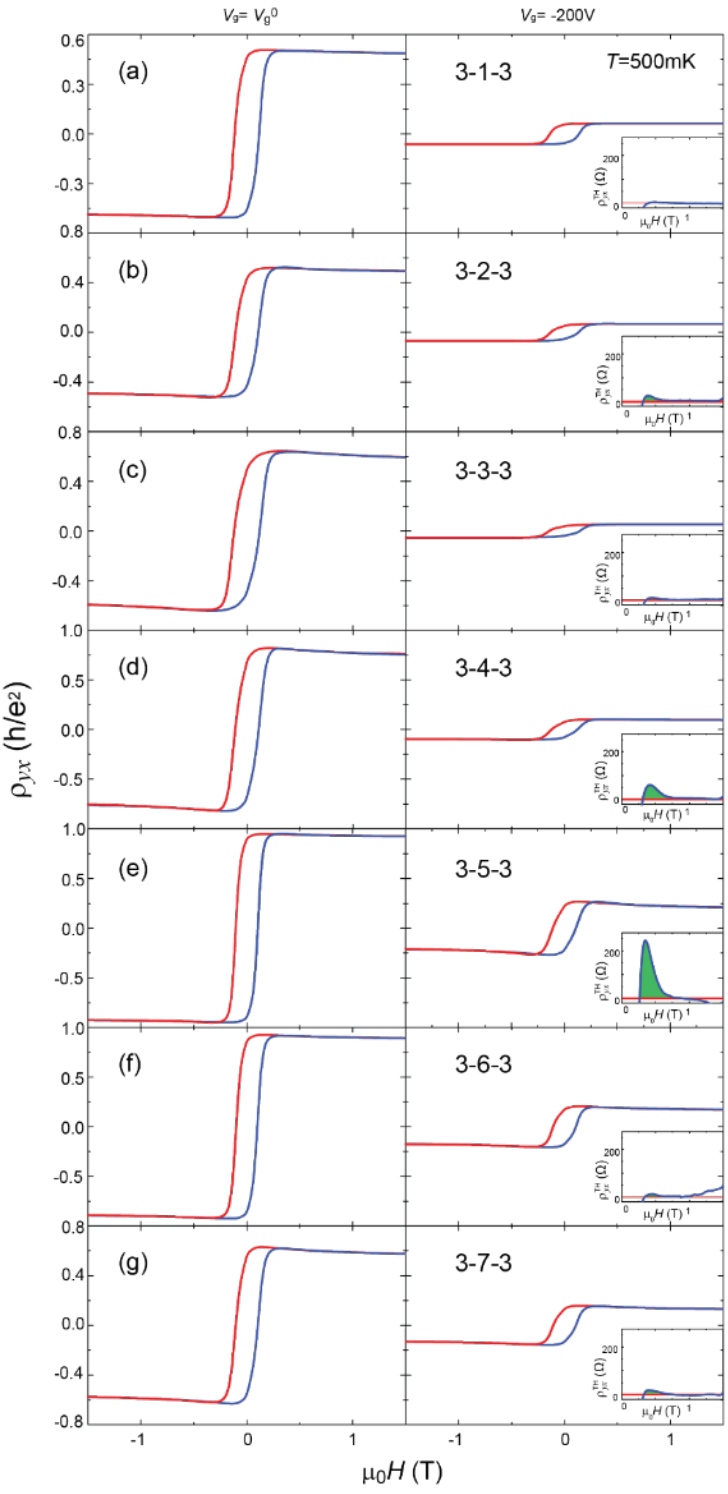

Figure 4.16 $\mu_0 H$ dependence of ρ_{yx} at $V_g = V_g^0$ and V_g = -200 V of samples top and bottom 3 QL Cr doped $(Bi_{1-x}Sb_x)_2Te_3$ layers sandwiched by undoped TI films with different thicknesses at T = 500 mK. (a) 3-1-3, (b) 3-2-

3, (c) 3-3-3, (d) 3-4-3, (e) 3-5-3, (f) 3-6-3, and (g) 3-7-3. Inset: the offset resistance, ρ^{TH}_{yx}, at V_g = - 200 V between upward (blue) and downward (red) $\mu_0 H$ sweep.

In order to optimize the thickness of the middle undoped TI layer, we kept the top and bottom Cr-doped $(Bi_{1-x}Sb_x)_2Te_3$ film to be 3 QL and systematically changed the thickness of the middle TI layer. Figure 4.16 shows the $\mu_0 H$ dependence of the ρ_{yx} at $V_g = V_g^0$ and V_g = -200 V of the 3-1-3, 3-2-3, 3-3-3, 3-4-3, 3-5-3, 3-6-3, and 3-7-3 samples at 500 mK. The left column of Fig. 4.16 shows the ρ_{yx} at $V_g = V_g^0$, and the ρ_{yx} of 3-5-3 sample is closest to the quantized value. The right column of Fig. 4.16 shows the ρ_{yx} at V_g = -200V. The 3-5-3 sample, again, shows the most pronounced TH effect. The smaller TH effect in 3-6-3 and 3-7-3 samples is possibly due to the existence of dissipative channels and weakened efficiency of the bottom gate in the thick heterostructures.

4.3 Explanation and Discussion

4.3.1 Chiral Domain Walls

In order to understand the experimental observations, we propose a physical picture based on the emergence of chiral spin textures for $\mu_0 H$ around $\mu_0 H_c$ regime. The "hump" structure in the ρ_{yx} has been observed in a variety of noncollinear magnetic systems and particularly regarded as the key signature for the chirality of skyrmions[94-97]. However, our sample has a solid ferromagnetic ground state for the occurrence of the QAH effect at low field, thus stable skyrmions are unlikely to be formed[56]. The fact that TH effect only occurs near $\mu_0 H_c$ motivates us to consider the possible spin textures during magnetization reversal. Magnetic domains with opposite polarization are nucleated and chiral walls can be formed at the domain boundaries due to the presence of the strong DM interaction (Figs. 4.17a and b). Net scalar chirality $\chi = \sum \boldsymbol{S}_1 \cdot (\boldsymbol{S}_2 \times \boldsymbol{S}_3)$ is thus non-

zero and leads to the TH effect. This is similar to the thermally-driven magnetization reversal that gives rise to the emergent chirality in the previous reports[111-113].

4.3.2 Theoretical Calculations

We start our calculation from the electronic band structure. The Hamiltonian of our magnetic TI heterostructure is consist of the surface state (SS) H_{SS} and the bulk quantum well (QW) state H_{QW}:

$$H_{ss} = v_F\left(k_y\sigma_x - k_x\sigma_y\right)\tau_z + U\tau_z + m_0\sigma_x,$$

$$H_{QW} = \varepsilon_0(\boldsymbol{k}) + N(\boldsymbol{k})\tau_z + A\left(k_y\sigma_x - k_x\sigma_y\right)\tau_x + U\tau_x$$

where the Pauli matrices σ is for spins and τ is for two orbitals, U is the asymmetric potential applied to two surfaces. $\varepsilon = C_0 + C_1k^2$ and $N = N_0 + N_2k^2$, and different sets of QW states differ by C_0 and N_0 values. Using the values $C_0 = 0.145$ eV, $C_2 = 10.0$ eV $\cdot$ Å^2, $N_0 = -0.18$ eV, $N_2 = 15.0$ eV $\cdot$ Å^2, $A = 3.0$ eV $\cdot$ Å, $m_0 = 0.005$ eV, $v_F = 3.0$ eV $\cdot$ Å, and $U = 0.02$ eV, we will have the dispersion relation in Fig. 4.17c. In the following calculation, we only consider one set of SS and QW bands for simplicity, adding more QW bands will not affect our qualitative interpretation. As we can see, the Dirac cones of SS are closer to the top QW valence band than the conduction band, which is noted as a superficial reason for asymmetric V_g - dependent ρ_{yx}^{TH} in Sec. 4.2.3.

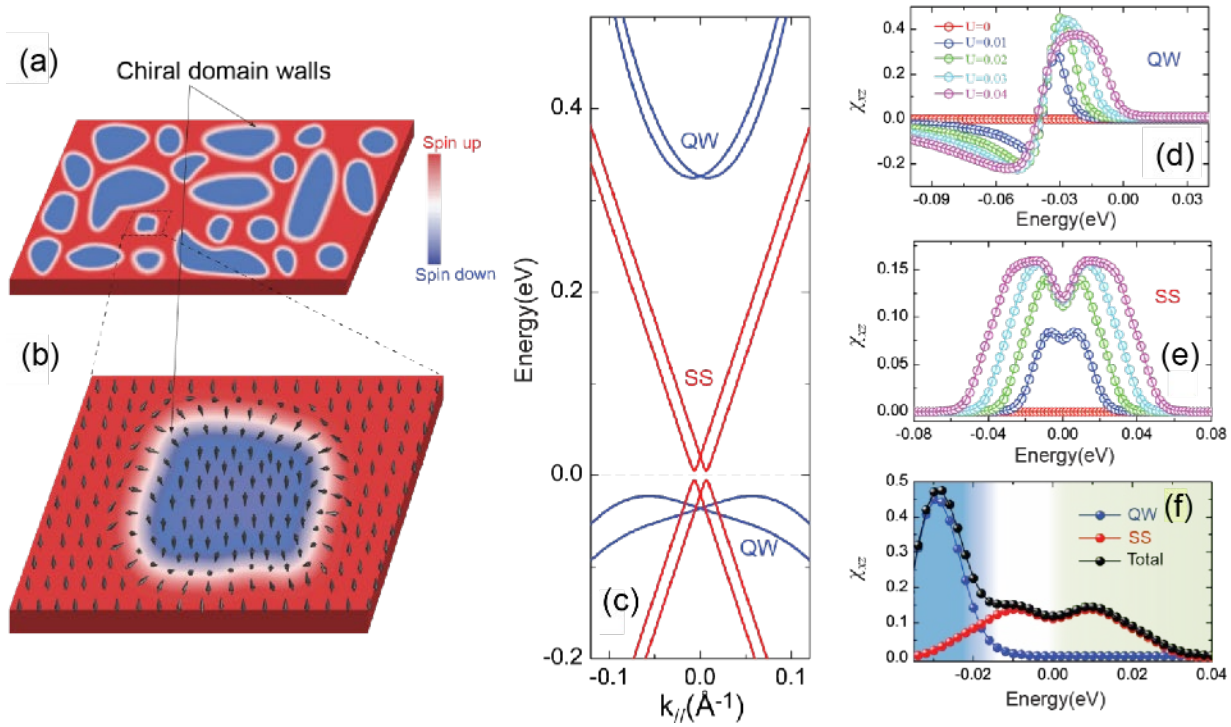

Figure 4.17 Chiral magnetic domain walls and theoretical interpretations of the crossover between the QAH and TH effects. (a) The formation of the chiral magnetic domain walls during magnetization reversals. (b) The spin distribution of the magnetic TI in a zoomed-in area in Fig. (a). (c) The energy dispersions of the SS and QW bands in the magnetic TI sandwich heterostructures. (d-e) χ_{xz} as a function of energy for the QW and SS states, respectively, under different asymmetric potentials U. (f) The QW contribution to χ_{xz}, SS contribution to χ_{xz}, and total χ_{xz} in the magnetic TI sandwich heterostructures when $U = 0.02$. $q_x = 0.005$ Å^{-1} and $q_y = 0$ in Fig. (d - f).

Since DM interaction is responsible for the formation of canting neighboring spins, the TH effect observed above can be evaluated qualitatively by investigating the DM interaction in magnetic/non-magnetic/magnetic TI sandwich systems. Since the DM interaction can be expressed as $D_\alpha(\boldsymbol{q}) = \varepsilon_{\alpha\beta\gamma}\chi_{\beta\gamma}(\boldsymbol{q})$, where ε is the Levi-Civita symbol and $\chi_{\alpha\beta}$ $(\alpha, \beta = x, y, z)$ is the spin susceptibility, we focus on the spin susceptibility to study the DM interaction.

Electrons couple to the magnetization $\boldsymbol{M}$ via Zeeman coupling, $H_{Zeeman} = -\boldsymbol{M} \cdot \boldsymbol{\Gamma}$, where $\boldsymbol{\Gamma}$ are proper 4×4 matrices for electron spin operators. For QW state electrons, $H_{Zeeman}^{QW} = -\boldsymbol{M} \cdot$

$\boldsymbol{\sigma}$, while the SS electrons respectively couple to the top magnetization $\boldsymbol{M}^t$ and the bottom $\boldsymbol{M}^b$, $H_{Zeeman}^{SS} = \boldsymbol{M}^t \cdot \boldsymbol{\sigma}(1+\tau_z)/2 + \boldsymbol{M}^b \cdot \boldsymbol{\sigma}(1-\tau_z)/2$.

The spin susceptibility $\chi_{\alpha\beta}$ $(\alpha, \beta = x, y, z)$ is evaluated for the model Hamiltonian based on linear response theory:

$$\chi_{\alpha\beta}(\boldsymbol{q}) = \frac{T}{2V}\mathrm{Tr}[G_0(\boldsymbol{q}+\boldsymbol{k}, i\omega_m)\Gamma_\alpha G_0(\boldsymbol{k}, i\omega_m)\Gamma_\beta],$$

where G_0 is the unperturbed Green's function. The spin interaction energy is:

$$E = \sum_q \chi_{ij}(\boldsymbol{q}) S^i(-\boldsymbol{q}) S^j(\boldsymbol{q}),$$

thus, the off-diagonal part of the spin susceptibility is for the DM interaction. During the magnetization reversal, the mirror symmetry with respect to the *x*-*y* plane is broken and $\chi_{xy} = 0$, so we focus on the off-diagonal components χ_{xz} and χ_{yz}. As expected from the Moriya rule[70], χ_{xz} (χ_{yz}) is linearly proportional to the momentum q_x (q_y), and $\chi_{xz}(q_y = 0) = 0$ and $\chi_{yz}(q_x = 0) = 0$, meaning the DM interaction is Neel type.

Take χ_{xz} for instance, its Fermi energy dependence with different asymmetric potentials *U* for QW states and SS are shown in Fig. 4.17d and f, respectively. The χ_{xz}- *Energy* relation for QW states displays a peak between the charge neutral point (*Energy* = 0 eV) and the SS valence band, then drop below zero when *Energy* is crossing both SS and QW valence band (< -0.03 eV). The QW conduction band (> 0.3 eV) is far above the energy range of interests, so no contribution is shown in Fig. 4.17d. χ_{xz}- *Energy* for SS displays a symmetric distribution around the charge neutral point with twin peaks, as shown in Fig. 4.17e.

Figure 4.17f demonstrates the Fermi energy dependence of total χ_{xz} when *U* is set to 0.02. It highly agrees with the experimental result of the ρ^{TH}_{yx} - (V_g -V_g^0) relation summarized in Fig.

4.11c. The -0.04 eV < *Energy* < -0.01 eV (filled by blue color) region corresponds to $V_g < V_g^0$ region in Fig. 4.11c, where the χ_{xz} displays a peak and the TH component also shows similar behavior. The -0.01 eV < *Energy* < 0 eV region (white color) corresponds to the $V_g = V_g^0$ region, however, the χ_{xz} is still non-zero, meaning the DM interaction is still able to generate the chiral spin textures. This is confirmed by non-zero TH component as the temperature increases between 100 mK and 1 K, where the thermal excitation introduces more conducting channels other than the chiral edge state from the SS or QW bands. The *Energy* > 0 eV region (green color) only has the contribution from SS band, thus the magnitude of TH component of positive V_g region is much weaker than it in the *Energy* < -0.01 eV region.

4.3.3 Discussion and Conclusion

Extra caution should be taken when we credit the chiral spin textures for the emergence of TH effect since a sign change of the AH effect could result in similar transport features. A recent paper proposed an alternative interpretation for the 'hump' features observed in $SrIrO_3/SrRuO_3/SrTiO_3$ sandwich structures[114-115]. These authors observed an opposite AH sign and different H_c between $SrRuO_3/SrTiO_3$ and $SrIrO_3/SrRuO_3$ interfaces, as displayed respectively by $R_{xy,\mathrm{I}}^{\mathrm{AH}}$ (green color) and $R_{xy,\mathrm{II}}^{\mathrm{AH}}$ (purple color) in Fig. 4.18, and the total Hall response (Orange curves in Fig. c - f) is the addition of both AH channels. During the field sweep, a higher Hall resistance is exhibited in the anti-ferromagnetic alignment region than it in the FM alignment region, and the shape of the hysteresis loop is determined by the comparative magnitude between $R_{xy,\mathrm{I}}^{\mathrm{AH}}$ and $R_{xy,\mathrm{II}}^{\mathrm{AH}}$. At T < 48K, even the total ρ_{yx} loop has a negative sign if $R_{xy,\mathrm{I}}^{\mathrm{AH}} > R_{xy,\mathrm{II}}^{\mathrm{AH}}$. Figure 4.18d - f provide reasonable explanations for all the 'hump' features observed in previous studies without resorting to the TH effect.

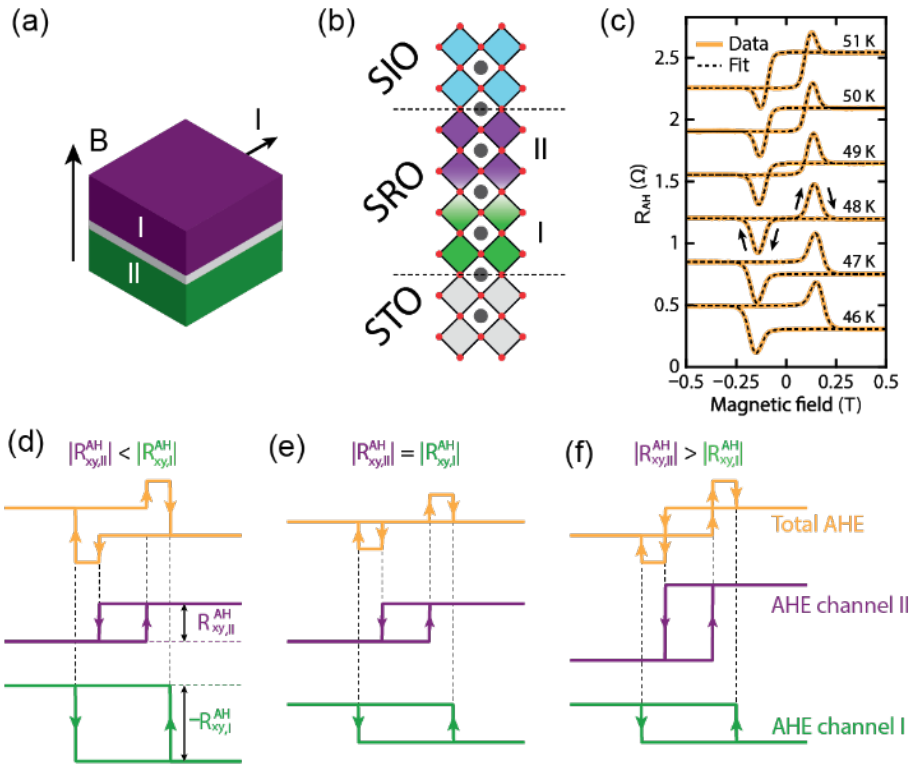

Figure 4.18 The formation of 'hump' feature in $SrIrO_3/SrRuO_3/SrTiO_3$ sandwich structures by two AH channels with opposite signs. (a) The schematic of two AH channels with opposite signs. (b) The simplified crystal structure of $SrIrO_3/SrRuO_3/SrTiO_3$ shows the exact locations for two AH channels (c) Different 'hump' features observed in the sample. (d-f) Experimental observations interpreted by the addition of $R^{\mathrm{AH}}_{xy,\mathrm{I}}$ and $R^{\mathrm{AH}}_{xy,\mathrm{II}}$. This figure is reproduced from Groenendijk, D. J., *et al*., arXiv:1810.05619, (2018).

However, this interpretation cannot be applied to our experimental results, mainly because a negative-sign AH resistance with a significantly enhanced $\mu_0 H_c$ (up to 1 T) has never been observed in a Cr-doped $(Bi_{1-x}Sb_x)_2Te_3$ samples. Also, no sign change of total ρ_{yx} is seen in our magnetic TI heterostructures at all temperature range (Fig. 4.7b). Although we are not able to manually alter the sign of AH effect in a Cr-doped TI, enhancing its $\mu_0 H_c$ is possible by coupling to a harder ferromagnet. Therefore, we carried out a control experiment to illustrate that an enhanced $\mu_0 H_c$ does not favor the formation of the 'hump' feature, and no high-$\mu_0 H_c$ component exists in our heterostructures.

In our control experiment, an additional 5 QL V-doped $(Bi_{1-x}Sb_x)_2Te_3$ ($H_c \sim 1$ T) is grown on top of the 3-5-3 heterostructure, and the top layer magnetic TI layer thus has an H_c higher than the bottom layer. Figure 4.19b-d shows the $\mu_0 H$ dependence of the ρ_{yx} of the four layers heterostructure under V_g = -50 V, 0 V, 200 V. Two distinctive ferromagnetic transitions are seen at 0.25 T and 0.08 T, representing the coercive field of the top (H_{c1}) and bottom (H_{c2}) layer. The 'plateau' feature observed when $\mu_0 H_{c1} < \mu_0 H < \mu_0 H_{c2}$ demonstrates the antiparallel magnetization alignment between the two 3 QL Cr-$(Bi_{1-x}Sb_x)_2Te_3$ layers[18], where the TH effect-like 'hump' feature disappears rather than being enhanced. The 'plateau' also indicates that the top 5 QL V-doped/3 QL Cr-doped magnetic TI layer is decoupled with the bottom 3 QL Cr-doped TI layer because of the 5 QL un-doped TI spacer. Our 3-5-3 sample with an even weaker perpendicular anisotropy in the top layer should also have a weak exchange coupling with the bottom layer. Therefore, any Hall component with an H_c (~ 0.5 T at 2 K or ~ 1 T at 30 mK) more than twice of the H_c of Cr-doped TI should be seen in the Hall loop. The absence of a second H_c makes the interpretation of sign-reversed AH resistance unlikely in our magnetic TI heterostructures.

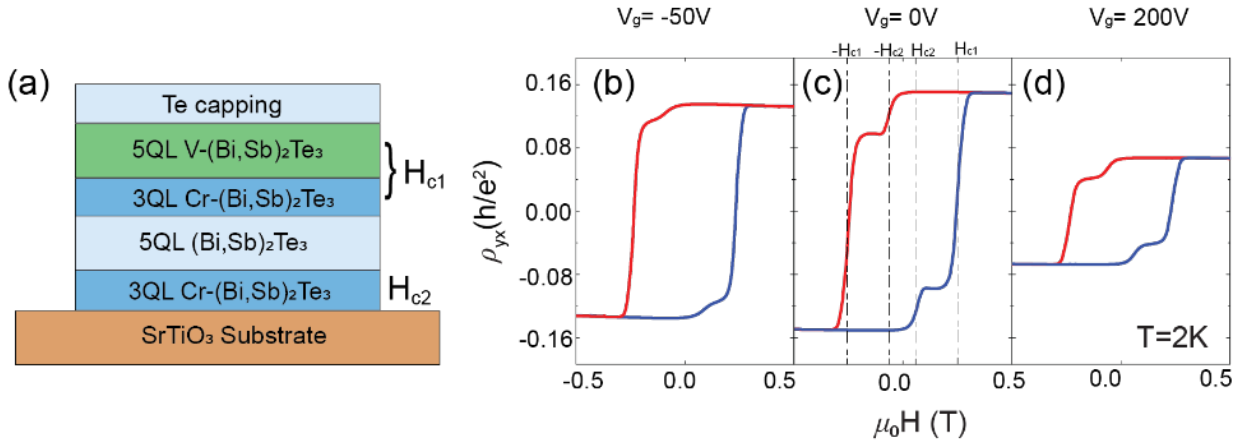

Figure 4.19 The control sample with enhanced Hc (a) Schematic of the control sample: 5 QL V-($Bi_{1-x}Sb_x)_2Te_3$ on 3-5-3 sample heterostructure. (b-d) $\mu_0 H$ dependence of the ρ_{yx} under V_g = -50 V (b), 0 V (c), 200 V (d). Because of the exchange coupling between the 5 QL V-($Bi_{1-x}Sb_x)_2Te_3$ and the top 3 QL Cr-($Bi_{1-x}Sb_x)_2Te_3$, the coercive field

($\mu_0 H_{c1}$) of the top Cr-doped TI layer increases to 0.25 T at 2 K, while the coercive field ($\mu_0 H_{c2}$) of the bottom Cr-TI stays at 0.08 T.

To summarize, we artificially fabricate a magnetic/non-magnetic/magnetic TI sandwich heterostructure that can crossover from QAH to TH effects by applying electrostatic gating voltage V_g. Systematical transport measurements at varying temperatures show the TH component is suppressed at QAH regime, and gradually increased to maximum when applying negative V_g. TH component still exists at positive V_g at a much smaller magnitude. The theoretical study calculates the DM interaction of the two surfaces with asymmetric potentials and finds that the chiral domain walls are responsible for the emergence of the TH effect. The chiral magnetic domain walls have great potential for recording the spin information [56], while the dissipation-free chiral edge states in the QAH effect can be used to transfer this information with a low-energy-cost. The marriage of the TH and QAH effect motivates further explorations of magnetic TI-based multilayer heterostructures for proof-of-concept next generation energy-efficient spintronic and electronic applications.

Part II: Long-range superconducting proximity effect in Ni nanowire

Chapter 5

Superconducting Proximity Effect in Ferromagnet

5.1 Overview of Superconductivity

Since the discovery of the superconductivity in mercury[116] by Kammerlingh Onnes back in 1911, the topic of superconductivity has been extensively and continuously investigated from both experimental and theoretical aspects due to its significant defining properties: transport of current without energy loss, and the expulsion of the magnetic field. The first widely recognized phenomenological theory[117] is proposed in 1935 by H. London, which explains the relation between the electric and magnetic field. In 1950, the Ginzburg-Landau (GL) theory[118] based on Landau's theory of second-order transition was proven to be rather intuitive and effective in describing macroscopic properties of superconductors. Soon after that in 1957, the Bardeen-Cooper-Schrieffer (BCS) theory[119] was proposed and it provided a satisfying microscopic approach to calculate theoretical quantities, such as superconducting energy gap (Δ), penetration depth (λ), superconducting coherence length (ξ), and critical field B_c (The normally used notation H_c stands for a coercive field in this dissertation).

In the past 100 years, many materials and systems were found to be able to host superconductivity and most of them can be described by the BCS theory. In 1979, a new class of superconductor[120] was uncovered in heavy-fermion system[121-122] that revolutionized people's knowledge of superconductors. Again in 1986, copper-oxide compounds (known as cuprates) were found to have a surprisingly high superconducting transition temperature (T_c) around 35 K[123], and

soon approached the boiling point of liquid nitrogen[124]. However, the mechanism of these unconventional superconductors has not yet been completely understood today. In recent years, many more unconventional superconducting systems have been revealed, such as interfacial superconductivity in 2D material[125], topological superconductors[126], graphene[127], low-carrier-density superconductivity[128-129], and high-pressure superconductivity[130]. Another interesting topic is the proximity-induced superconductivity in ferromagnets[131].

In this dissertation, we report the finding of a surprisingly long-range superconducting proximity effect found in mesoscopic ferromagnetic nanowire system.

5.1.1 Microscopic Understanding – Bardeen Cooper Schrieffer Theory

Proposed by John Bardeen, Leon Cooper, and John Robert Schrieffer in 1956, the BCS theory shows that under the sufficiently low temperature, two electrons can form a 'Cooper pair' and possess lower free energy than the normal state as long as an attractive force exists between them. In a conventional superconductor, this attraction is provided by electron-phonon interaction. The existence of a lower energy state of superconductivity starts the formation of 'Cooper pair' until the binding energy for an extra pair is decreased to zero. The paired electrons have the lowest free energy with minimum total momentum, so the two electrons have opposite but equal momenta. Here we will show below the derivation[132] of Δ and ξ according to the BCS theory.

The wave function of Cooper pair ground state is written in the form of second quantization:

$$|\varphi_G\rangle = \prod_k (u_k + v_k c_{k\uparrow}^{+} c_{-k\downarrow}^{+})|\varphi_0\rangle$$

where $c_{k\uparrow}^{+}$ is a 'creation operators' that creates a spin-up electron of momentum k, while an 'annihilation operator' $c_{k\uparrow}$ would give a 0 when act on a spin-up state with momentum k. $|\varphi_0\rangle$ is

the vacuum state without any particle. Also, $|u_k|^2 + |v_k|^2 = 1$, indicating the probability of the Cooper pair $(k\uparrow, -k\downarrow)$ being occupied is $|v_k|^2$, while its probability of being unoccupied is $1 - |v_k|^2$. The pairing Hamiltonian can be written as

$$H = \sum_{k,\sigma} \xi_k c_{k\sigma}^{+} c_{k\sigma} + \sum_{k,l} V_{kl} c_{k\uparrow}^{+} c_{-k\downarrow}^{+} c_{-l\downarrow} c_{l\uparrow}$$

where ξ_k is the energy of a single particle relative to the Fermi energy, while V_{kl} is the interaction potential. We can minimize the expectation value of the Hamiltonian at ground state by setting $\delta\langle\varphi_G|H|\varphi_G\rangle = 0$.

Since $\langle\varphi_G|\sum_{k,\sigma}\xi_k c_{k\sigma}^{+} c_{k\sigma} + \sum_{k,l} V_{kl} c_{k\uparrow}^{+} c_{-k\downarrow}^{+} c_{-l\downarrow} c_{l\uparrow}|\varphi_G\rangle = 2\sum_k \xi_k {v_k}^2 + \sum_{k,l} V_{kl} v_k v_l u_k u_l$, we can substitute v_k with $\cos\theta_k$, and u_k with $\sin\theta_k$, then we have $\frac{\partial\langle\varphi_G|H|\varphi_G\rangle}{\partial\theta_k} = 0 = -2\xi_k \sin 2\theta_k + \sum_l V_{kl} \sin 2\theta_l \cos 2\theta_k$. Therefore, we have

$$\tan 2\theta_k = \frac{\sum_l V_{kl} \sin 2\theta_l}{2\xi_k}.$$

We can then define $\Delta_k = -\frac{1}{2}\sum_l V_{kl} \sin 2\theta_l$ and $E_k = ({\Delta_k}^2 + {\xi_k}^2)^{1/2}$, which respectively represents the minimum excitation energy (energy gap) and the excitation energy of a quasi-particle with momentum $\hbar k$. With those definitions, we have

$$\tan 2\theta_k = -\frac{\Delta_k}{\xi_k},\ \sin 2\theta_k = \frac{\Delta_k}{E_k},\ \text{and } \cos 2\theta_k = -\frac{\xi_k}{E_k}.$$

Substituting $\sin 2\theta_k$ back to the definition of Δ_k leads to the condition for self-consistency, $\Delta_k = -\frac{1}{2}\sum_l V_{kl} \frac{\Delta_l}{E_l} = -\frac{1}{2}\sum_l V_{kl} \frac{\Delta_l}{({\Delta_l}^2 + {\xi_l}^2)^{1/2}}$.

With the BCS approximation that $V_{kl} = -V$ and $\Delta_k = \Delta_l = \Delta$, the self-consistency condition will become $1 = -\frac{V}{2}\sum_k \frac{1}{E_k}$.

The derivations above are done at 0 K, however, we need to translate them into a finite temperature so these quantities can be physically measured. The Fermi function that describes the probability of excitation energy E_k is $f(E_k) = (e^{\frac{E_k}{kT}} + 1)^{-1}$, thus, $\Delta_k = -\frac{1}{2}\sum_l V_{kl}\frac{\Delta_l}{E_l}[1 - 2f(E_k)] = -\frac{1}{2}\sum_l V_{kl}\frac{\Delta_l}{E_l}\tanh\frac{E_k}{2kT}$. And the self-consistency condition finally reveals the T dependence of Δ,

$$1 = -\frac{V}{2}\sum_k \frac{\tanh\frac{E_k}{2kT}}{E_k}$$

With the conditions at T_c that $\Delta(T_c) \to 0$, $E_k \to |\xi_k|$, we will reach

$$\frac{\Delta(0)}{kT_c} = 1.764,$$

in which the numerical coefficient 1.76 comes from converting the summation to the integral. This equation explicitly demonstrates that the superconductivity gap can be characterized by a measurable parameter, T_c.

The superconducting coherence length ξ_0 is another important parameter that describes the size of the Cooper pair at 0 K, i.e., the maximum distance two electrons remain coherent. Since Δ determines the range of energy for a Cooper pair, from Heisenberg uncertainty principle $\xi_0(\frac{\Delta}{v_F}) \sim \hbar$, ξ_0 can also be estimated.

5.1.2 Macroscopic Approach – Ginzburg-Landau Theory

The GL theory starts with postulating a complex order parameter $\varphi(x)$ as the wave function of superconducting electrons, so the local density of superconducting electrons is $|\varphi(x)|^2$. Assuming $\varphi(x)$ is small and varying slowly in space, we will have the free energy of superconductivity that could be expanded into the form:

$$f = f_{n0} + \alpha|\varphi|^2 + \frac{\beta}{2}|\varphi|^4 + \frac{1}{2m^*}\left|(\frac{\hbar}{i}\nabla - \frac{e^*}{c}A)\varphi\right|^2 + \frac{h^2}{8\pi},$$

where f_{n0} is the free energy of the normal state, α and β are the phenomenological parameters, m^* and e^* are effective mass and charge. In Cooper pair, we can simply set m^* to 2m and e^* to 2e. A is the magnetic vector potential and h is the effective field.

Without the presence of fields and gradients, we have

$$f - f_{n0} = \alpha|\varphi|^2 + \frac{\beta}{2}|\varphi|^4.$$

The superconducting state becomes the lowest free energy state when $\alpha < 0$ while $\beta > 0$. The minimum free energy occurs at $|\varphi|^2 = -\frac{\alpha}{\beta}$ with $f - f_{n0} = -\frac{\alpha^2}{2\beta}$.

From the free energy equation, α and β are related to the measurable quantities, T_c and B_c. When both α and β are positive, the superconducting free energy is larger than f_{n0} at any order parameter $\varphi(x)$, meaning the system is above T_c and $\alpha \propto (T - T_c)$. For correlating B_c to the free energy, we should recall that B_c is the minimum field to destroy the superconductivity, meaning the energy possessed by B_c would let the superconducting system overcome the free energy difference $f - f_{n0}$ and become normal. Therefore, the energy of the magnetic field satisfies $\frac{B_c^2}{8\pi} = f - f_{n0} = -\frac{\alpha^2}{2\beta}$.

Defining $t = \frac{T}{T_c}$, the empirical approximation gives us

$$\alpha \propto (1 - t)$$

$$\beta \propto \frac{1}{(1-t^2)^2} \approx \text{constant}\,.$$

If we use $\varphi = |\varphi| e^{i\theta}$ in the free energy equation and derive the equilibrium equation by minimizing the free energy respect to φ, we will have GL differential equation,

$$\alpha\,\varphi + \frac{\beta}{2}|\varphi|^2\varphi + \frac{1}{2m^*}\left(\frac{\hbar}{i}\nabla - \frac{e^*}{c}A\right)^2\varphi = 0\,.$$

In the absence of fields and introduce a normalized wave function $f = \frac{\varphi}{\varphi_\infty}$ (where $|\varphi_\infty|^2 = -\frac{\alpha}{\beta}$ for $\alpha < 0$ and $|\varphi_\infty|^2 = 0$ for $\alpha > 0$), we would have in 1D,

$$\frac{h^2}{2m^*|\alpha|}\frac{d^2 f}{dx^2} + f - f^3 = 0\,.$$

So, we can naturally define the temperature related characteristic length $\xi^2(T) = \frac{h^2}{2m^*|\alpha|} \propto \frac{1}{1-t}$. $\xi\,(T)$ can be shown to be expressed by ξ_0,

$$\xi\,(T) = 0.74\frac{\xi_0}{(1-t)^{\frac{1}{2}}}\,,\ \text{clean limit},\ l < \xi_0$$

$$\xi\,(T) = 0.74\frac{(\xi_0 l)^{\frac{1}{2}}}{(1-t)^{\frac{1}{2}}}\,,\ \text{dirty limit},\ l > \xi_0$$

where l is the mean free path.

From here, we have seen how the BCS theory microscopically explains the origin of superconductivity, as well as the relation between the theoretical parameters and measurable

quantities. GL theory serves as an important extension of BCS theory when dealing with the practical systems with spatial inhomogeneity.

5.2 Spin-triplet Superconductivity

The superconducting Cooper pair have minimum total momentum, meaning two electrons should have anti-symmetric wave-function. Most of the superconductors, conventional or high-T_c, have been proven to show even spatial part of the wave-function, $\varphi(r) = \varphi(-r)$, so the spin of the electrons will have opposite directions and form a spin-singlet. Its spin part of wave-function can be written as $\frac{1}{\sqrt{2}}(|\uparrow\downarrow\rangle - |\downarrow\uparrow\rangle)$ with the total spin $S = 0$ (shown in Fig. 5.1a). However, it is natural for us to assume the case of odd spatial wave-function, where we would expect a spin-triplet with $S = 1$. Its spin wave-function should have three forms: $\frac{1}{\sqrt{2}}(|\uparrow\downarrow\rangle + |\downarrow\uparrow\rangle)$, $|\uparrow\uparrow\rangle$, and $|\downarrow\downarrow\rangle$; the latter two have $S_z = \pm 1$ and are called 'equal spin'. Recently, many pieces of evidence have pointed to the existence of spin-triplet, and in this dissertation, we present our attempts to induce a possible spin-triplet superconducting pairing indicated by the long-range superconducting proximity effect in a ferromagnet.

When a superconductor is adjacent to a normal metal, the Cooper pairs can tunnel into the normal metal up to a few microns without breaking the superconducting coherence. The distance for Cooper pair could extend in the non-superconducting metal is called 'proximity range', and it is given by $\xi = \sqrt{\hbar D/k_B T}$. Here, D is the material-related electron diffusion constant, which can be calculated as one third of Fermi velocity v_F times mean free path l. However, if we replace the normal metal is a ferromagnet, the exchange coupling would force the anti-parallel alignment of a spin-singlet to the same direction, and destroy the superconducting coherence. Therefore, a spin-singlet Cooper pair is not able to survive in a ferromagnet more than a few nanometers. Its

proximity range can be expressed as $= \sqrt{\hbar D/k_B T_c}$, where T_c is the superconducting critical temperature.

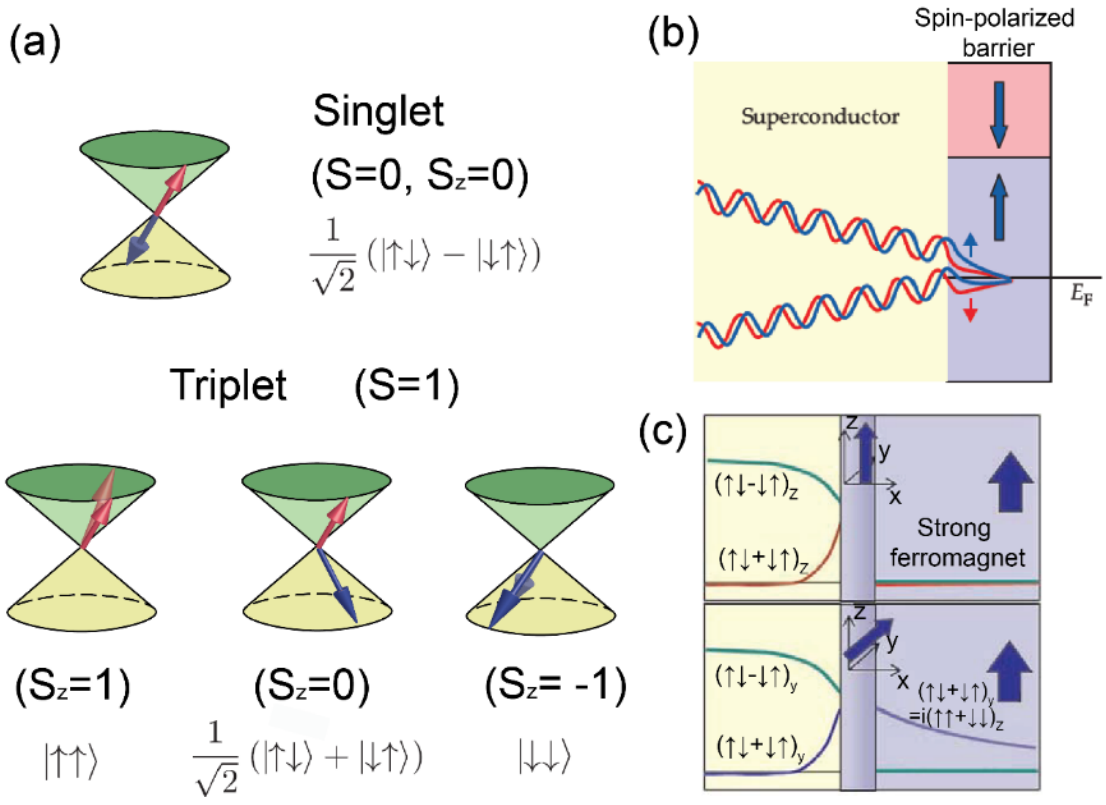

Figure 5.1 Different pairing types of superconducting Cooper pair and the creation mechanism of 'equal-spin' triplet. (a) The schematics of spin-singlet and triplet. Spin-singlet has opposite spin directions and $S = 0$, while for the spin-triplet, $S = 1$. (b) Electrons would acquire a spin direction dependent phase shift when entering a spin-polarized barrier. Blue curves indicate the wave function of spin-up electrons, while red curves represent that of spin-down electrons, so they will have a relative phase shift ϑ that gives rise to a singlet-triplet mixing state. (c) A buffer ferromagnetic layer with different magnetization direction than the strong bulk ferromagnet would create 'equal-spin' triplets that could survive in a ferromagnet. Figure (b - c) are reproduced from Eschrig, M., Physics Today, *64* (1), p.43.

However, there are observations of unusual long-range superconducting proximity effect, which will be introduced in the next section, in a ferromagnetic material that can be possibly explained by the emergence of spin-triplet. The system that facilities such observation usually

consists of an additional weak / non-collinear ferromagnetic layer that is presumably responsible for the induction of spin-triplet. Here we will briefly introduce the creation mechanism of spin-triplet[133-134].

When a spin-singlet penetrated into a ferromagnet with a spin-polarized barrier, the spin-up electron with momentum k (blue curves in Fig. 5.1b) would acquire a spin-dependent relative phase shift respective to its spin-down electron with opposite momentum $-k$ (red curves). Thus, we would have,

$$|\uparrow_k\downarrow_{-k}\rangle \rightarrow e^{i(\varphi_\uparrow-\varphi_\downarrow)}|\uparrow_{k'}\downarrow_{-k'}\rangle,\ |\downarrow_k\uparrow_{-k}\rangle \rightarrow e^{i(\varphi_\downarrow-\varphi_\uparrow)}|\downarrow_{k'}\uparrow_{-k'}\rangle.$$

Defining $\varphi_\uparrow - \varphi_\downarrow = \vartheta$, we would have the wave function of the singlet turned into a singlet-triplet mixing state:

$$|\uparrow\downarrow\rangle - |\downarrow\uparrow\rangle \rightarrow\ (|\uparrow\downarrow\rangle - |\downarrow\uparrow\rangle)\cos\vartheta + (|\uparrow\downarrow\rangle + |\downarrow\uparrow\rangle)\sin\vartheta.$$

Here the singlet-triplet mixing state is still not able to survive the exchange coupling, as shown in Fig. 5.1c. But if we have a weak / non-collinear ferromagnetic layer buffered between superconductor/ferromagnet interface that has different magnetization direction than the bulk / strong ferromagnet, the triplet component in singlet-triplet mixing state can have an 'equal-spin' projection in the magnetization direction of the strong ferromagnet. For example, in Fig. 5.1c, if the triplet component is generated in the y-axis, $(|\uparrow\downarrow\rangle + |\downarrow\uparrow\rangle)_y$, it equivalents to the combination of the 'equal-spins' respective to the z-axis:

$$(|\uparrow\downarrow\rangle + |\downarrow\uparrow\rangle)_y = i(|\uparrow\uparrow\rangle + |\downarrow\downarrow\rangle)_z,$$

therefore, the long-range superconducting proximity effect would be practical in a ferromagnet with a z-axis magnetization direction.

5.3 Previous Studies on Superconducting Proximity Effect

The first observation of spin-triplet supercurrent is reported in 2006, where authors discovered long-ranged supercurrent in the ferromagnetic half metal CrO_2 between two superconducting NbTiN electrodes[135] (Fig. 5.2a - b) with spatial separation of 310 nm. Extended work[136] showed that when a Ni/Cu layer is sandwiched between the ferromagnet and the superconductor ($Mo_{70}Ge_{30}$ is used in this work), the supercurrent can even survive more than a micrometer in CrO_2. This experiment demonstrated that the extra ferromagnetic Ni layer is playing a vital role in the induction of spin-triplet.

In 2010, two observations[137-138] of long-range superconducting proximity effect in ferromagnetic Co make people realize the importance of an additional inhomogeneous magnetization profile for generating spin-triplet between the strong ferromagnet and the superconductor. Robinson *et al*.[137] found triplet supercurrent in Co when it's sandwiched between two conical magnetic Ho layers (Figure 5.2c - e), which have magnetic moments processing in a spiral form under low temperature. Their main result displayed a rather constant characterized voltage I_cR_N in response to the increasing thickness of strongly ferromagnetic Co layer, while the I_cR_N would decrease exponentially in the absence of Ho layers (inset of Fig. 5.2e).

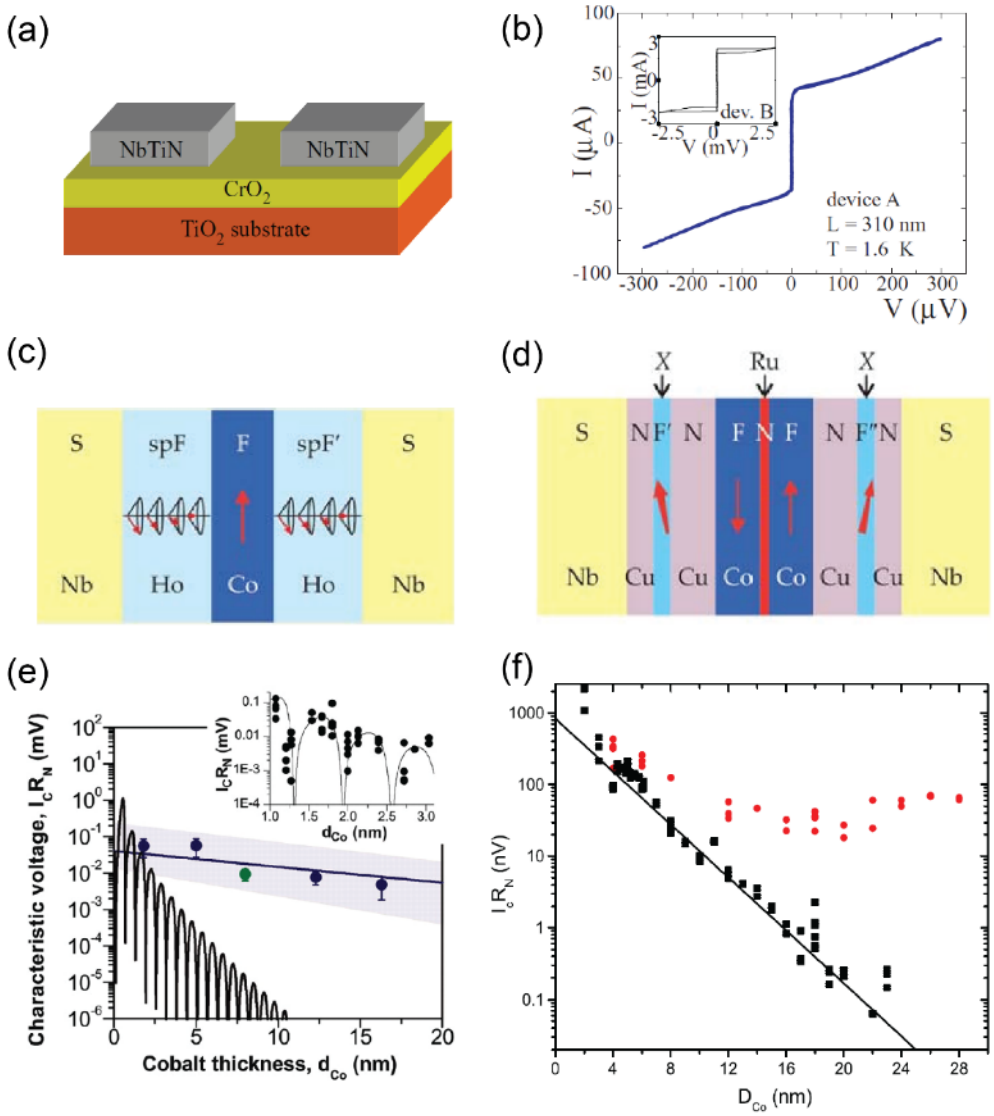

Figure 5.2 Observation of the spin-triplet pairing in mesoscopic superconducting/ferromagnetic (SF) junctions. (a) Long-ranged supercurrent is observed in the ferromagnetic half metal CrO_2 by using NbTiN electrodes. (b) I - V relation indicates a clear zero resistance supercurrent which is presumably caused by spin-triplet. (c) Schematics of the SF junction using Nb as the superconductor and Co as the ferromagnet. Ho with conical magnetization is used as the magnetic inhomogeneity to induce spin-triplet pairing. (e) I_cR_N – Co thickness relation of Nb/Ho/Co/Ho/Nb junction. Inset shows I_cR_N – Co thickness in the junctions without Ho buffer layer. (d) Schematic of SF junction using Co/Ru/Co as strong ferromagnet and Pd/Ni as a weak ferromagnetic layer F'/F". Cu buffer layers are also used to magnetically isolate those magnetic layers. (f) I_cR_N – Co thickness relation of the junction shown in Fig. (d). Red dots represent the data points acquired from the junction with F'/F" layers, while

the black dots represent the exponential drop of spin-singlet where F'/F" layers are absent. Figure (a - b) are reproduced from Keizer, R. S., *et al*., Nature, **439**, 825-827 (2006). Figure (c - d) are reproduced from Eschrig, M., Physics Today, **64** (2011). Figure (e) is reproduced from Robinson*, et al*., Science, **329**, 59-61 (2010). Figure (f) is reproduced from Khaire, T. S., *et al.,* Physical Review Letters, **104**, 137002 (2010).

Similar results are found by Khaire *et al.* [138] who used a weak ferromagnetic layer PdNi or CuNi (shown by the F' and F" in Fig. 5.2d) as the buffer layer in between Nb and Co/Ru/Co. Its I_cR_N remains constant (shown as red dots in Fig. 5.2f) when Co layer is increased to 28 nm, indicating the robustness of spin-triplet against the exchange coupling of ferromagnetism. In this experiment, authors used Co/Ru/Co structure that has anti-parallel magnetization between two Co layers, which resulted in a zero net magnetization and greatly helped in the precise measurement of I_c. Also, Cu layers are used to magnetically isolate the weak and strong magnetic layers, so the non-collinear ferromagnetic texture is possible.

Long-range superconducting proximity range can be directly measured in ferromagnetic nanowire (NW) system with superconducting electrodes. This is based on the fact that below T_c, the part of NW permeable to Cooper pair is non-resistive and would reduce the normal resistance of the ferromagnetic NW. Assuming a good uniformity of nanowire, the ratio of proximity effect range to the total length would be the same as the ratio of the superconducting resistance drop to total normal resistance. Wang *et al*.[139] observed that a ferromagnetic single-crystalline Co NW of 40 nm diameter was driven superconducting by tungsten (W) electrodes separated by 600 nm. The superconducting W electrodes deposited onto the NWs by focused ion beam (FIB) technique contain approximately 40 % atomic carbon and 20 % atomic gallium and has a T_c of 4.5 K, well above that of pure W at 12 mK. For longer Co NWs of 40nm, 80 nm diameter (1.5 μm in length), and Ni NW of 60 nm diameter (3 μm in length), the residual resistance found after the

superconducting drop in the low-temperature limit were 11 %, 50 %, and 52 % of the normal state resistance, respectively. This observation was later confirmed by Kompaniiets *et al.*[140] using superconducting W as a spin-triplet inducer, even the W is not a part of the measurement circuit. They found the proximity range is as long as 1 μm and insusceptible to magnetic fields up to 11 T. In these experiments, the W were all fabricated by FIB, so the bombarding of high-energy ions may introduce contaminations into the ferromagnet[139] and give rise to inhomogeneous ferromagnetism for spin-triplet superconductivity[141].

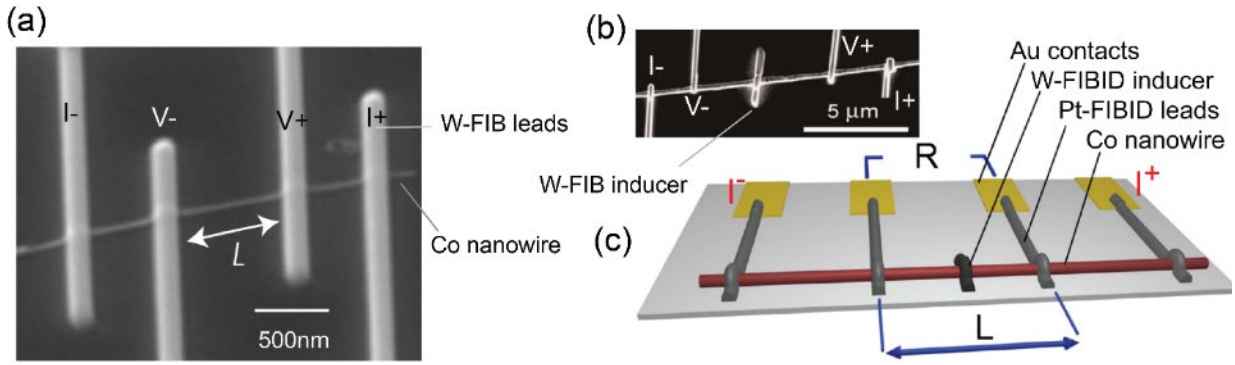

Figure 5.3 Sample configurations of the experiments observed long-range superconducting proximity effect in Co nanowire with FIB-assisted superconducting W electrodes / inducer. (a) SEM image of Co NW contacted by W electrodes and its resistance is measured by four-probe measurement. (b) SEM image of Co NW contacted by Pt electrodes; a W inducer is deposited in the middle of the NW to give rise to superconducting proximity effect. (c) Schematic of the sample configuration in figure (b). Figure (a) is reproduced from Wang*, et al*., Nature Physics, **6**, 389-394 (2010). Figure (b - c) are reproduced from Kompaniiets, *et al.,* Applied Physics Letters, 104 (2014).

Motivated by last two experiments, we would like to substitute the high-energy FIB with better-controlled deposition methods. Assisted by physical vapor deposition (PVD) and multi-step ebeam-lithograph, we reproduced the long-range proximity effect on ferromagnetic Ni NW.

Chapter 6

Sample Fabrication

6.1 Physical Vapor Deposition

Physical vapor deposition refers to several deposition methods that make the material be vaporized into atoms / molecules or plasma under ultra-high vacuum before it condenses again on top of a substrate as a uniform thin film without experiencing any chemical reaction. The most common processes for PVD are evaporation and sputtering.

Evaporation is realized by heating a solid material up to a temperature that produces a vapor pressure. In most of the cases, the solid is melted into the liquid form in an up-right crucible and the vapor will be coated onto a face-down surface on the top of the chamber (Fig. 6.1a).

Two heating methods are commonly practiced. First one is the so-called 'thermal evaporation', which is used in our experiment. It involves electrical resistive heating filaments usually made of high melting point metal like W or Mo. The W filament used in our experiments are in a shape of a 'boat', and the evaporation source is placed and melted in its concaved belly when a high current (can be as large as 100 A) is driven through the filament. Noted that Ni will form an alloy with W, so W filament boat with Al_2O_3 coating (Fig. 6.1c) is utilized when it comes to evaporating ferromagnetic Ni NW to prevent the possible damage to W filament. The other heating method is 'e-beam evaporation', where electron beams would be accelerated by a high voltage (around 10kV) in an e-beam 'gun', then hit and create a 'hot-spot' in the source. Unlike the thermal evaporation where the whole source is melted, e-beam evaporation is able to heat up only a part of the source at a particular position. This method is widely used in the deposition of high melting point metals or the materials with poor thermal conductivity like Si and ITO.

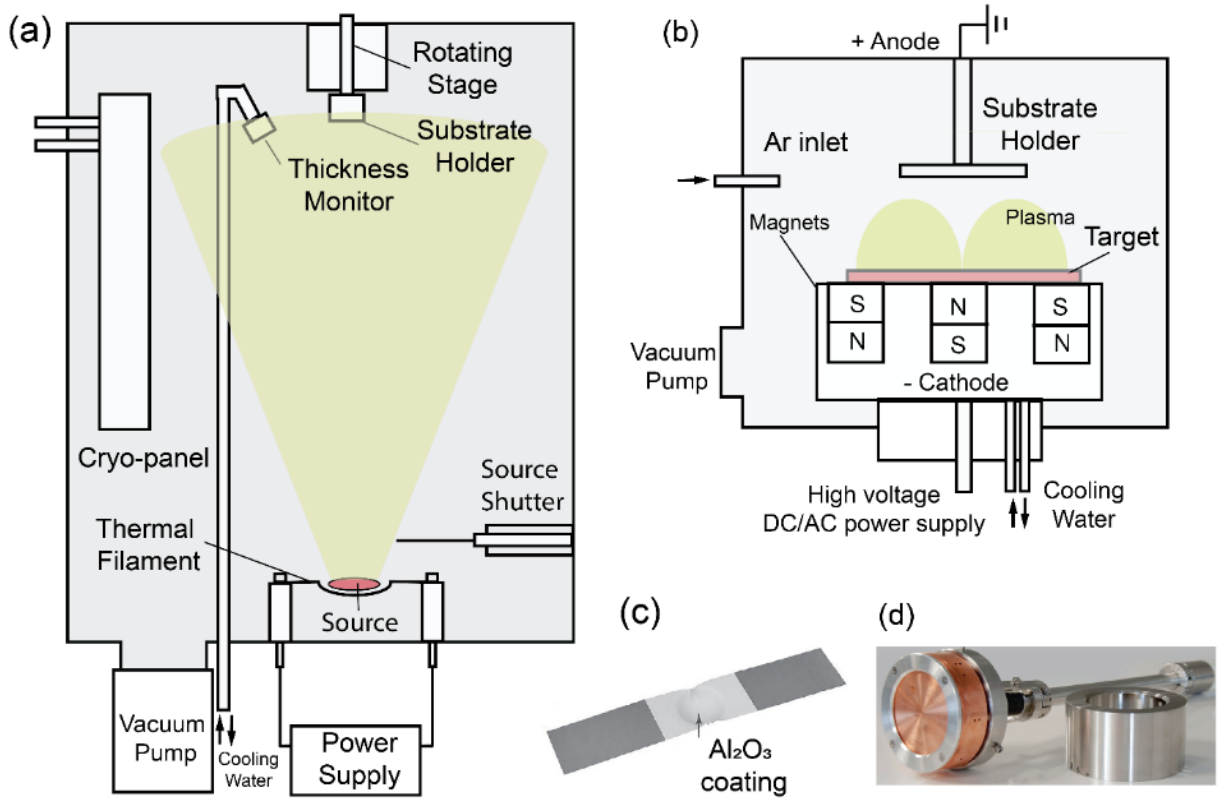

Figure 6.1 Physical vapor deposition (PVD) methods for sample growth. (a) Schematic of a thermal evaporation chamber. The evaporation source (shown in red) is melted in a W filament and the vapor will reach and condense on the face-down substrate. The process can be controlled by source shutter and monitored by the thickness monitor. A cryo-panel can be cooled by LN_2 and improve the background vacuum. (b) Schematic of a magnetron sputtering machine. The target is installed on top of a magnetron source and a high voltage will accelerate the ionized Ar atoms and bombard on the target surface. The ejected target material is trapped by the magnetic field and deposited on the substrate. (c) Image of a W filament in a shape of 'board' with Al_2O_3 coating used in our experiment. (d) Image of a magnetron gun used in the sputtering machine. Figure (c) is reproduced from https://www.lesker.com. Figure (d) is reproduced from https://moorfield.co.uk/.

Other components in an evaporation chamber are shown in Fig. 6.1a. A cryo-panel cooled by liquid nitrogen is installed to absorb impurities and improve the background vacuum level. To ensure the deposited film is of the desired thickness, a quartz crystal thickness monitor is placed at the same height of the substrate to read the real-time thickness based on its thickness-dependent

vibrating frequency. Cooling water is also employed to eliminate the influence of the temperature to the crystal vibration. Source shutter is opened when the source is fully melted for a stable deposition rate, and it will be closed to shut off the flux once the thickness reached the preset value. To improve the uniformity of the sample, we can increase the distance between the source and sample or rotate the substrate holder at a constant speed.

In the evaporator used our experiment, the power supply can host three separated sources, so different materials can be deposited consecutively without breaking the vacuum. The sample holder is ~ 1 m away from the source, and the evaporating process is carried out under the background pressure around 1×10^{-6} mbar with the deposition rate around 1-2 Å/s for Ni and Cu.

Magnetron sputtering is employed in our experiment for depositing superconducting Nb. After the chamber being pumped down to a vacuum around 10^{-7} mbar, Ar gas is injected into the chamber as the sputtering gas at the beginning of the sputtering process. Then a high voltage (DC for metallic target and AC for insulating material) will be applied on the cathode, which is a magnetron gun shown in Fig. 6.1d, so the ionized Ar would be accelerated and bombard the target (shown in red in Fig. 6.1b). The atoms of the target will thus acquire enough energy to be ejected out of the target surface and form a plasma before reaching the substrate. Strong magnets are used to confine the electrons in the plasma (as shown in Fig. 6.1b in yellow shadow), which will produce an even denser plasma and increase the deposition rate. The magnetic field will also prevent the high-energy plasma hitting the sample surface, protecting the fragile photoresists in our experiment. The anode is connected to the substrate holder and commonly grounded to the chamber during the deposition. Additionally, in our experiment, a negative voltage is often applied to the anode prior to the deposition (50 V for 50 s), so that the low energy ionized Ar can help remove the unwanted oxidation layer or organics on the sample surface.

Superconductivity of Nb film / NW is greatly influenced by its impurity level. Nb deposited in the evaporator is not able to show the superconductivity, even growing Nb in an MBE chamber at the vacuum as good as 10^{-13} mbar can dramatically decrease its T_c from ~ 8 K down to 3 K. It was discovered that only the high growth rate of (> 1 nm/s) sputtering would result in deposited Nb film with the same T_c as its bulk state. In our experiment, Nb is deposited under the background vacuum of 4×10^{-7} mbar, Ar pressure up to 4×10^{-3} mbar; The substrate is placed 10 cm away from magnetron gun and 200 V DC voltage usually gives a growth rate of 1.3 nm/s.

6.2 E-beam lithography

E-beam lithography is a process that uses scanning electron beams to draw a custom pattern in the nanometer scale. When the electron beams act on an electron-sensitive resist, the solubility of the resist would be reduced (or enhanced depending on the type of resist). After being immersed into a solvent, the region of resist scanned by the electron beam will be dissolved (or becomes harder while the rest of the area is dissolved). Followed by the deposition (or dry-etch) and lift-off process, we will have the target material in the shape of the pattern left on the substrate.

In our experiment, since the NW (ferromagnetic material Ni) and the electrodes (superconducting Nb) are different materials, we have to utilize two-step e-beam lithography. The detailed sample fabricating procedure is described below. The 0.5 mm thick Si substrates coated with 100 nm thick SiO_2 is first spin-coated with e-beam resist (Figure 6.2a). Depending on the required resolution and thickness for NW, a suitable resist will be chosen. Normally for the NW configuration, we spin coat Zep520 or bilayer PMMA (PMMA 495 A3 and PPMS 950 A3) at 6000 rpm, and bake it for 3 min at 180 ºC for hardening. Then, the pattern of NW, along with the alignment marker, will be written by the electron beam (Figure 6.2b) in lithography tool (Leica EBPG5-HR). The dose of the electron beam is carefully calibrated (~300 μC/cm^2 in our case), so

the backscattered electrons won't expand the exposure area and compromise the pattern's geometry. The resist Zep520 is normally developed in n-Amyl acetate, followed by rinsing using IPA and deionized water, while the developer for PPMA is diluted IPA (water : IPA = 1 : 3 by volume). After the development, the region radiated by e-beam will dissolve and leave us a resist mask with NW patterns. During the deposition, the vaporized materials will either condense on the e-beam resist or the bare substrate in the resist-removed region (Figure 6.2d). Once it's soaked into the lift-off solvent (acetone is usually used), the remaining e-beam resist, along with its deposited metal on top, will be washed off, and only the patterns (NW / electrodes and alignment marker) will be left on the substrate.

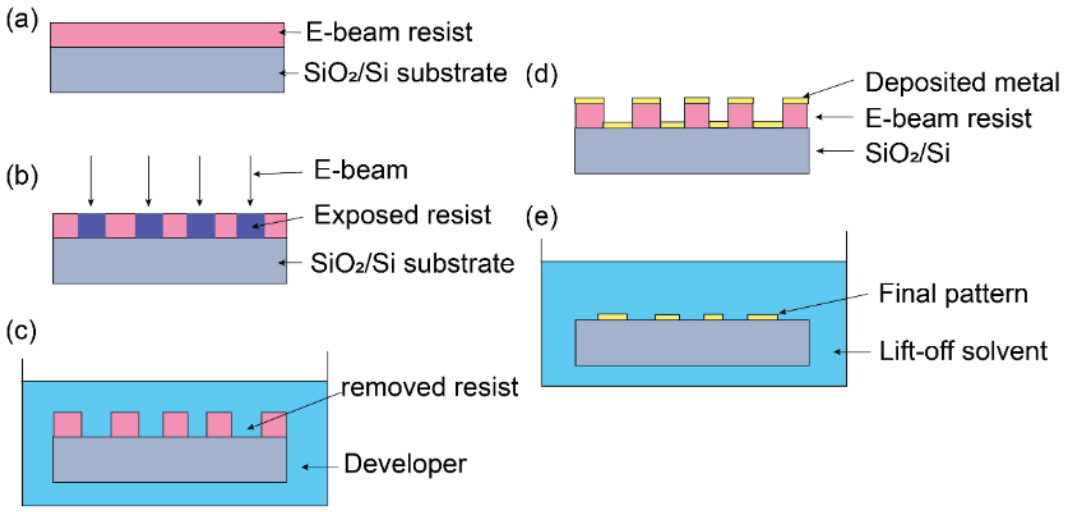

Figure 6.2 Schematics of the e-beam lithography process. (a) Spin-coating of the e-beam resist on top of SiO_2/Si substrate. (b) The solubility of the resist would be reduced (in a costume pattern, shown in blue) once scanned by electron beams. (c) Regions of exposed resist will be dissolved after being immersed into the developer. (d) During the deposition, the vaporized materials will either condense on the e-beam resist or the bare substrate in the resist-removed region. (e) The pattern is left on the substrate once it is soaked into the lift-off solvent.

Before repeating the same process to add the second material, locating the alignment marker under an optical microscope made in the previous step of lithography is indispensable.

Alignment marker is a 2D array consisting of 20 μm × 20 μm squares with 900 μm separations between each other (shown in Fig. 6.2a). It acts as a coordinate system that both NWs and electrodes have their corresponding locations. By calibrating the alignment marker to be consistent with the 'coordinate system' of the lithography tool, the electron beam can find the exact location to write the pattern for the next step, and the NW can thus be contacted by the electrodes.

6.3 Sample Configuration

The pattern fabricated for our experiment is shown in Fig. 6.3a, where the contacting leads and pads take up most of the sample in the convenience of making electrical contact (See details in Section 2.2.2) for low-temperature transport measurement. The Ni NW is fabricated along with the red leads shown in Fig. 6.3a, while the Nb electrodes are made at the same time with the blue ones. The NW configuration seen under the microscope is shown in Fig. 6.3b and the wiring method for the contact-resistance-free four-probe resistance measurement is labeled in Fig. 6.3c. Depending on the sequence of the materials' deposition, the supercurrent can flow through the ferromagnetic Ni NW either in a 'bottom-up' or 'top-down' manner. According to our results that will be presented in the next chapter, these two methods don't make any difference to our conclusion. The optional buffer layers are deposited using the same e-beam resist mask with the Nb NW, so that the supercurrent would flow through the ferromagnetic material rather than being electrically shorted by the buffer layer. In such sample configuration, the current from Nb NW will penetrate into the Ni NW within its proximity range ξ, shown in blue in Fig 6.3d. So the total resistance measured between V+ and V- leads would decrease by the percentage corresponding to the ratio of ξ to L. Giving two voltage leads that doubles the proximity effect, the superconducting proximity range can be characterized as $\xi = \frac{R_{drop}}{2R_{normal}} L$.

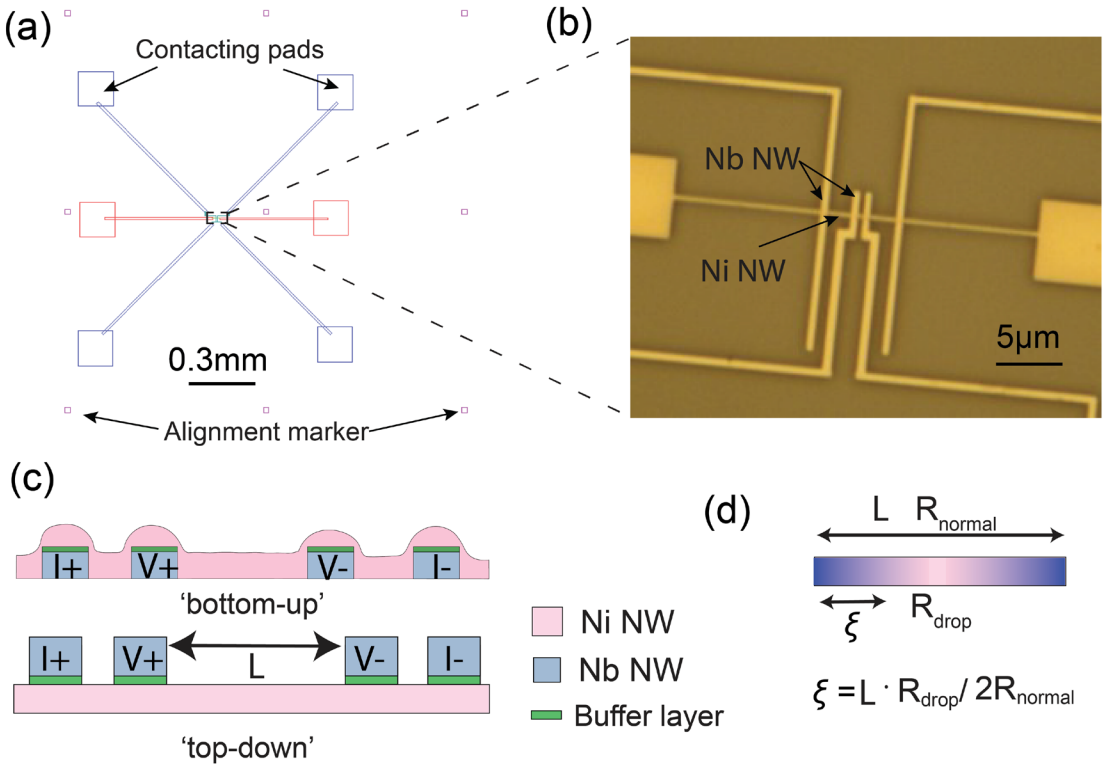

Figure 6.3 The sample configurations of nanowire structure. (a) The pattern fabricated in the lithography process. The long leads and pads are used for making electrical contacts between NWs and transport measurement system. (b) A typical image for the NW and electrodes from an optical microscope. (c) Schematics of the NW configuration in side view. The supercurrent can flow through the ferromagnetic Ni NW either in a 'bottom-up' or 'top-down' manner. (d) The superconducting proximity range can be characterized by the ratio of superconducting resistance drop to normal resistance.

Chapter 7

Long-range Superconducting Proximity Effect in Ni nanowire

7.1 Proximity Effect with Cu Buffer Layer

7.1.1 Proximity Effect without any Buffer Layer

The major drawback of the previous NW experiments[139-140] is that the deposition of the W electrodes on the Co or Ni nanowires (fabricated by electro-deposition) by the FIB process is not a well-controlled process, so the high-energy bombarding of W atoms may introduce a region of the inhomogeneous ferromagnetic area. It's natural for us first to repeat the configuration of superconducting electrodes directly contacting the ferromagnetic NW grown by PVD.

Since Co NW is often granular when fabricated by PVD, Ni is chosen as the ferromagnet in our experiment. We note that these PVD-made Ni NWs are prone to have polycrystalline structure[142]. Nb is chosen as the superconductor due to its high T_c around 8K.

We fabricated our *Sample 1* with the geometry shown in the inset of Fig. 7.1a. Ni NW is thermally evaporated in the first step of lithography, then superconducting Nb electrodes is directly sputtered on top after the second lithography. The resistance was measured by the excitation (at microampere level, 0.2 μA for *Sample 1*) that acquires optimal noise-to-signal ratio, and it has dropped only 0.8 % starting at 1.4 K (Fig. 7.1a), indicating a proximity range of 2 nm. The superconducting drop is further decreased with the application of the external field of 3 T and 6 T. Figure 7.1b shows the $\mu_0 H$ dependence of resistance shows that B_c is around the 4 T at 0.5 K, and decreases as temperature increases. The inset shows contact resistance around 0.4 kΩ from the 2-terminal measurement, indicating the ohmic contact between Ni and Nb. The superconducting drop of contact resistance also displays good quality of Nb electrode with T_c around 8 K.

The result acquired from *Sample 1* is in a good agreement with the conventional theoretical predictions[143-144]. The contact resistance indicates a comparatively good electrical contact in superconductor/ferromagnet interface. The short proximity range also indicates the established ferromagnetic order of Ni NW fabricated in our experiment.

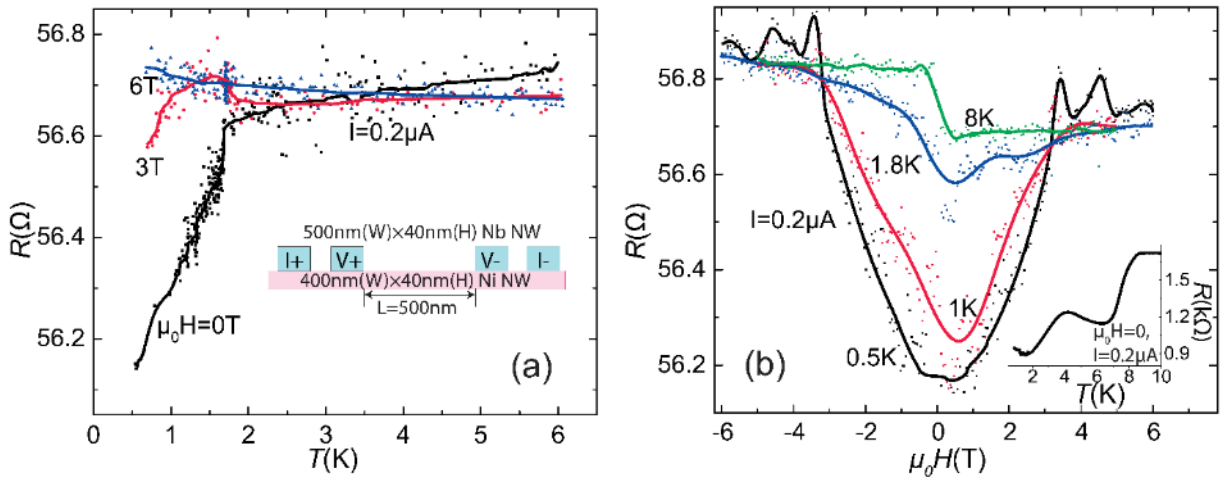

Figure 7.1 *R-T* and R-$\mu_0 H$ property of a Ni NW measured by the superconducting Nb electrodes without any buffer layer. Dots in the graphs are individual data points and the lines are the guide to the eye. (a) The resistance of *Sample 1* starts to drop at 1.5 K, and drops 0.8 % down to 0.5 K, suggesting the proximity range of superconducting singlet is 2 nm in the ferromagnet. The inset is the schematic of *Sample 1* in side view. (b) $\mu_0 H$ dependence of resistance shows decreasing B_c and resistance drop as temperature increases. The inset shows contact resistance from the 2-terminal measurement, indicating the $T_c \sim 8$ K of Nb electrodes.

7.1.2 Proximity Effect with CuNi Buffer Layer

In the previous successful observations of long-range superconducting effect, conical magnet Ho[137] or the weak ferromagnetic PdNi or CuNi layers[138] were used to provide a non-collinear magnetic profile. CuNi alloy is first applied as a buffer layer in our experiments due to its wide accessibility. We use a CuNi (55:45) alloy as the evaporation source to deposit a 1 nm

CuNi layer sandwiched between two 1 nm Cu layers, and the sample structure is shown in the inset of Fig. 7.2.

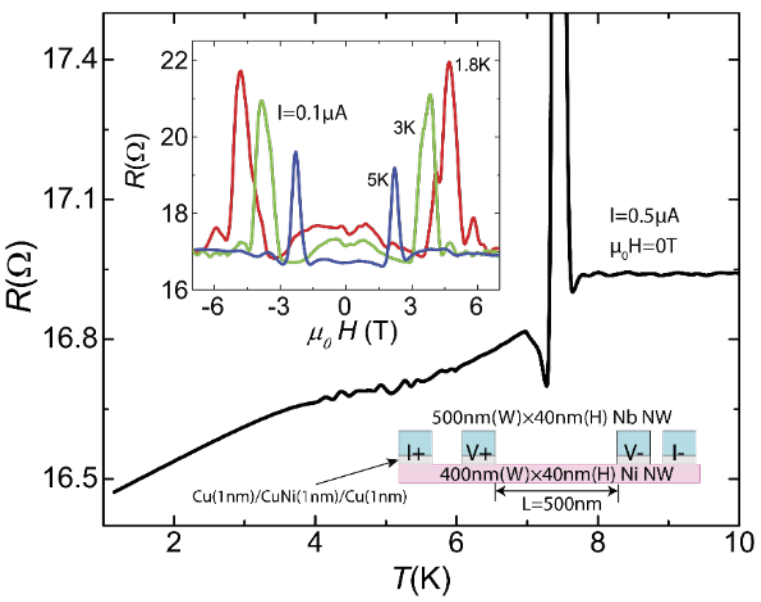

Figure 7.2 *R-T* relation of a Ni NW measured by the superconducting Nb electrodes with a Cu (1 nm)/CuNi (1 nm)/Cu (1 nm) buffer layer. The superconducting drop of *Sample 2* indicates a proximity range of 8 nm. The inset on the upper left is R-H relation and the one at the right corner is the schematic of *Sample 2* in side view.

Sample 2 shows the largest superconducting drop (*R-T* curve in Fig. 7.2) among all the samples with the same structure, indicating a superconducting proximity range of 8 nm. The *R-T* relation of *Sample 2* displays a 'critical peak' appears around 7.5 K and the R - $\mu_0 H$ relations (inset of Fig. 7.2) are also dominated by the influence of the giant 'critical peaks'. The 'critical peak' feature is commonly seen in a superconductor-ferromagnet heterostructure, however, its origin still remains debatable. The absence of the long-range proximity effect in this structure is possibly due to the large ferromagnetic exchange coupling of Ni NW, which aligns the magnetization of CuNi layer to the same direction, so a non-collinear magnetic region is failed to be established.

(a) Long-range Proximity Effect with Cu Buffer Layer

A practical way to isolate the influence of strong ferromagnetic material is increasing the thickness of the Cu layer[138, 145]. Before conducting further study on the weak ferromagnetic buffer

layer, we have to first identify the influence of Cu buffer to the superconducting proximity effect. Strikingly, we find that by simply adding a thin Cu buffer layer with natural oxidation between SF interfaces, an unusual long-range superconducting proximity effect emerges. In this section, we will present three ferromagnetic Ni NWs with 3 nm Cu buffer layer, *Sample 3* to *Sample 5*, exhibiting superconducting proximity effect with spatial extent ranging from 35 nm to 136 nm. In our experiment, materials with different functionality were deposited separately to guarantee the clean interfaces and minimum intermixing, so Cu layer was exposed to air before the deposition of the next structure. And we will show later that the oxidized Cu is playing a vital role in the long-range proximity effect.

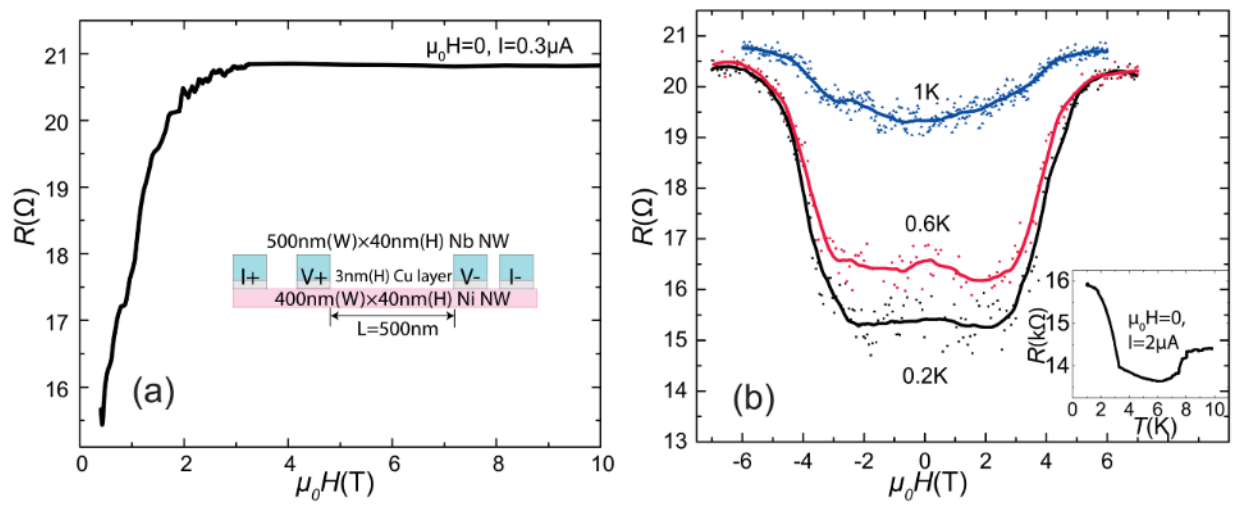

Figure 7.3 *R-T* and R-μ0*H* property of a Ni nanowire measured by the superconducting Nb electrodes with a Cu buffer layer. (a) The resistance of *Sample 3* starts to drop at 3 K, and drops 25 % down to 0.2 K, suggesting a superconducting proximity range of 65 nm in Ni NW. The inset is the schematic of *Sample 3* in side view. (b) R-μ0*H* relation shows decreasing B_c and resistance drop as temperature increases, the dots in the graph are individual data points and the lines are the guide to the eye. The inset shows contact resistance from the 2-terminal measurement, indicating the Tc ~ 8 K of Nb electrodes. A resistive upturn shows up under 3 K.

Sample 3 is also a 'top-down' configuration with Ni NW deposited prior to the 3 nm Cu buffer layer and Nb electrodes. As shown in Fig. 7.3a, the resistance of *Sample 3* has dropped 30 % from 3 K to 0.2 K, indicating a superconducting proximity range of 65 nm. Magnetoresistance displays consistent superconducting-normal state transition with decreasing B_c and R_{drop} as temperature rises in Fig. 7.3b. Its inset shows the contact resistance acquired by two-probe measurement, where the superconducting transition of Nb electrodes is clearly demonstrated around 8 K, as well as an increase at 3 K. It is due to the bad thermal conductivity when Ni is induced superconducting, so the heat accumulated around contact is unable to dissipate through the substrate and cause the resistance to increase.

Figure 5.10 suggests a superconducting proximity range of 35 nm for *Sample 4*, and Figure 5.10c shows an even longer range of 136 nm for *Sample 5*. Closed to T_c of Nb electrodes (see Fig. 5.10 (b) & (d), insets), R_{drop} of Ni NW in these two samples start to emerge from 8 K, and gradually vanishes with the applications of the external magnetic field. *Sample 4&5* have more robust superconducting coherence than *Sample 3* due to their higher T_c, which can also be seen from their larger critical current (I_c) (shown in Fig. 7.5a - c). Resistance peaks near T_c or B_c can also be observed, although the origin of which still remains as an open question[139]. The magnitude of normal resistance of *Sample 4* is dramatically larger than other devices, indicating a comparatively larger strength of scattering in its Ni NW. This can also be seen in the *R-T* relation in the normal state (Figure. 7.5d), where *Sample 4* shows a slightly insulating behavior while others show the all-range metallic property, coinciding with the fact that the superconducting proximity range of *Sample 4* is the smallest among all three samples.

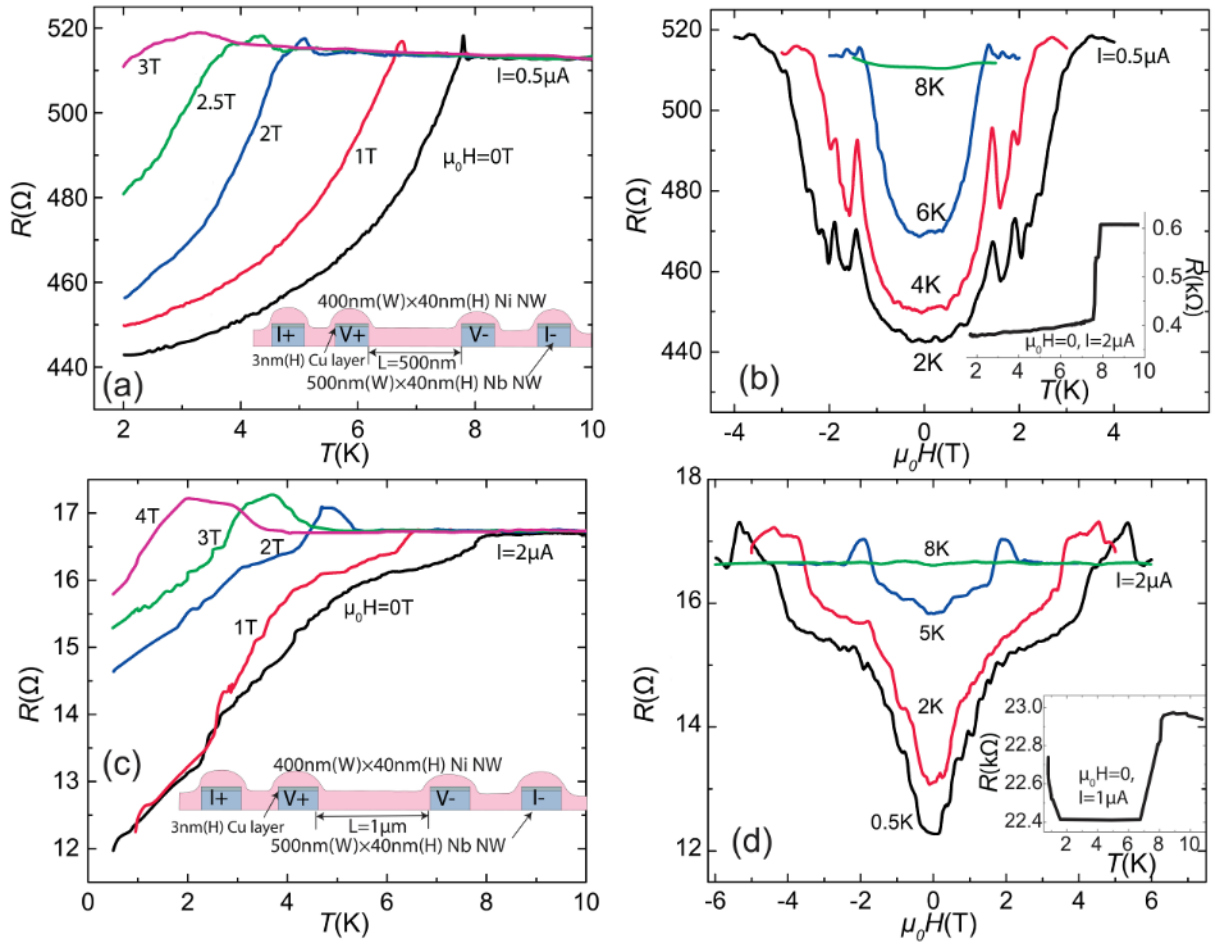

Figure 7.4 *R-T* and *R-μ₀H* property of two Ni nanowires deposited on Cu/Nb electrodes. (a) *R-T* curve of *Sample 4* suggests a superconducting proximity range of 35 nm with Tc ~ 8 K at zero field. The resistance drop gradually vanishes with the application of *H*. The inset is the schematic of *Sample 4* in side view. (b) R-$\mu_0 H$ curve of *Sample 4* shows $B_c \sim 4$ T at 2 K. B_c and the amount of resistance drop decrease as temperature increases. The inset shows contact resistance from the 2-terminal measurement. (c) *R-T* graph of *Sample 5* suggests a proximity range of 136nm with $T_c \sim 8$ K at $H = 0$ and decreases with the application of *H*. The inset is the schematic of *Sample 5* in side view. (d) *R*-$\mu_0 H$ curve of *Sample 5* shows $B_c \sim 6$ T at 0.5 K, and $B_c \sim 4$ T at 2 K. B_c and the amount of resistance drop decrease as the temperature increases. The inset shows contact resistance from the 2-terminal measurement.

We noticed a repeatable quasiperiodic oscillation superimposed on background magnetoresistance (Fig. 7.4b and d) of both samples. These oscillations are likely to be the vortex

crossing in the proximity-induced superconducting region. Similar oscillation is reported in the type-II superconductor, $NbSe_2$[146].

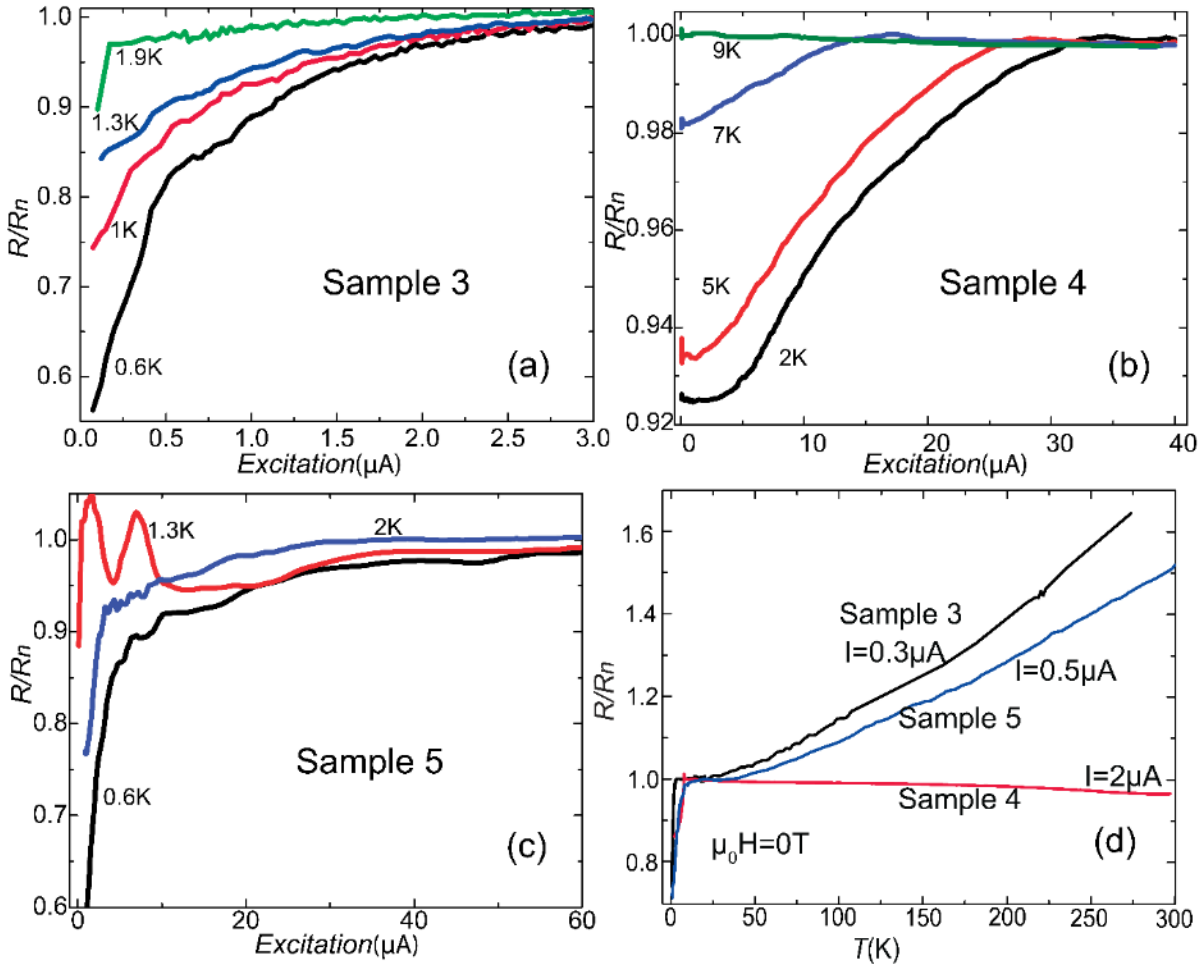

Figure 7.5 Normalized resistance v.s. current relation under different temperatures of (a) *Sample 3,* (b) *Sample 4,* and (c) *Sample 5*. The superconducting proximity effect is gradually diminishing as the excitation or temperature increases, indicated by the decreasing resistance drop of ferromagnetic Ni NW. (d) Normalized resistance-*T* relation of three samples.

7.1.3 Proximity Effect with Au Buffer Layer

To check the influence of a normal-metal buffer layer to superconducting proximity effect, we substitute Cu with thermally evaporated Au in *Sample 6*. We also tried to short Ni wire by covering it with thick Au (6 nm) layer in *Sample 7*. Au layer of *Sample 6* shared the same mask of Nb electrodes, while in *Sample 7*, 6 nm Au was thermally deposited on the same mask of Ni NW.

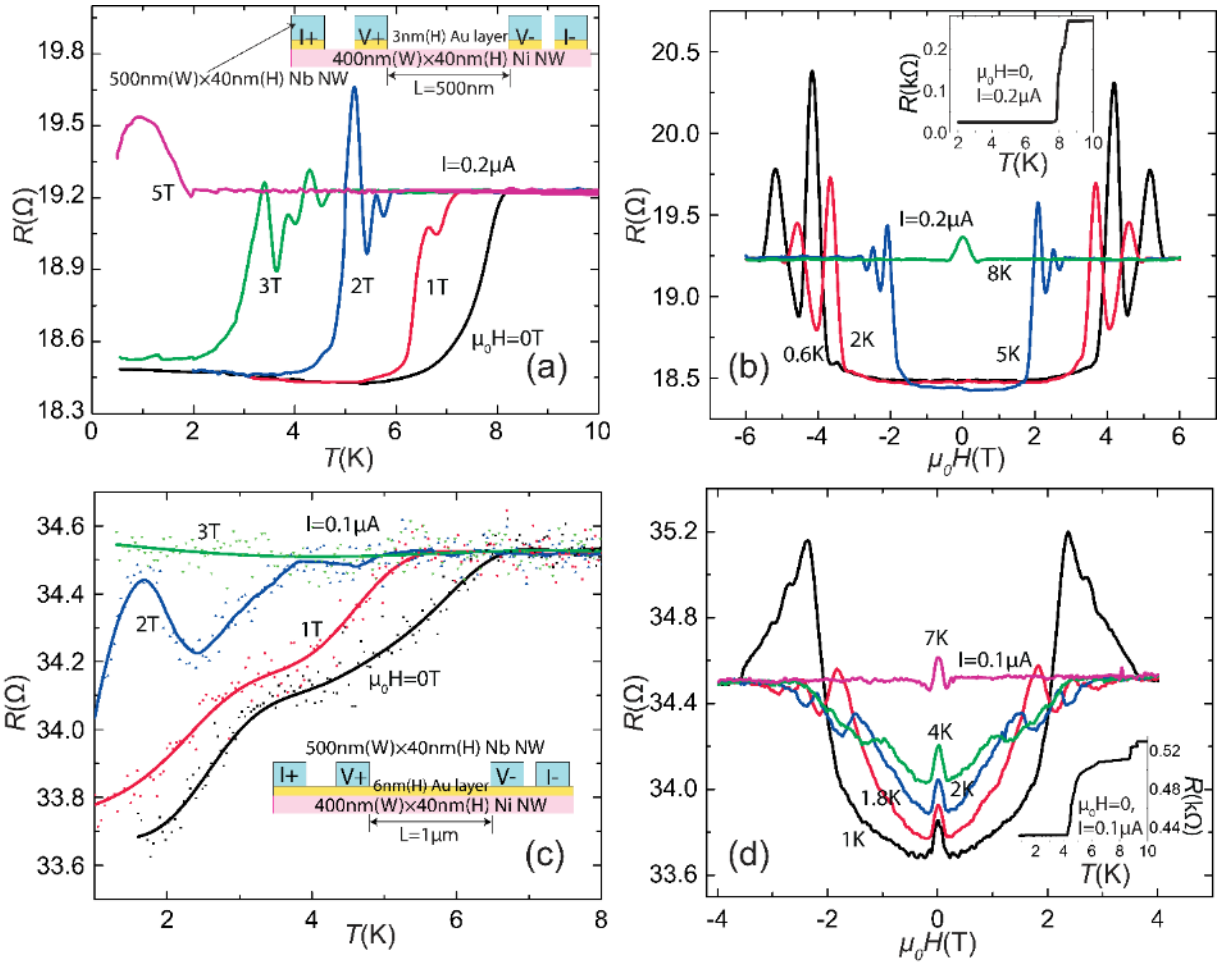

Figure 7.6 *R-T* and *R*-μ0*H* property of a Ni NW measured by the superconducting Nb electrodes with Au interlayer. (a) *R-T* graph of *Sample 6*. The inset is the schematic of *Sample 6* in side view. (b) *R*-μ0*H* of *Sample 6*. The inset shows contact resistance from the 2-terminal measurement. (c) *R-T* graph of *Sample 7*. The inset is the

schematic of *sample 7* in side view, where the Au layer has covered the whole Ni wire. (d) *R*-$\mu_0 H$ of *Sample 7*. The inset shows contact resistance from the 2-terminal measurement.

Interestingly, both samples show a resistance drop indicating maximum proximity range around 10 nm and giant 'critical peaks' in magnetoresistance, as shown in Fig. 7.6. In *Sample 6*, *R*-*T* relation also shows increased resistance with several 'critical peaks' around Tc, and the resistance flattened quickly with decreasing temperature. Sharp superconducting drops are also presenting around Hc in *R*-$\mu_0 H$ relation graph. While in most of our samples, resistance is dropping gradually and showing the trend of further drop at the cryostat's base temperature. *R*-$\mu_0 H$ relation of *Sample 7* has large and wide 'critical peaks' starting from 4 T to 2 T at 1 K. Interestingly, small peaks also emerge around the low field from 1 K to 7 K, and the reason remains unknown for us.

These results do demonstrate an enhanced superconducting proximity effect in the ferromagnetic wire when using Au buffer layer, although not as strong as it with Cu. It also indicates that the Ni NWs we are studying have strong ferromagnetism that has prevented Au layer from being driven fully superconducting[147-148].

7.2 Possible Explanation of Long-range Proximity Effect in Ni

7.2.1 Possible Noncollinear Magnetic Profile Induced by CuO

We listed all the nanowire samples presented in this dissertation in Table 7.1 for a clear comparison in an attempt to understand the particularly long-range proximity effect found in samples inserted with thin layers of Cu.

No.	Geometry L(nm)	Ni fabrication method	Interlayer(nm) /Method	CuO presents?	Supercurrent direction	Contact resistance (Ohm)	Proximity range in Ni(nm)
1	500	Evaporation	N/A	No	Top-down	800	2
2	500	Evaporation	Cu(1)/CuNi(1)/Cu(1) /evaporation	Yes	Top-down	100	8
3	500	Evaporation	Cu(3)/evaporation	Yes	Top-down	13,000	60
4	500	Sputtering	Cu(3)/sputtering	Yes	Bottom-up	265	35
5	1000	Sputtering	Cu(3)/sputtering	Yes	Bottom-up	22,400	136
6	500	Evaporation	Au(3)/Evaporation	No	Top-down	<1	10
7	1000	Evaporation	Au(6)/Evaporation	No	Top-down	<1	10(Au/Ni NW)
8	500	Sputtering	Cu(3)/sputtering	Minimal	Top-down	200	13
9	500	Sputtering	Cu(10)/sputtering	Minimal	Top-down	5	2
10	500	Sputtering	Cu(10)/sputtering	Yes	Bottom-up	300	<1

Table 7.1 Summary of NW structure and properties presented in this dissertation. *Sample 1* has no buffer layer and it shows superconducting proximity range consistent with conventional theory. *Sample 2, Sample 6, and Sample 7* are showing a similar level of proximity range, indicating a slight enhancement due to the buffer layer. *Sample 3* to *Sample 5* display surprising long-range proximity effect when a naturally oxidized thin Cu layer is acting as the buffer layer. *Sample 8* to *Sample 10* will be presented in the next section to show that proximity range dramatically decreases if we reduce the amount of CuO or the magnitude of its magnetism.

The first candidate is the formation of CuNi alloy at Cu/Ni interface. It has been reported to provide noncollinear magnetic texture[138] predicted to induce spin-triplet[149-150]. However, the 8 nm proximity range from *Sample 2* indicates the negligible influence of CuNi layer to the triplet supercurrent induction. Other candidates lie on the oxidations formed during the fabrication,

namely, CuO[151] and NiO, which are antiferromagnetic[152] materials that could serve as the magnetic inhomogeneity. NiO can be ruled out by *Sample 4&5*, whose NiO is absent in the interface while the long-range proximity effect still emerges; And in *Sample 1*, NiO is possibly presented, but only 2 nm of proximity range is detected. Thus, CuO becomes the most likely origin for inducing long-range proximity effect. CuO could be formed in the atmosphere from thermally evaporated Cu[153], it was shown that such CuO a film often displays anti-ferromagnetism properties with Neel temperature around 230 K[154]. Nano-sized CuO particles could even display ferromagnetism due to short-range low-dimensional anti-ferromagnetic elements[153]. Enhanced coercivity and remanence were also observed under low temperature by Karthik, *et al*.[155] The CuO layer that formed between Cu and Ni layer in our sample could be the reason for the formation of spin-triplet cooper pairs that survive a long range in ferromagnetic Ni nanowire.

7.2.2 Experimental Evidence of Magnetic CuO

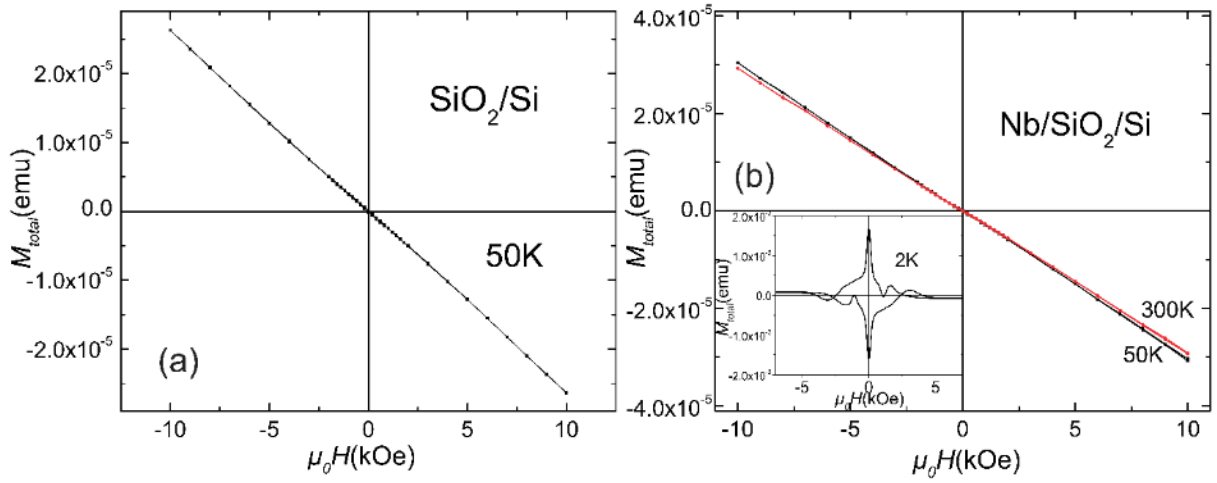

Figure 7.7 *M-H* relation of controlled samples. (a) M-H curve of a 4 μm × 4 μm Si substrate with 500 nm SiO2 on the surface. (b) M-H relation of a 40 nm Nb sputtered on the substrate. The inset shows the *M-H* curve of the sample under 2 K. No ferromagnetic impurity is found by the SQUID measurement.

To test the magnetic properties of the Cu layer in our NW, we carried out magnetization measurement using Superconducting Quantum Interference Device (SQUID) by Quantum Design, Inc. As shown in Fig.7.7, the substrate (4 μm × 4 μm SiO_2 (500 nm)/Si (500 μm)) has a linear M-H relation with the negative slope at 50 K, and the one with 40 nm Nb on top presents similar diamagnetic behavior. These results are reasonable since Si/SiO_2 are mostly showing the diamagnetic property if it's not contaminated by ferromagnetic material; And the Nb is paramagnetic when it's above T_c. Both diamagnetism and paramagnetism are giving a linear magnetic response, thus we can detect the ferromagnetic behavior of our sample when subtracting the linear M-H relation of the substrate. The inset of Fig. 7.7b displays superconducting behavior of Nb under 2 K.

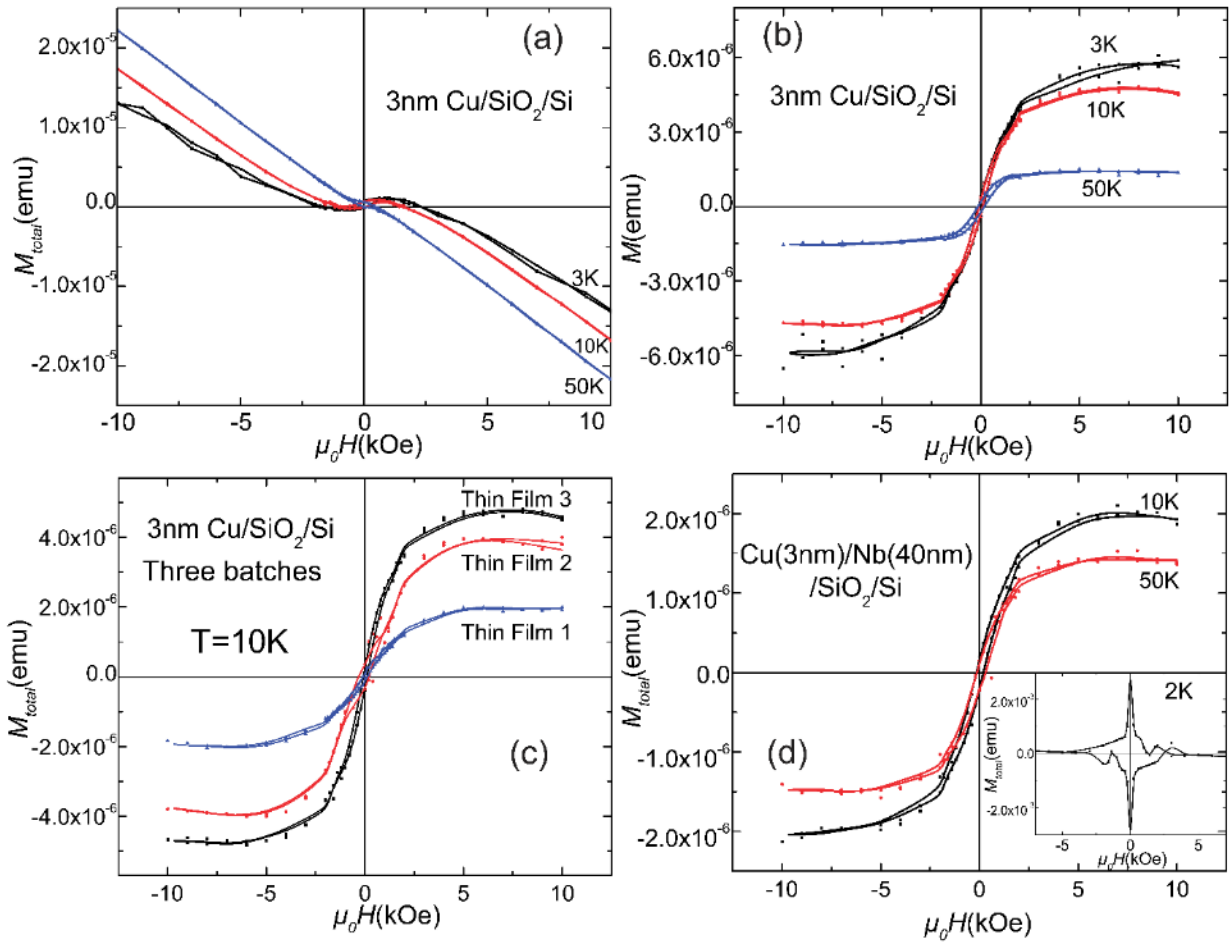

Figure 7.8 *M-H* relation of 3nm naturally oxidized Cu evaporated on 4 μm × 4 μm SiO_2/Si Substrate with / without 40 nm Nb layer. (a) Raw Data acquired from the sample. (b) *M-H* relation of 3 nm naturally oxidized Cu layer with background subtraction. (c) A number of such Cu films from different batches were tested, similar M-H relations were found. Thin Film 1 is the film shown in Fig. (a) and (b). (d) *M-H* relation of 3 nm naturally oxidized Cu layer on top of 40 nm Nb. Inset shows the diamagnetism of superconductivity.

Figure 7.8 shows the ferromagnetic behavior of naturally oxidized Cu (3 nm) on the substrate. If we subtract the linear diamagnetic background out of the raw data, we found evidence of ferromagnetism in Fig. 7.8b. It presents a hysteresis loop with the coercive field around 200 Oe, and the saturation field more than 2 kOe under 50 K. The total magnetization increases as temperature decreases due to enhanced magnetic anisotropy. To ensure the repeatability of the

ferromagnetism, we deposited such Cu film several times, and the samples from all batches are showing similar result under 10K (Fig. 7.8c). Similar *M-H* is also obtained when a 40 nm Nb layer is deposited prior to the Cu layer (Fig. 7.8 d).

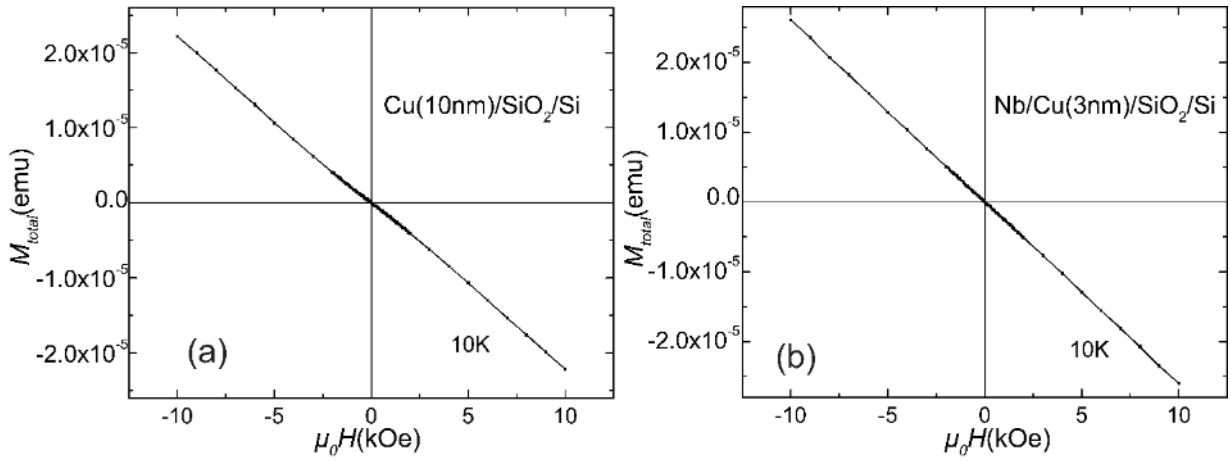

Figure 7.9 *M-H* relation in thicker Cu layer or thin Cu layer with minimum exposure to atmosphere. (a) *M-H* relation of 10 nm naturally oxidized 10nm Cu evaporated on a 4 μm × 4 μm Si substrate with 500 nm SiO_2. Cu and Nb are deposited without breaking the vacuum. (b) *M-H* relation of 3 nm Cu layer covered by a 40 nm Nb layer grown on the Si substrate. Ferromagnetism vanished in these two cases, indicating the anti-ferromagnetism of CuO.

The naturally oxidized thin (3 nm) Cu layer in our system has found to show an anomalous ferromagnetic behavior, which agrees with the ferromagnetic response of reported CuO nanostructures[153, 155-157]. In those CuO nanostructures, anti-ferromagnetism dominates when the diameter (d) is larger than 10 nm, but when *d* is smaller than 10 nm, ferromagnetism emerges and persists even up to room temperature due to the uncompensated surface spin[153, 155-157]. We believe the ferromagnetism in our thin oxidized Cu layer shares the same origin of those CuO nanostructures. Therefore, we increase the thickness of the Cu layer to 10 nm to check its consistency with anti-ferromagnetic CuO nanostructures. Figure. 7.9a shows a linear *M-H* relation,

indicating the vanishing ferromagnetism in 10 nm thick Cu layer. Also, as shown in Fig. 7.9b when thin Cu layer is covered by Nb layer before exposing to the atmosphere, minimum oxidation is expected without detectable ferromagnetism. Consistent with the previous reports[153, 155-157], these results illustrate that the origin of the ferromagnetism in our 3 nm Cu buffer layer is the naturally oxidized surface.

The magnetic property of Cu layer in those films provide a possible explanation for the origin of ferromagnetism in our Cu buffer layer and based on this assumption, our sample resembles the S/F'/F/F''/S structure reported holding the long-range triplet-supercurrent in Co up to 28 nm[138]. In their experiment, F' and F'' was used by CuNi or PdNi alloy and Cu buffer layers are employed to magnetically isolate F layer and preserve their noncollinear alignment. In our sample, the functionality of F' or F'' is fulfilled by naturally oxidized Cu layer, and its anti-ferromagnetic nature makes it immune to the exchange coupling of Ni layer even they lie closely to each other.

7.2.3 Proximity Effect with Minimum Influence of CuO

The magnetization measurement shows the Cu films we deposited are consistent with previous studies: ferromagnetism emerges at a few nanometers thick CuO due to the uncompensated spins (Fig. 7.8). Additional magnetization measurements (Fig. 7.9) show no ferromagnetism with a pure thin Cu layer and thicker CuO (> 10 nm) film. Therefore, the functionality of the CuO buffer layer can be further confirmed if the long-range superconducting proximity effect is absent in NW configuration with pure thin Cu or thicker CuO film.

In *Sample 8*, the Cu buffer layer and Nb electrodes were sharing the same mask and sputtered consecutively without breaking the vacuum. In *R-T* relation, followed by the 'critical peak', the resistance starts to drop around 7 K at zero field, which is the same as the T_c of Nb

electrodes, shown in the inset of Fig. 7.10. At 2 K, *R*-$\mu_0 H$ graph shows resistance drop starting at 4 T, prior to the appearance of 'critical peak' at 2 T. These resistance dips before the 'critical peaks' is also seen in *Sample 1&6.* Superconducting proximity range in such configuration is calculated as 13nm, which is of the comparable level of that found in *Sample 6&7*. This result is reasonable since minimum oxides should greatly reduce the noncollinear ferromagnetism in the buffer layer according to our assumption, and the inevitable oxidation around the edges of Cu layer still gives rise to a marginal proximity effect.

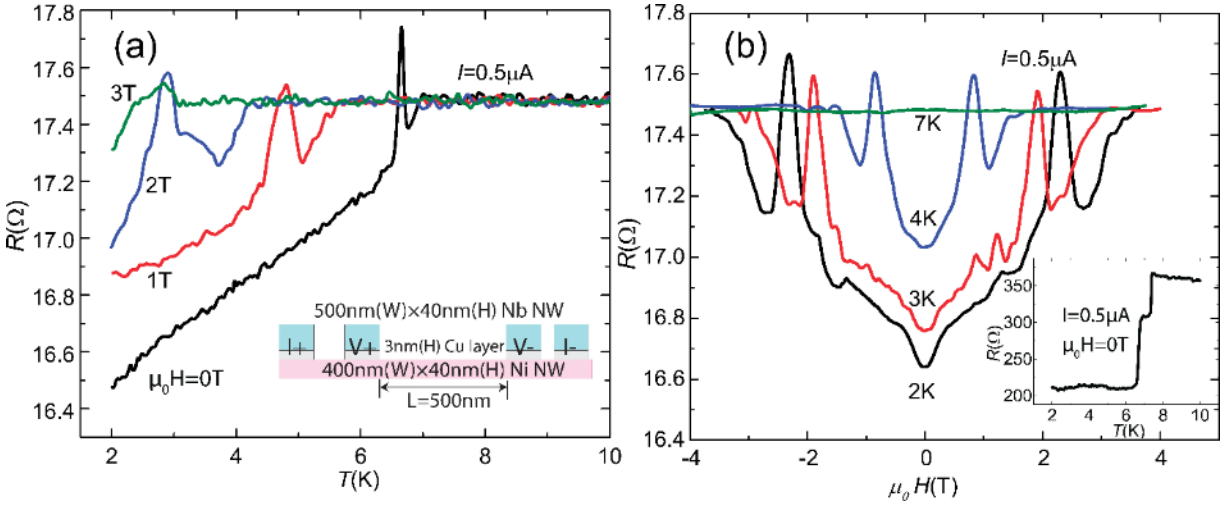

Figure 7.10 *R-T* and *R*-$\mu_0 H$ relation of *Sample 8*, where Cu/Nb are deposited consecutively in the same chamber. (a) *R-T* relation under the different magnitude of the external field. The inset is the schematic of *Sample 8* in the side view. (b) *R*-$\mu_0 H$ property under different temperatures. The inset shows contact resistance from the 2-terminal measurement.

When increasing the thickness of Cu to 10 nm in *Sample 9* and keeping other fabricating parameters used in *Sample 8*, we find the proximity range is only 2 nm at zero field. In *R*-$\mu_0 H$ graph, we encounter a magnetoresistance step when crossing zero external field, similar to *R*-$\mu_0 H$ curve of *Sample 1* in Fig. 7.1. This resistance change only takes up less than 1 % of normal

resistance and gives different normal resistance at the higher external field in *R-T* relation shown in Fig. 7.11b.

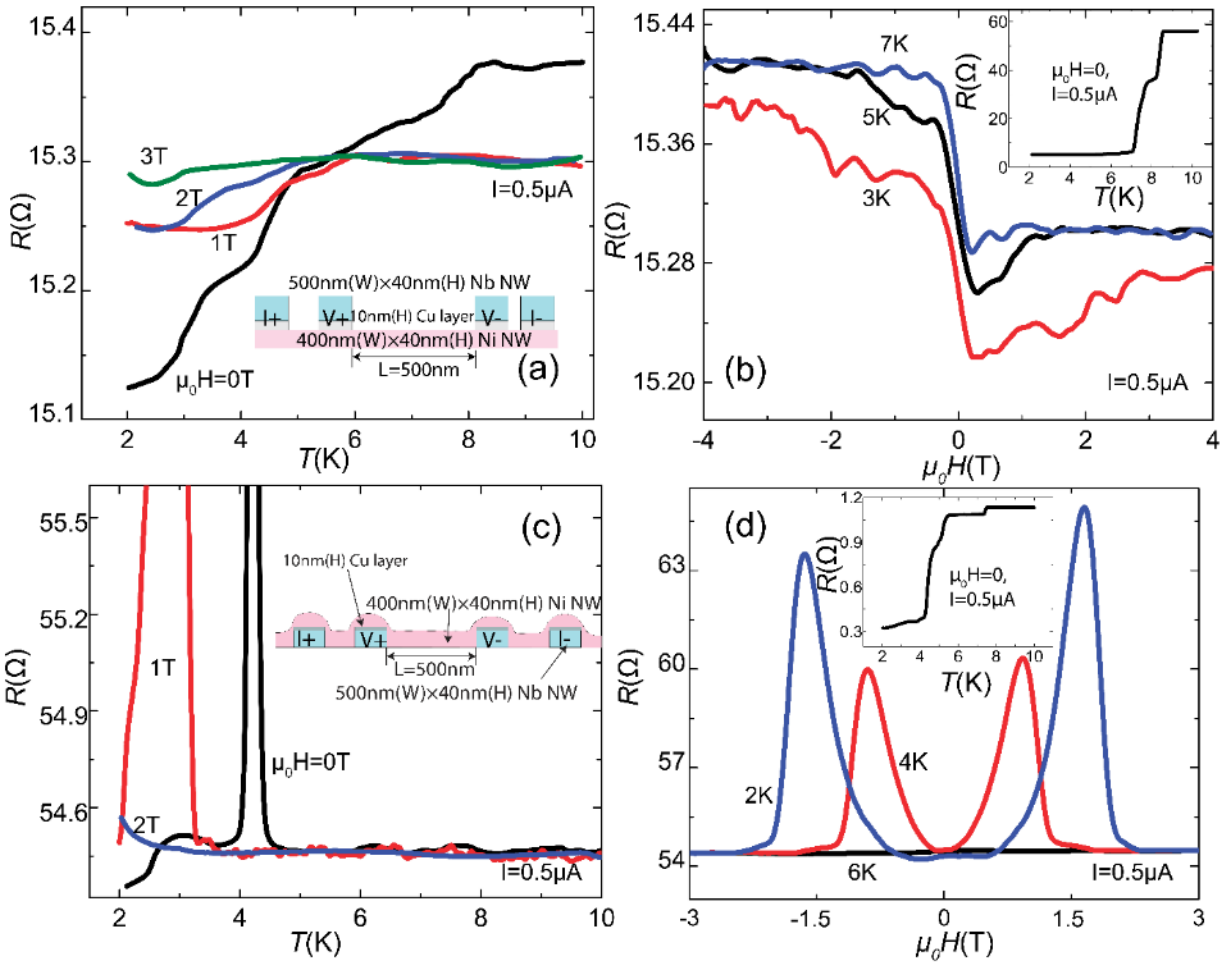

Figure 7.11 *R-T* and *R*-μ$_0$*H* relation of Ni NW with 10 nm Cu interlayer. (a) *R-T* relation under the different magnitude of the external field of *Sample 9,* where Cu/Nb are deposited without breaking the vacuum. The inset is the schematic of *Sample 9* in the side view. (b) *R*-μ$_0$*H* property under different temperatures of *Sample 9*. The inset shows contact resistance from the 2-terminal measurement. (c) *R-T* relation under different magnitude of the external fields of *Sample 10*, where Nb/Cu are sputtered prior to Ni NW. CuO is presented at the Cu/Ni interface. The inset is the schematic of *Sample 10* in the side view. (b) *R*-μ$_0$*H* property under different temperatures of *Sample 10*. The inset shows contact resistance from the 2-terminal measurement.

In *Sample 10*, we first sputtered Nb and consecutively deposited 10 nm of Cu layer, then Ni NW was evaporated after another step of fabrication. In such structure, the Cu layer was exposed to air, but we see negligible resistance drop indicating superconducting proximity range less than 1nm. *R*-*T* and *R*-$\mu_0 H$ relation are mostly dominated by the 'critical peak'.

Combined with our SQUID data, we see a strong correlation between the emergence ferromagnetism of naturally oxidized Cu buffer layer and the observation of long-range proximity effect in Ni NW. Further experiments show that when the ferromagnetism of buffer layer significantly reduced by avoiding the exposure to air, as well as increasing the thickness, long-range proximity effect also disappears. Therefore, strong evidence points to the Cu oxides for providing a noncollinear magnetic profile that is crucial to the induction of spin-triplet supercurrent in our observations of long-range proximity effect.

7.3 Conclusion

In this chapter, we report an experiment that directly correlates the dramatic effect in the spatial extent of the superconducting proximity effect along the Ni NW upon the insertion of a thin Cu buffer layer with natural oxidation between the Nb electrode and the Ni NW. We found three ferromagnetic Ni NWs with 3 nm Cu buffer layer exhibiting superconducting proximity effect with spatial extent ranging from 35 nm to 136 nm; while in the devices where Cu is absent, proximity range only yields 2 nm. In our experiment, samples were fabricated by e-beam lithography followed by physical vapor deposition (PVD). Materials with different functionality were deposited separately to guarantee relatively clean interfaces and minimum intermixing.

Our experiments provide a new understanding of triggering long-range superconducting proximity effect in a ferromagnetic NW system. We believe that the ferromagnetism originated from uncompensated antiferromagnetic spins in oxidized Cu buffer layer provides noncollinear magnetic alignment against ferromagnetic Ni wire. We hope the accessibility and flexibility of fabricating such structure could be handy in future applications and inspire many more studies.

References

1. Bernevig, B. A., Hughes, T. L., and Zhang, S. C., Quantum spin Hall effect and topological phase transition in HgTe quantum wells. *Science*, **314**, 1757-61 (2006)
2. Konig, M., et al., Quantum spin Hall insulator state in HgTe quantum wells. *Science*, **318**, 766-70 (2007)
3. Fu, L. and Kane, C. L., Topological insulators with inversion symmetry. *Physical Review B*, **76** (2007)
4. Hsieh, D., et al., A topological Dirac insulator in a quantum spin Hall phase. *Nature*, **452**, 970-U5 (2008)
5. Xia, Y., et al., Observation of a large-gap topological-insulator class with a single Dirac cone on the surface. *Nature Physics*, **5**, 398-402 (2009)
6. Chen, Y. L., et al., Experimental Realization of a Three-Dimensional Topological Insulator, Bi2Te3. *Science*, **325**, 178-181 (2009)
7. Hsieh, D., et al., Observation of Time-Reversal-Protected Single-Dirac-Cone Topological-Insulator States in Bi_2Te_3 and Sb_2Te_3. *Physical Review Letters*, **103** (2009)
8. Zhang, H. J., et al., Topological insulators in Bi_2Se_3, Bi_2Te_3 and Sb_2Te_3 with a single Dirac cone on the surface. *Nature Physics*, **5**, 438-442 (2009)
9. Chang, C. Z., et al., Experimental Observation of the Quantum Anomalous Hall Effect in a Magnetic Topological Insulator. *Science*, **340**, 167-170 (2013)
10. Chang, C. Z., et al., High-Precision Realization of Robust Quantum Anomalous Hall State in a Hard Ferromagnetic Topological Insulator. *Nature Materials*, **14**, 473-477 (2015)
11. Checkelsky, J. G., et al., Trajectory of the anomalous Hall effect towards the quantized state in a ferromagnetic topological insulator. *Nature Physics*, **10**, 731-736 (2014)
12. Kou, X. F., et al., Scale-Invariant Quantum Anomalous Hall Effect in Magnetic Topological Insulators beyond the Two-Dimensional Limit. *Physical Review Letters*, **113**, 137201 (2014)
13. Mogi, M., et al., Magnetic Modulation Doping in Topological Insulators toward Higher-Temperature Quantum Anomalous Hall Effect. *Applied physics letters*, **107**, 182401 (2015)
14. Chang, C. Z., et al., High-precision realization of robust quantum anomalous Hall state in a hard ferromagnetic topological insulator. *Nature Materials*, **14**, 473-477 (2015)
15. Deng, Y., et al., Magnetic-field-induced quantized anomalous Hall effect in intrinsic magnetic topological insulator $MnBi_2Te_4$. *arXiv:1904.11468*, (2019)

16. Mogi, M., et al., Magnetic modulation doping in topological insulators toward higher-temperature quantum anomalous Hall effect. *Applied Physics Letters*, **107**, 182401 (2015)
17. Ou, Y., et al., Enhancing the Quantum Anomalous Hall Effect by Magnetic Codoping in a Topological Insulator. *Advanced Materials*, **30** (2018)
18. Xiao, D., et al., Realization of the Axion Insulator State in Quantum Anomalous Hall Sandwich Heterostructures. *Physical Review Letters*, **120**, 056801 (2018)
19. He, Q. L., et al., Chiral Majorana fermion modes in a quantum anomalous Hall insulator-superconductor structure. *Science*, **357**, 294-299 (2017)
20. Yasuda, K., et al., Quantized chiral edge conduction on domain walls of a magnetic topological insulator. *Science*, **358**, 1311-1314 (2017)
21. Wen, X.-G., Colloquium: Zoo of quantum-topological phases of matter. *Reviews of Modern Physics*, **89**, 041004 (2017)
22. Kane, C. L. and Mele, E. J., Z2 topological order and the quantum spin Hall effect. *Physical Review Letters*, **95**, 146802 (2005)
23. Fu, L., Kane, C. L., and Mele, E. J., Topological insulators in three dimensions. *Physical Review Letters*, **98**, 106803 (2007)
24. Qi, X. L., Hughes, T. L., and Zhang, S. C., Topological Field Theory of Time-Reversal Invariant Insulators. *Physical Review B*, **78**, 195424 (2008)
25. Liu, C. X., Zhang, S. C., and Qi, X. L., The Quantum Anomalous Hall Effect: Theory and Experiment. *Annual Review of Condensed Matter Physics, Vol 7*, **7**, 301-321 (2016)
26. Chang, C. Z., et al., Simultaneous Electrical-Field-Effect Modulation of Both Top and Bottom Dirac Surface States of Epitaxial Thin Films of Three-Dimensional Topological Insulators. *Nano Letters*, **15**, 1090-1094 (2015)
27. Haldane, F. D. M., Model for a Quantum Hall-Effect without Landau Levels: Condensed-Matter Realization of the "Parity Anomaly". *Physical Review Letters*, **61**, 2015-2018 (1988)
28. Onoda, M. and Nagaosa, N., Quantized anomalous Hall effect in two-dimensional ferromagnets: quantum Hall effect in metals. *Physical Review Letters*, **90**, 206601 (2003)
29. Qi, X.-L., Wu, Y.-S., and Zhang, S.-C., Topological quantization of the spin Hall effect in two-dimensional paramagnetic semiconductors. *Physical Review B*, **74**, 085308 (2006)
30. Liu, C. X., et al., Quantum anomalous Hall effect in $Hg_{1-y}Mn_yTe$ quantum wells. *Physical Review Letters*, **101** (2008)
31. Yu, R., et al., Quantized Anomalous Hall Effect in Magnetic Topological Insulators. *Science*, **329**, 61-64 (2010)

32. Nomura, K. and Nagaosa, N., Surface-quantized anomalous Hall current and the magnetoelectric effect in magnetically disordered topological insulators. *Physical Review Letters*, **106**, 166802 (2011)
33. Li, J., et al., Intrinsic magnetic topological insulators in van der Waals layered $MnBi_2Te_4$-family materials. *arXiv preprint arXiv:1808.08608*, (2018)
34. Gong, Y., et al., Experimental realization of an intrinsic magnetic topological insulator. *arXiv preprint arXiv:1809.07926*, (2018)
35. Chang, J., Park, Y.-S., and Kim, S.-K., Atomically flat single-terminated $SrTiO_3$ (111) surface. *Applied Physics Letters*, **92**, 152910 (2008)
36. Christen, H. M., et al., Dielectric properties of sputtered $SrTiO_3$ films. *Physical Review B*, **49**, 12095-12104 (1994)
37. Zhang, J. S., et al., Band Structure Engineering in $(Bi_{1-x}Sb_x)_2Te_3$ Ternary Topological Insulators. *Nature Communications*, **2**, 574 (2011)
38. Quantum Design, I. PPMS Hardware Manual. 2008; Available from: http:// www.qdusa.com/products/ppms.html.
39. Arrott, A., Criterion for Ferromagnetism from Observations of Magnetic Isotherms. *Physical Review*, **108**, 1394-1396 (1957)
40. Leiden Cryogenics, B. V. Model MINIKELVIN 126-TOF Dilution Refrigerator- Instruction Manual. Available from: leicryo@euronet.nl.
41. Del Cueto, J., et al., Experiments in 3He-4He liquid mixtures near the tricritical point. *Le Journal de Physique Colloques*, **41**, C7-133-C7-136 (1980)
42. Pobell, F., Matter and methods at low temperatures. 2007, Springer,: Berlin ; New York. xv, 461 p.
43. PICOWATT, AVS-47B AC RESISTANCE BRIDGE-Instruction Manual. (2015)
44. Essin, A. M., Moore, J. E., and Vanderbilt, D., Magnetoelectric Polarizability and Axion Electrodynamics in Crystalline Insulators. *Physical Review Letters*, **102** (2009)
45. Wang, J., et al., Quantized topological magnetoelectric effect of the zero-plateau quantum anomalous Hall state. *Physical Review B*, **92** (2015)
46. Wilczek, F., Two applications of axion electrodynamics. *Physical Review Letters*, **58**, 1799-1802 (1987)
47. Morimoto, T., Furusaki, A., and Nagaosa, N., Topological magnetoelectric effects in thin films of topological insulators. *Physical Review B*, **92** (2015)
48. Kou, X., et al., Metal-to-insulator switching in quantum anomalous Hall states. *Nature Communications*, **6**, 8474 (2015)

49. Feng, Y., et al., Observation of the Zero Hall Plateau in a Quantum Anomalous Hall Insulator. *Physical Review Letters*, **115**, 126801 (2015)
50. Grauer, S., et al., Scaling of the Quantum Anomalous Hall Effect as an Indicator of Axion Electrodynamics. *Physical Review Letters*, **118**, 246801 (2017)
51. Mogi, M., et al., A magnetic heterostructure of topological insulators as a candidate for an axion insulator. *Nature Materials*, **16** (2017)
52. Lachman, E. O., et al., Observation of superparamagnetism in coexistence with quantum anomalous Hall C = ±1 and C = 0 Chern states. *npj Quantum Materials*, **2** (2017)
53. Walser, P., et al., Heat-induced antiferromagnetic coupling in multilayers with ZnSe spacers. *Physical Review B*, **60**, 4082-4086 (1999)
54. Faure-Vincent, J., et al., Interlayer magnetic coupling interactions of two ferromagnetic layers by spin-polarized tunneling (vol 89, art no 107206, 2002). *Physical Review Letters*, **89** (2002)
55. Yu, J., Zang, J., and Liu, C.-X., Magnetic-Resonance-Induced Current Response in Axion Insulators. *arXiv preprint arXiv:1903.12068*, (2019)
56. Jiang, W. J., et al., Skyrmions in Magnetic Multilayers. *Physics Reports-Review Section of Physics Letters*, **704**, 1-49 (2017)
57. Nagaosa, N. and Tokura, Y., Topological properties and dynamics of magnetic skyrmions. *Nat Nanotechnol*, **8**, 899-911 (2013)
58. Rajaraman, R., Solitons and instantons. (1982)
59. Brown, G. E. and Rho, M., The multifaceted skyrmion. 2010: World Scientific.
60. Callan Jr, C. G., Dashen, R., and Gross, D. J., Toward a theory of the strong interactions, in *Instantons In Gauge Theories*. 1994, World Scientific. 36-60.
61. Phatak, C., Petford-Long, A. K., and Heinonen, O., Direct observation of unconventional topological spin structure in coupled magnetic discs. *Physical Review Letters*, **108**, 067205 (2012)
62. Wintz, S., et al., Topology and origin of effective spin meron pairs in ferromagnetic multilayer elements. *Physical Review Letters*, **110**, 177201 (2013)
63. Malozemoff, A. and Slonczewski, J., Magnetic Domain Walls in Bubble Materials: Advances in Materials and Device Research. Vol. 1. 2016: Academic press.
64. Moutafis, C., Komineas, S., and Bland, J., Dynamics and switching processes for magnetic bubbles in nanoelements. *Physical Review B*, **79**, 224429 (2009)
65. Skyrme, T. H. R., A unified field theory of mesons and baryons. *Nuclear Physics*, **31**, 556-569 (1962)

66. Everschor, K., Current-induced dynamics of chiral magnetic structures: skyrmions, emergent electrodynamics and spin-transfer torques. 2012, Universität zu Köln.
67. Chen, G., et al., Novel chiral magnetic domain wall structure in Fe/Ni/Cu(001) films. *Physical Review Letters*, **110**, 177204 (2013)
68. Fert, A. Magnetic and transport properties of metallic multilayers. in *Materials Science Forum*. 1990. Trans Tech Publ.
69. Dzialoshinskii, I., Thermodynamic theory of weak ferromagnetism in antiferromagnetic substances. *Soviet Physics Jetp-Ussr*, **5**, 1259-1272 (1957)
70. Moriya, T., Anisotropic Superexchange Interaction and Weak Ferromagnetism. *Physical Review*, **120**, 91-98 (1960)
71. Dzyaloshinskii, I., The theory of helicoidal structures in antiferromagnets. II. metals. *Journal of Experimental and Theoretical Physics*, **20** (1965)
72. Yu, X. Z., et al., Real-space observation of a two-dimensional skyrmion crystal. *Nature*, **465**, 901-904 (2010)
73. Nakanishi, O., et al., The origin of the helical spin density wave in MnSi. *Solid State Communications*, **35**, 995-998 (1980)
74. Bode, M., et al., Chiral magnetic order at surfaces driven by inversion asymmetry. *Nature*, **447**, 190 (2007)
75. Bak, P. and Jensen, M. H., Theory of helical magnetic structures and phase transitions in MnSi and FeGe. *Journal of Physics C: Solid State Physics*, **13**, L881 (1980)
76. Muhlbauer, S., et al., Skyrmion lattice in a chiral magnet. *Science*, **323**, 915-9 (2009)
77. Pfleiderer, C., et al., Skyrmion lattices in metallic and semiconducting B20 transition metal compounds. *Journal of Physics: Condensed Matter*, **22**, 164207 (2010)
78. Münzer, W., et al., Skyrmion lattice in the doped semiconductor $Fe_{1-x}Co_xSi$. *Physical Review B*, **81**, 041203 (2010)
79. Miao, B. F., et al., Experimental realization of two-dimensional artificial skyrmion crystals at room temperature. *Physical Review B*, **90**, 174411 (2014)
80. Gilbert, D. A., et al., Realization of ground-state artificial skyrmion lattices at room temperature. *Nature Communications*, **6**, 8462 (2015)
81. Pizzini, S., et al., Chirality-Induced Asymmetric Magnetic Nucleation in $PtCoAlO_x$ Ultrathin Microstructures. *Physical Review Letters*, **113**, 047203 (2014)
82. Tanaka, M., et al., Electric-current-induced dynamics of bubble domains in a ferrimagnetic Tb/Co multilayer wire below and above the magnetic compensation point. *AIP Advances*, **7**, 055916 (2017)

83. Pollard, S. D., et al., Observation of stable Neel skyrmions in cobalt/palladium multilayers with Lorentz transmission electron microscopy. *Nature Communications*, **8**, 14761 (2017)
84. Tonomura, A., et al., Real-space observation of skyrmion lattice in helimagnet MnSi thin samples. *Nano Letters*, **12**, 1673-7 (2012)
85. Yu, X. Z., et al., Near room-temperature formation of a skyrmion crystal in thin-films of the helimagnet FeGe. *Nature Materials*, **10**, 106-9 (2011)
86. Seki, S., et al., Observation of skyrmions in a multiferroic material. *Science*, **336**, 198-201 (2012)
87. Adams, T., et al., Long-wavelength helimagnetic order and skyrmion lattice phase in Cu_2OSeO_3. *Physical Review Letters*, **108**, 237204 (2012)
88. Seki, S., et al., Formation and rotation of skyrmion crystal in the chiral-lattice insulator Cu_2OSeO_3. *Physical Review B*, **85**, 220406 (2012)
89. Shibata, K., et al., Current-Driven Motion of Domain Boundaries between Skyrmion Lattice and Helical Magnetic Structure. *Nano Letters*, **18**, 929-933 (2018)
90. Chen, G., et al., Tailoring the chirality of magnetic domain walls by interface engineering. *Nature Communications*, **4**, 2671 (2013)
91. Chen, G., et al., Out-of-plane chiral domain wall spin-structures in ultrathin in-plane magnets. *Nature Communications*, **8**, 15302 (2017)
92. Heinze, S., et al., Spontaneous atomic-scale magnetic skyrmion lattice in two dimensions. *Nature Physics*, **7**, 713 (2011)
93. Yang, G., et al., Majorana bound states in magnetic skyrmions. *Physical Review B*, **93**, 224505 (2016)
94. Neubauer, A., et al., Topological Hall Effect in the A Phase of MnSi. *Physical Review Letters*, **102**, 186602 (2009)
95. Lee, M., et al., Unusual Hall Effect Anomaly in MnSi under Pressure. *Physical Review Letters*, **102**, 186601 (2009)
96. Kanazawa, N., et al., Large Topological Hall Effect in a Short-Period Helimagnet MnGe. *Physical Review Letters*, **106**, 156603 (2011)
97. Huang, S. X. and Chien, C. L., Extended Skyrmion Phase in Epitaxial FeGe(111) Thin Films. *Physical Review Letters*, **108**, 267201 (2012)
98. Matsuno, J., et al., Interface-Driven Topological Hall Effect in $SrRuO_3$-$SrIrO_3$ Bilayer. *Science Advances*, **2**, e1600304 (2016)
99. Ohuchi, Y., et al., Electric-Field Control of Anomalous and Topological Hall Effects in Oxide Bilayer Thin Films. *Nature Communications*, **9**, 213 (2018)

100. Liang, D., et al., Current-driven dynamics of skyrmions stabilized in MnSi nanowires revealed by topological Hall effect. *Nature Communications*, **6**, 8217 (2015)
101. Yasuda, K., et al., Geometric Hall Effects in Topological Insulator Heterostructures. *Nature Physics*, **12**, 555-559 (2016)
102. Liu, C., et al., Dimensional Crossover-Induced Topological Hall Effect in a Magnetic Topological Insulator. *Physical Review Letters*, **119**, 176809 (2017)
103. Mogi, M., et al., A Magnetic Heterostructure of Topological Insulators as a Candidate for an Axion Insulator. *Nature Materials.*, **16**, 516-521 (2017)
104. Mogi, M., et al., Tailoring Tricolor Structure of Magnetic Topological Insulator for Robust Axion Insulator. *Science Advances*, **3**, eaao1669 (2017)
105. Nagaosa, N. and Tokura, Y., Topological properties and dynamics of magnetic skyrmions. *Nature Nanotechnology*, **8**, 899-911 (2013)
106. Nagaosa, N., et al., Anomalous Hall effect. *Reviews of Modern Physics*, **82**, 1539-1592 (2010)
107. Li, W., et al., Origin of the Low Critical Observing Temperature of the Quantum Anomalous Hall Effect in V-Doped $(Bi, Sb)_2Te_3$ Film. *Scientific Reports*, **6**, 32732 (2016)
108. Chang, C. Z., et al., Zero-Field Dissipationless Chiral Edge Transport and the Nature of Dissipation in the Quantum Anomalous Hall State. *Physical Review Letters*, **115**, 057206 (2015)
109. Wang, W. B., et al., Direct Evidence of Ferromagnetism in a Quantum Anomalous Hall System. *Nature Physics*, **14**, 791-795 (2018)
110. Ohuchi, Y., et al., Topological Hall effect in thin films of the Heisenberg ferromagnet EuO. *Physical Review B*, **91** (2015)
111. Hou, W. T., et al., Thermally Driven Topology in Chiral Magnets. *Physical Review B*, **96** (2017)
112. Bottcher, M., et al., B-T Phase Diagram of Pd/Fe/Ir(111) Computed with Parallel Tempering Monte Carlo. *New Journal of Physics*, **20** (2018)
113. Wang, W., et al., Universal Spin Chirality Fluctuation in Two-Dimensional Ising Ferromagnets. *arXiv:1812.07005*, (2018)
114. Groenendijk, D. J., et al., Berry Phase Engineering at Oxide Interfaces. *arXiv:1810.05619*, (2018)
115. Kan, D., et al., Alternative to the topological interpretation of the transverse resistivity anomalies in $SrRuO_3$. *Physical Review B*, **98**, 180408 (2018)
116. KAMERLINGH ONNES, H., The superconductivity of mercury. *Communications from the Physical Laboratory at the University of Leiden*, **122**, 122-124 (1911)

117. London, F. and London, H., The electromagnetic equations of the superconductor. *Proceedings of the Royal Society of London Series a-Mathematical and Physical Sciences*, **149**, 0071-0088 (1935)
118. Ginzburg, V. L., On the Theory of Superconductivity. *Nuovo Cimento*, **2**, 1235-1250 (1955)
119. Bardeen, J., Cooper, L. N., and Schrieffer, J. R., Theory of Superconductivity. *Physical Review*, **108**, 1175-1204 (1957)
120. Lee, P. A., Nagaosa, N., and Wen, X.-G., Doping a Mott insulator: Physics of high-temperature superconductivity. *Reviews of modern physics*, **78**, 17 (2006)
121. Steglich, F., et al., Superconductivity in the Presence of Strong Pauli Paramagnetism: $CeCu_2Si_2$. *Physical Review Letters*, **43**, 1892 (1979)
122. Stewart, S. G., Heavy-fermion systems. *Reviews of Modern Physics*, **56**, 755 (1984)
123. Bednorz, J. G. and Müller, K. A., Possible high T_c superconductivity in the Ba− La− Cu− O system. *Zeitschrift für Physik B Condensed Matter*, **64**, 189-193 (1986)
124. Wu, M.-K., et al., Superconductivity at 93 K in a new mixed-phase Y-Ba-Cu-O compound system at ambient pressure. *Physical Review Letters*, **58**, 908 (1987)
125. Saito, Y., Nojima, T., and Iwasa, Y., Highly crystalline 2D superconductors. *Nature Reviews Materials*, **2**, 16094 (2017)
126. Qi, X. L. and Zhang, S. C., Topological Insulators and Superconductors. *Reviews of Modern Physics*, **83**, 1057-1110 (2011)
127. Cao, Y., et al., Unconventional superconductivity in magic-angle graphene superlattices. *Nature*, **556**, 43-50 (2018)
128. Lin, X., et al., Fermi surface of the most dilute superconductor. *Physical Review X*, **3**, 021002 (2013)
129. Prakash, O., et al., Evidence for bulk superconductivity in pure bismuth single crystals at ambient pressure. *Science*, **355**, 52-55 (2017)
130. Gor'kov, L. P. and Kresin, V. Z., Colloquium: High pressure and road to room temperature superconductivity. *Reviews of Modern Physics*, **90**, 011001 (2018)
131. Buzdin, A. I., Proximity effects in superconductor-ferromagnet heterostructures. *Reviews of Modern Physics*, **77**, 935-976 (2005)
132. Tinkham, M., Introduction to superconductivity. 2004: Courier Corporation.
133. Eschrig, M., Spin-polarized supercurrents for spintronics: a review of current progress. *Reports on Progress in Physics,* **78**, 104501 (2015)
134. Eschrig, M., Spin-polarized supercurrents for spintronics. *Physics Today*, **64** (2011)

135. Keizer, R. S., et al., A spin-triplet supercurrent through the half-metallic ferromagnet CrO_2. *Nature*, **439**, 825-827 (2006)
136. Anwar, M., et al., Long-range supercurrents in ferromagnetic CrO2 using a multilayer contact structure. *Applied physics letters*, **100**, 052602 (2012)
137. Robinson, J. W. A., Witt, J. D. S., and Blamire, M. G., Controlled Injection of Spin-Triplet Supercurrents into a Strong Ferromagnet. *Science*, **329**, 59-61 (2010)
138. Khaire, T. S., et al., Observation of spin-triplet superconductivity in Co-based Josephson junctions. *Physical Review Letters*, **104**, 137002 (2010)
139. Wang, J., et al., Interplay between superconductivity and ferromagnetism in crystalline nanowires. *Nature Physics*, **6**, 389-394 (2010)
140. Kompaniiets, M., et al., Long-range superconducting proximity effect in polycrystalline Co nanowires. *Applied Physics Letters*, **104** (2014)
141. Takei, S. and Galitski, V., Microscopic theory for a ferromagnetic nanowire/superconductor heterostructure: Transport, fluctuations, and topological superconductivity. *Physical Review B*, **86** (2012)
142. Pauleau, Y., et al., Structure and physical properties of nickel films deposited by microwave plasma-assisted cathodic sputtering. *Journal of Physics D-Applied Physics*, **39**, 2803-2808 (2006)
143. Vandover, R. B., Delozanne, A., and Beasley, M. R., Superconductor-Normal-Superconductor Microbridges - Fabrication, Electrical Behavior, and Modeling. *Journal of Applied Physics*, **52**, 7327-7343 (1981)
144. Degennes, P. G., Boundary Effects in Superconductors. *Reviews of Modern Physics*, **36**, 225-237 (1964)
145. Klose, C., et al., Optimization of spin-triplet supercurrent in ferromagnetic Josephson junctions. *Physical Review Letters*, **108**, 127002 (2012)
146. Mills, S. A., et al., Vortex crossing, trapping, and pinning in superconducting nanowires of a NbSe2 two-dimensional crystal. *Physical Review B*, **93** (2016)
147. Yamazaki, H., Shannon, N., and Takagi, H., Superconducting proximity effect in epitaxial Nb (110)/Au (111)/Nb (110) trilayers. *arXiv preprint arXiv:1602.05790*, (2016)
148. Wang, J., et al., Proximity-induced superconductivity in nanowires: minigap state and differential magnetoresistance oscillations. *Physical Review Letters*, **102**, 247003 (2009)
149. Oboznov, V. A., et al., Thickness dependence of the Josephson ground States of superconductor-ferromagnet-superconductor junctions. *Physical Review Letters*, **96**, 197003 (2006)

150. Volkov, A. F. and Efetov, K. B., Odd spin-triplet superconductivity in a multilayered superconductor-ferromagnet Josephson junction. *Physical Review B*, **81** (2010)

151. Keil, P., Lützenkirchen‐Hecht, D., and Frahm, R. Investigation of Room Temperature Oxidation of Cu in Air by Yoneda‐XAFS. in *AIP Conference Proceedings*. 2007. AIP.

152. Wu, J., et al., Functional metal oxide nanostructures. Vol. 149. 2011: Springer Science & Business Media.

153. Zhang, Q., et al., CuO nanostructures: Synthesis, characterization, growth mechanisms, fundamental properties, and applications. *Progress in Materials Science*, **60**, 208-337 (2014)

154. Brown, P. J., et al., Antiferromagnetism in Cuo Studied by Neutron Polarimetry. *Journal of Physics-Condensed Matter*, **3**, 4281-4287 (1991)

155. Karthik, K., et al., Temperature-dependent magnetic anomalies of CuO nanoparticles. *Solid State Communications*, **151**, 564-568 (2011)

156. Gao, D., et al., Vacancy-mediated magnetism in pure copper oxide nanoparticles. *Nanoscale Research Letters,* **5**, 769-72 (2010)

157. Gao, D., et al., Room-Temperature Ferromagnetism of Flowerlike CuO Nanostructures. *The Journal of Physical Chemistry C,* 18347–18351(2010)

Vita

Jue Jiang

Education

Ph.D. of Physics	The Pennsylvania State University (University Park, PA)	2019
B.S of Physics	Sichuan University (Chengdu, PRC)	2013
Exchange Study, Physics	The University of Utah (Salt Lake City, UT)	2012-2013

Publications (* indicates equal contribution)

Jiang J*, Xiao D*, Shin JH, Wang W, et al. 'Crossover of Quantum Anomalous Hall to Topological Hall Effect in Magnetic Topological Insulator Sandwich Heterostructures', *arXiv*: 1901.07611, 2019 (Pre-printed).

Jiang J, Zhao W, Du R, Miao L, et al. 'Long range proximity effect in Ni nanowires.' (In preparation).

Xiao D*, **Jiang J*,** Shin JH, Wang W, et al. 'Realization of the axion insulator state in quantum anomalous hall sandwich heterostructures', *Phys. Rev. Lett.* 120, 056801 (editors' suggestion).

Zhao W*, Li M*, Chang CZ*, **Jiang J,** et al. 'Direct imaging of electron transfer and its influence on superconducting pairing at FeSe/$SrTiO_3$ interface', *Science advances*, 4(3), p. eaao2682.

Wang F, Zhang H, **Jiang J**, Zhao YF, et al. 'Chromium-induced ferromagnetism with perpendicular anisotropy in topological crystalline insulator SnTe (111) thin films' *Physical Review B* 97 (11), 115414.

Wang F*, Xiao D*, Yuan W*, **Jiang J**, et al. 'Observation of Interfacial Antiferromagnetic Coupling between Magnetic Topological Insulator and Antiferromagnetic Insulator', *arXiv*: 1901. 02905, 2019 (Pre-printed).

Kayyalha M*, Xiao D*, Zhang R*, Shin JH, **Jiang J**, et al. 'Non-Majorana Origin of the Half-Quantized Conductance Plateau in Quantum Anomalous Hall Insulator and Superconductor Hybrid Structures', *arXiv:* 1904.06463, 2019 (Pre-printed).

Bersch B, Briggs N, Wang Y, **Jiang J**, et al. 'An Atomically Thin Gallium/Graphene Superconducting Heterostructure' arXiv:1905.09938, 2019 (Pre-printed).